Progress in Materials Science xxx (xxxx) xxxx

Contents lists available at ScienceDirect

Progress in Materials Science

journal homepage: www.elsevier.com/locate/pmatsci

The fate and role of *in situ* formed carbon in polymer-derived ceramics

Qingbo Wen[c], Zhaoju Yu[a,d,*], Ralf Riedel[b,c]

[a] College of Materials, Key Laboratory of High Performance Ceramic Fibers (Xiamen University), Ministry of Education, Xiamen 361005, China
[b] State Key Laboratory of Solidification Processing, Northwestern Polytechnical University, Xi'an, Shaanxi 710072, China
[c] Technische Universität Darmstadt, Institut für Materialwissenschaft, Otto-Berndt-Straße 3, D-64287 Darmstadt, Germany
[d] College of Materials, Fujian Key Laboratory of Advanced Materials (Xiamen University), Xiamen 361005, China

ARTICLE INFO

Keywords:
Free carbon
Segregated carbon
Microstructure
High-temperature resistance
Structural and functional properties

ABSTRACT

Polymer-derived ceramics (PDCs) have been intensively studied for nearly 50 years due to their unique advantages to producing ceramic fibers, coatings, foams, nanocomposites and for additive manufacturing. A phenomenon associated with the polymer-to-ceramic transformation process using organo-substituted silicon polymers as the starting material has been widely reported, namely, *in situ* formation of carbon within the generated silicon-based ceramic matrix. Interestingly, the precipitation of carbon depends to a great extent on the molecular structure of the preceramic polymer and significantly affects the composition, crystallization and decomposition behavior, microstructural evolution as well as the related structural and functional properties of PDCs. Thus, this review article highlights the recent progress in the PDC field with the focus on the fate and role of the *in situ* formed carbon. Firstly, a brief summary of the synthesis and processing of PDCs is provided, followed by the microstructural characterization of the formed ceramics. The *in situ* formation of carbon, precursor-carbon-morphology relation and high-temperature evolution of the carbon will be summarized. Secondly, the influence of the segregated carbon on the microstructure and its associated properties of the PDCs will be comprehensively highlighted. Finally, potential advanced structural and functional applications of the PDCs related to the carbon are evaluated.

1. Introduction

1.1. History and recent developments of PDCs

Si-based advanced ceramics (*e.g.*, SiC, Si_3N_4) that provide a good combination of high strength, superior hardness, outstanding oxidation resistance as well as excellent thermal and chemical stability are one of the most important classes of advanced materials. Conventionally, the Si-based ceramic parts are manufactured by the powder processing technology, including powder synthesis, powder processing (*e.g.*, milling and mixing), shaping and sintering [1]. However, the powder technologies are not suitable for fabricating ceramic fibers, crack-free coatings/films, ceramic matrix composites, ceramic nanocomposites as well as dense ceramic monoliths obtained at relatively low processing temperatures (*e.g.*, 1100–1300 °C).

In the early 1960s, organosilicon polymers have been proposed for the preparation of Si-based ceramics via a polymer-to-ceramic

* Corresponding author at: College of Materials, Key Laboratory of High Performance Ceramic Fibers (Xiamen University), Ministry of Education, Xiamen 361005, China.
E-mail address: zhaojuyu@xmu.edu.cn (Z. Yu).

https://doi.org/10.1016/j.pmatsci.2019.100623
Received 18 August 2018; Received in revised form 28 November 2019; Accepted 28 November 2019

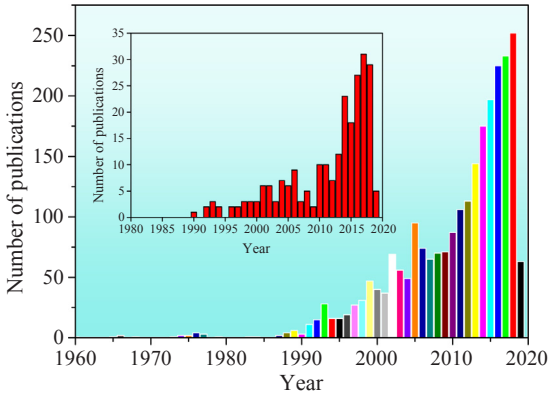

Fig. 1. Number of publications resulting from a search with the keyword "polymer derived ceramics" in "All databases" on "web of science", from 1960 up to the end of April 2019. The inset is the number of publications related to "free carbon" in the framework of "PDCs".

transformation process, and the resulting ceramics are denoted as PDCs [2,3]. The potential of such preceramic polymers for materials science was not recognized until the first practical application reported by Veerbeck [4,5], Winter [6], and Yajima [7–10] in 1970s, *i.e.*, the manufacture of small-diameter Si_3N_4/SiC-based and SiC-based ceramic fibers via thermolysis of polyorganosilicon precursors. Since then, numerous preceramic polymers for the synthesis of Si-based ceramics have been developed [11–18]. The transformation of polymer to ceramic upon pyrolysis provides an important opportunity to develop several novel Si-based advanced ceramics, including coatings/films [19–22], small-diameter fibers [7,23], ceramic matrix composites [24–27], dense monoliths obtained at relatively low temperatures (1000–1300 °C) [15,28,29] as well as non-oxide ceramics stable at temperatures up to 2000 °C [14,18]. Moreover, the PDC route enables facile producing of Si-based ternary (*e.g.*, SiCN, [30–34] and SiOC [35–39]), quaternary (*e.g.*, SiBCN [14,40–43], SiBCO [44–46], SiCNO [47–50], SiAlCN [51–54], and SiAlCO [55–58]) or even pentanary (*e.g.*, SiHfBCN [59–62] and SiHfCNO [63–66]) ceramics, which are difficult to be fabricated by other methods so far [18,67]. Consequently, PDCs attracted increasing attention in the past decades, and the number of publications still grows dramatically (Fig. 1). Particularly, the number of publications clearly denoted as "PDCs" in the past 10 years (2009–2018) is around 1600, which is more than that of all the publications before 2009.

Owing to the promising structural and functional properties as well as their ability for being shaped upon various processing techniques, PDCs have found fundamental and technological interest for a variety of applications in several key fields, such as high-temperature resistant materials for structural applications (*e.g.*, ceramic fibers [9,68–70], ceramic matrix composites [25,60,71,72], environmental/thermal barrier coatings [21,73–75], joining materials [76,77] and ceramic foams/aerogels [78–81]), ceramic heaters (*e.g.*, glow plugs) [82], heat exchangers [83], electromagnetic absorbing and shielding applications [84–87], microelectromechanical systems (MEMS) [88–93], photoluminescent applications [94–97], energy and environmental applications [98–103], tribological applications (*e.g.*, brakes for motorbikes) [104–108], sensing materials [109–112] and biomedical components [113–115]. The SiOC ceramics are even regarded as an "All-Rounder" materials suitable for several advanced structural and functional applications [116]. The typical applications of the PDCs are shown in Fig. 2, and more information can be found in some other review articles and books [13,18,78,82,89,116–119].

Recently, numerous novel ceramic nanocomposites with tailored microstructures and properties were successfully synthesized using the PDC approach. The structural and functional properties of the polymer-derived ceramic nanocomposites can be controlled at the nanoscale level by molecular design of the preceramic precursors [120–122]. Moreover, polymer-derived porous ceramics, ceramic nanowires/nanobelts as well as ceramic micro-lattice, honeycomb cellular and sub-micrometer 3D complex architectures fabricated by additive manufacturing of preceramic precursors have been reported as well [123–127]. In addition, a few Si-free PDCs have also been developed in the past, such as polymer-derived BN [128–132], BCN [133–135], ZrO_2 [136], transition metal nitrides [137–139] as well as ultrahigh temperature ceramics (*e.g.*, TiC [140–142], ZrC [141–143], ZrB_2 [144,145], ZrC/ZrB_2 [146], HfC [141,147] and $HfTaC_2$ [148]). Detailed information regarding the history and developments of PDCs can be found in some other review articles and books published from 1984 to 2019 [18,67,82,89,116,118–120,127,149–162]. In the present review, we focus on highlighting the fate and role of *in situ* formed carbon in Si-based PDCs. The Si-free PDCs also contain *in situ* formed free carbon, but they will not be discussed here because the free carbon shows similar fate and role to that within the Si-based PDCs [140,142,143,147,162].

1.2. In situ formation of carbon

Within the research field of PDCs, a phenomenon associated with the polymer-to-ceramic transformation process, namely the *in situ* formation of carbon (so called "free carbon") in the generated silicon-based ceramic matrix, has been widely reported [7,41,163–167]. After several decades of research, it is believed that the presence of free carbon must be a common event for any PDCs, even with the C/Si ratios as low as 0.7 [17,163,168,169]. As shown in Fig. 1, a large amount of publications (> 300 articles) are directly related to free carbon, and the number of publications increases with increasing of PDC-related publications. Moreover,

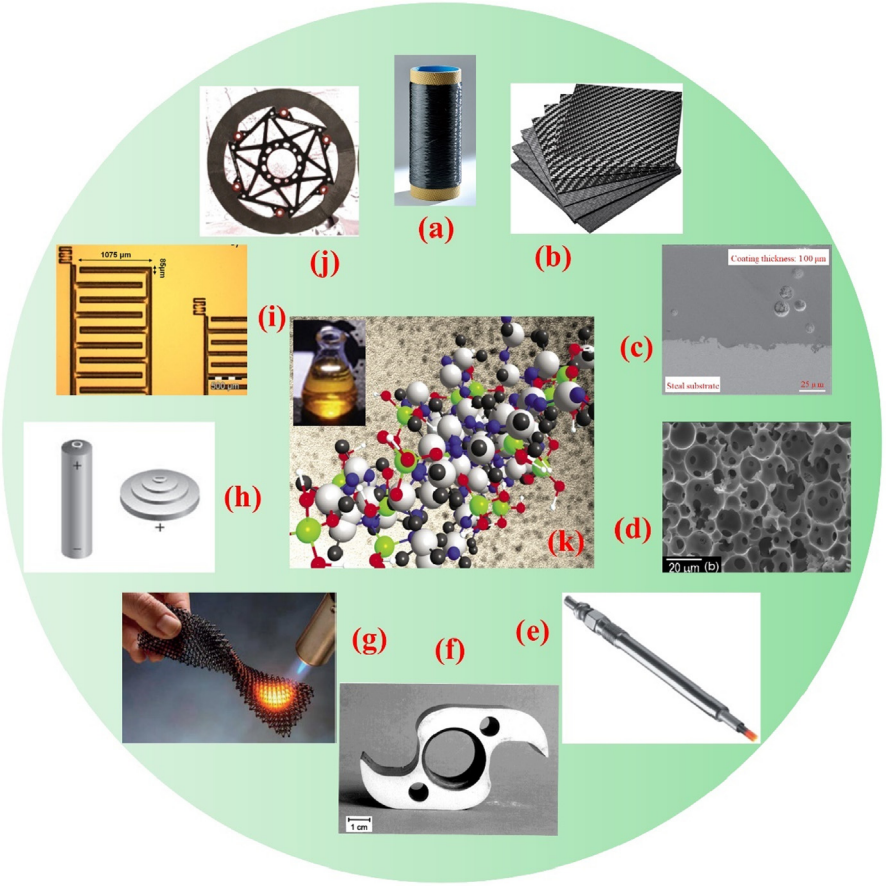

Fig. 2. Selected applications of polymer-derived ceramics (PDCs): (a) Nicalon silicon carbide continuous fibers (source: Nippon Carbon Co., Ltd, http://www.carbon.co.jp); (b) Ceramic matrix composites (source: MarketandResearch.biz, https://marketandresearch.biz/); (c) SEM image of the 100 µm thick polysilazane-derived coatings with boron silicate-barium silicate glass filler particle mixture on a 1.7335 steel substrate [648]; (d) SEM image of a micro-cellular open cell foam obtained by pyrolysis of a silicone resin [123]; (e) SiCO based ceramic glow plug (source: Robert Bosch GmbH, http://www.bosch.com); (f) Polymer-derived engineering ceramics: high precision shaping of complex components with a thermal expansion similar to steel for vacuum pump devices [13]; *(g)* Additive manufactured SiOC ceramics [124]; (h) Lithium ion batteries in which the SiOC and SiCN ceramics can be used for anode materials [199,561,690] (i) SiOC ceramic microstructures on silicon wafer (with dimensions down to 20 µm) fabricated by photolithography approach [226]; (j) Polymer-derived C/C/SiC ceramic brake disk Starblade^{TM} produced for motorbikes (Starfire Systems, Inc., https://www.starfiresystems.com/) [82]; (k) A ball and stick model of a preceramic polymer (source: front cover picture of the themed issue on Chemical Society Reviews [691]). The inset in (k) is a picture of a commercially available allylhydridopolycarbosilane (SMP10, Starfire systems, Inc., USA).

the free carbon is found to act as an independent entity in the PDCs rather than to link to the surrounding medium (except for the mixed bonds at the interface when pyrolyzed at lower temperatures). Different from the “carbidic carbon” in which the carbon atoms are directly bonded to Si atoms forming a sp^3-hybridization, the carbon atoms in the free carbon are not directly bonded to Si or other atoms but bonded to each other, forming a sp^2-hybridization. Therefore, it is called “free carbon”, “segregated carbon”, “sp^2-carbon” or sometimes “excess carbon”.

The free carbon stems from the hydrocarbon groups (*e.g.*, alkyl, vinyl, allyl, phenyl and benzyl groups) that are attached to the backbone of the preceramic precursors (*i.e.*, the R_1 and R_2 groups in Fig. 3). After pyrolysis, hydrogen atoms are removed preferentially leaving behind excess carbon in the ceramics [170–172]. Accordingly, there is a strong relationship between the molecular structure of the preceramic polymer and the amount and distribution of free carbon within the PDCs, which was proved by numerous studies [173–176]. Firstly, G.T. Burns et al. investigated the effects of the hydrocarbon groups (*i.e.*, R groups in Fig. 3) on the chemical composition of SiCN- and SiOC-based ceramics [170,177–179]. The results reveal that the saturated and unsaturated *R* groups have totally different effects on the free carbon content of PDCs. For the saturated *R* groups (*e.g.*, methyl, ethyl, propyl and isobutyl), the free carbon content in the PDCs is relatively low and it is independent on the molecular structure and number of carbon atoms on the side groups. In contrast, the unsaturated *R* groups (*e.g.*, allyl, vinyl, phenyl groups) lead to higher free carbon contents with a variable range of amounts. Generally, the free carbon content in the ceramics increases as the number of carbon atoms in the R group increases. For instance, the free carbon content in the ceramics follows the trend of allyl < 3-butenyl < phenyl < benzyl [170]. Analogous phenomenon was analyzed by Mera et al. in a series of SiCN-based ceramics derived from poly(silylcarbodiimides)

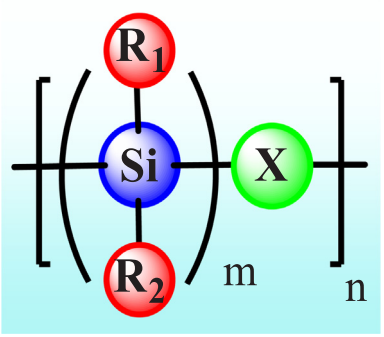

Fig. 3. General monomeric unit of typical preceramic organosilicon polymers. The variation of *X* results in different classes of Si-based polymers (*e.g.*, polycarbosilane with $X = CH_2$, polysiloxane with $X = O$, polysilazane with $X = NH$, and polysilylcarbodiimide with $X = [N = C = N]$); R_1 and R_2 are functional groups (*e.g.*, hydrogen, aliphatic or aromatic groups) determining the chemical and physical properties of the polymers and the resultant ceramics [18].

with different substituents (H, phenyl, methyl or vinyl) [176]. Hurwitz et al. also demonstrated that the free carbon content of SiOC-based ceramics increases with increasing concentration of phenyl groups in the preceramic polymers [180]. E. Bouillon et al. studied the free carbon content in several SiC-based ceramic fibers prepared from a series of functional polycarbosilanes. They claimed that the amount of free carbon within the PDCs strongly depends on the thermal stability of the hydrocarbon linkages, rather than on the percentage of the total carbon content of the polymer [181].

Furthermore, the thermal-treatment conditions (temperature, atmosphere and duration) also play an important role in the fate of free carbon within the PDCs [174,175,182,183]. These correlations will be carefully discussed in the following sections.

Formerly, the free carbon was thought to be detrimental to the mechanical properties (*e.g.*, tensile strength, hardness, and Young's modulus) and high-temperature properties (*e.g.*, thermal stabilities and oxidation resistance) of the final PDC products [165]. Consequently, many efforts have been made to reduce the content of free carbon, for instance, adjusting the molecular structure of preceramic polymers or pyrolyzing the polymers under reducing atmosphere (*e.g.*, H_2 and NH_3) [174,175,184,185]. However, in recent years, this view has been completely revised due to the fact that, under certain conditions, several carbon-rich PDCs exhibit better resistance toward crystallization, decomposition and oxidation than those with lower free carbon content [165–167,176,178–180,186,187]. In addition, the free carbon also has been proven to be beneficial for a number of other structural and functional properties of the PDCs, such as electrical conductivity [188–195], electromagnetic properties [196–198], electrochemical properties [37,199,200], piezoresistivity [201–203], corrosion resistance [184,204], tribological properties [104,106,205], creep resistance [206–208], as well as high-temperature anelastic behavior [209]. Accordingly, in the past decades, the fate and role of the free carbon on the structural and functional properties of PDCs is one of the most intriguing questions in this field of research. Numbers of meaningful studies have been reported. However, there is still a need to fully understand its generation and structural evolution under different thermal-treatment conditions, interactions with the Si-based ceramic matrix and how it affects the properties for the sake of tailoring the performance of PDC materials upon adjusting the amount, morphology, grain size, crystallinity and distribution of the free carbon [165]. This article, for the first time, is to review the research results regarding the fate and role of *in situ* formed free carbon within the PDCs in the past decades in order to provide a systematic information for the researchers to further investigate and understand the free carbon as well as the PDCs.

2. General synthetic routes for Si-based preceramic polymers

Synthesis of the preceramic precursors is a crucial step in fabrication of PDCs because not only the chemical composition but also the phase composition and microstructure of obtained ceramics (including the status of the free carbon) are strongly affected by the molecular structure of the preceramic polymers. As a result, the structural and functional properties of PDCs can be effectively adjusted by design of the precursors at the molecular level.

An overview of synthesis routes for the most typical preceramic polymers that are suitable for Si-based advanced ceramics are shown in Fig. 4 [18]. The synthesis of silicon-based polymers mainly involves the reaction of organochlorosilanes with Na/K to produce polysilanes and polycarbosilanes (after Kumada rearrangement), with water to produce polysiloxanes, as well as reactions with ammonia or amines to prepare polysilazanes or with bis(trimethylsilyl)carbodiimide to synthesize poly(silylcarbodiimides). The synthesis of polyborosilazane and polyborosilylcarbodiimide for SiBCN ceramics can be realized via at least two different approaches (*i.e.*, starting from monomers or chemical modification of polymers) with the prerequisite that there must be unsaturated carbon bonds on the *R* groups (*e.g.*, allyl or vinyl groups) for hydroboration reactions or N—H bonds on the backbone of the polymers for dehydrocoupling [14,69,156,210,211]. Moreover, in order to meet the requirements of practical applications, some properties of the polymers are quite important, such as *(1)* high molecular weight in order to avoid volatilization and to ensure high ceramic yield on pyrolysis; *(2)* suitable solubility and rheological properties for processing/shaping; *(3)* latent reactivity (*i.e.*, the presence of functional groups); *(4)* synthesis of ceramics with defined stoichiometry, *e.g.*, SiC or Si_3N_4; *(5)* no gelation, no uncontrolled polymerization or aging [67,160] and others. Up to now, numbers of Si-based preceramic polymers have been synthesized, and the

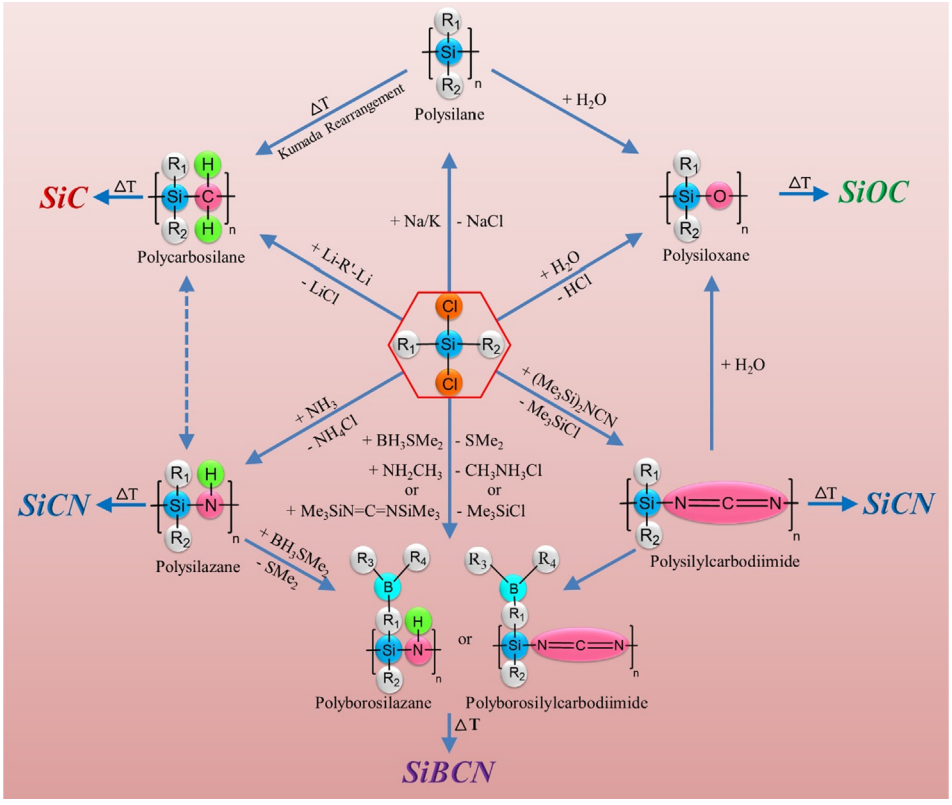

Fig. 4. Synthetic routes for the most representative classes of Si-based polymers and corresponding ceramics from organochlorosilanes [18,67].

synthesis routes have been summarized in various review articles [1,18,67,149,151–153,155,156].

3. Processing of PDCs

Fabrication of PDCs typically comprises the following steps: *(1)* synthesis of preceramic precursors using appropriate monomers; *(2)* shaping and crosslinking at low temperatures (100–400 °C); *(3)* polymer-to-ceramic transformation (*i.e.*, ceramization) via pyrolysis at temperatures ranging from 400 to 1400 °C [18,160]. Most PDCs after the polymer-to-ceramic transformation are

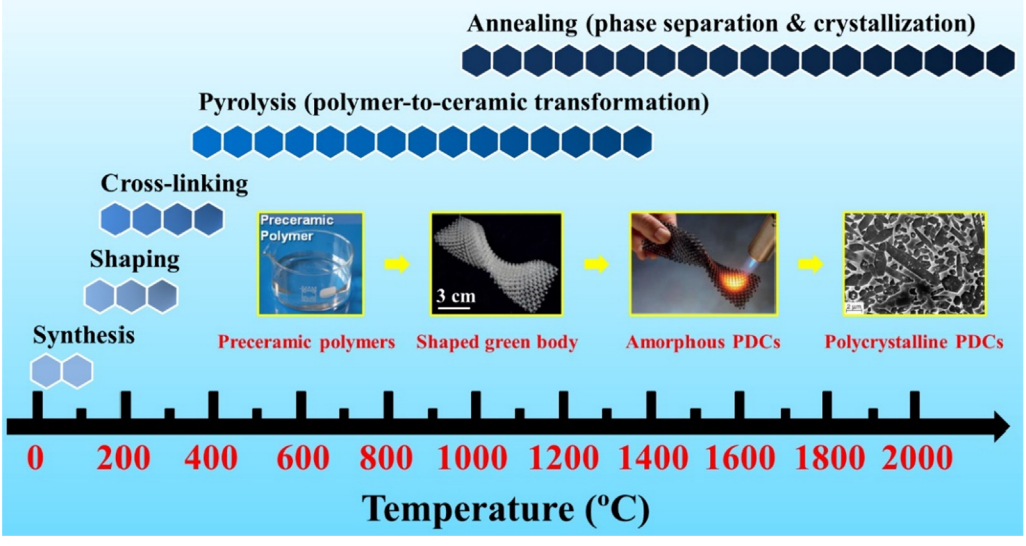

Fig. 5. Processes involved during the formation of PDCs at different temperatures [18,124,159].

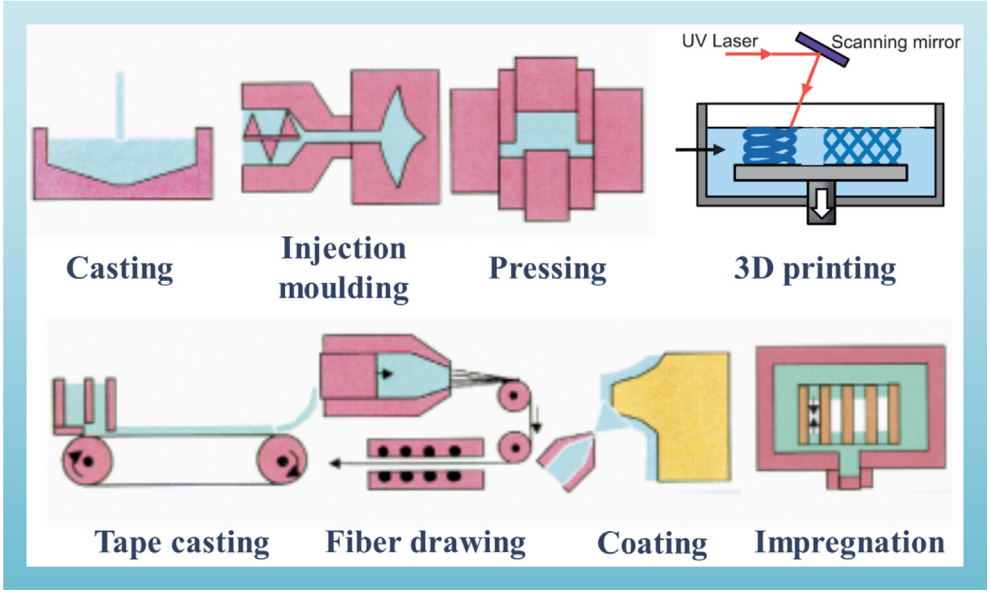

Fig. 6. Various shaping technologies suitable for the production of PDC components [18,124].

amorphous. The (poly)crystalline PDCs can be obtained by subsequent annealing of the amorphous ceramics at elevated temperatures (> 1000 °C). The general temperature range for the processing is shown in Fig. 5.

3.1. Shaping technologies

The preceramic precursors are polymeric in nature, which is one of the most important characteristics of the PDCs. The adjustable solubility, fusibility and viscosity of the polymers enable that they can be subjected to a large number of different shaping methods (*e.g.*, fiber drawing, dip- or spin-coating, polymer infiltration or resin transfer molding, freeze casting, UV/X-ray lithography and warm pressing) to prepare novel or unique ceramic components after subsequent pyrolysis, such as ceramic fibers [7,8,212,213], ceramic coatings/films [21,214–217], ceramic matrix composites [25,60,71,72,218–220], porous ceramics [38,221–223], ceramic microparts [224–227] and dense monoliths obtained at relatively low processing temperatures [15,228–231], which are difficult to be fabricated by ceramic powder/paste technologies (Fig. 6) [18]. In recent years, additive manufacturing has made a new breakthrough in the fabrication of PDCs [124,126,232–235]. Using the PDC method, the ceramic components can be easily shaped and machined before ceramization, which therefore can avoid the problems caused by tool wear and brittle fracture of the ceramics [236–239]. Compared with other molecular synthesis methods the PDC approach also has a lot of advantageous: *(a)* it can be used to synthesize non-oxide advanced ceramics, particularly the ternary, quaternary or even pentanary ceramics; *(b)* it does not need long processing time for gelation and drying; *(c)* it does not need flammable solvent for shaping; *(d)* the polymer solutions are stable for a long time storage; *(e)* it is available for large-scale production in industrial applications. More details regarding the processing of PDCs are summarized in related review articles [18,119,154,214,240].

3.2. Cross-linking

In the fabrication of PDCs, one cannot ignore an important step (so called cross-linking) in which the preceramic precursors should be converted into infusible organic/inorganic materials in order to not only increase the ceramic yield but also to retain the shape of the precursors during the polymer-to-ceramic transformation (*i.e.*, ceramization process) [241,242]. Based on the chemical features of polymers, the cross-linking process can be initiated under different mechanisms [18]. Thermal cross-linking is generally considered when the elemental and phase composition of final ceramics must be controlled, because no additional elements are introduced. The capability of thermal cross-linking comes from the reactive functional groups (*e.g.*, Si-H, Si-OH, N-H and vinyl/allyl substituents) on the preceramic polymers via condensation or addition reactions [18,153]. In the thermal crosslinking process, four major reactions may be involved, namely, hydrosilylation (*e.g.*, Si-H/vinyl groups), polymerization (*e.g.*, vinyl or allyl groups), transamination (*i.e.*, evolution of amines, ammonia or oligomeric silazanes), and dehydrocoupling (*e.g.*, Si-H/Si-H or Si-H/N-H groups) [59,153,228,243–246]. Yive et al. found that the cross-linking activities can be arranged in the following order: hydrosilylation > dehydrocoupling > transamination > vinyl group polymerization [243]. The presence of catalysts can lead to a remarkable decrease in the thermal cross-linking temperature, allowing for the cross-linking occurs during shaping but not in the subsequent pyrolysis treatment [93,245,247].

In addition to the thermal treatment, the cross-linking activity can be realized in other methods. For instance, the crosslinking of polycarbosilanes (PCS) can be achieved with either oxygen [8,248–253] or electron-beam curing [117,150,253,254]. Nevertheless,

the former results in much higher oxygen content in the final SiC materials (*e.g.*, SiC fibers) [117,253]. UV-crosslinking method can be used on the preceramic polymers with photo-sensitive functional groups for micro-component or fiber fabrication [88,255–258]. Reactive gases (*e.g.*, NH_3, $SOCl_2$, NO_2, NO, halogenated or unsaturated hydrocarbon) [259–262] or reactive plasma based on NH_3, CH_4, N_2, H_2, H_2O, O_2, SiH_4, or BH_3 gas [263,264] have also been used for cross-linking at low temperatures (typically lower than 200 °C). For some precursors such as silicone resins containing Si-OH groups, the shaped components can be even crosslinked by immersing in a highly alkaline solution [265]. Recently, rapid prototyping and 3D printing of PDCs have been developed, in which selective laser curing has been successfully applied to fabricate ceramic components with a high degree of morphological complexity [266–275].

3.3. Polymer-to-ceramic transformation

As shown in Fig. 5, in order to obtain the PDCs, the crosslinked preceramic polymers have to be pyrolyzed at temperatures from 400 to 1400 °C within inert or reactive gases, depending on different classes of polymers [160]. The most representative ceramics derived from typical organosilicon polymers are summarized in Fig. 4. After thermolysis, the poly(organocarbosilanes), poly(organosiloxanes), poly(organosilazanes)/poly(organosilylcarbodiimides) and poly(organoborosilazane) will be converted into amorphous SiC-, SiOC-, SiCN- and SiBCN-based ceramics, respectively.

Up to now, the mechanisms involved in the polymer-to-ceramic transformation process are still not well clarified due to their high complexity resulting from the amorphous structure of both highly crosslinked polymeric precursors and resultant amorphous ceramics. However, some advanced techniques are available for us to *in situ* or *ex situ* investigate the complicated ceramization process, in order to improve the ceramic yield and to control the composition of the obtained ceramics. Solid-state nuclear magnetic resonance (NMR), Fourier transform infrared (FT-IR) and Raman spectroscopy can be used to *ex situ* characterize the structural evolution of the precursors after being pyrolyzed at different temperatures [245]. Using thermogravimetric analysis (TGA) coupled with *in situ* mass spectrometry (MS) and FTIR spectroscopy, one can study the decomposition and elimination behavior of the preceramic polymers by quantitively analyzing the released volatile species and fragments in the flowing gas as well as to optimize the heating program for the polymer-to-ceramic transformation process upon identifying and resolving the mass loss peaks [66].

The polymer-to-ceramic transformation process can be realized through thermal or nonthermal methods depending on different classes of polymers and aims. The most widely used thermal method is the pyrolysis of preceramic precursors in a programmed tube furnace as mentioned above [18]. In addition, chemical vapor deposition [276,277], plasma spraying [278], rapid thermal annealing [279], laser pyrolysis [280–285], flash pyrolysis [286], microwave pyrolysis [287,288], and ion irradiation [289–293] have also been used. Among these methods, the ion irradiation is a nonthermal method in which ceramization occurs by elimination of hydrogen atoms via cleavage of C—H bonds [291,292,294–296].

Interestingly, the conditions for polymer-to-ceramic transformation process have very strong effects on the resultant ceramics, such as ceramic yield, chemical and phase compositions [18]. Thus, the content and morphology of free carbon are also strongly influenced. The most important effect should come from the pyrolysis atmosphere. For instance, using H_2 as protection gas of pyrolysis, the ceramics without free carbon can be obtained [208,297,298], whereas the free carbon is very hard to avoid if using argon or nitrogen as protection gas [182]. This is because the hydrogen atmosphere suppresses evolution of H_2 from precursors but helps to remove the alkyl or aryl groups and free carbon in the form of CH_4 during pyrolysis, which is totally different from the decomposition mechanisms under argon or nitrogen [175]. In addition, one can also use NH_3 or water vapor to reduce the free carbon content within the resultant ceramics [174,183,299]. This may be ascribed to the high possibility of abstraction of hydrogen atoms from the NH_3 or H_2O molecules by $\equiv C\bullet$ radicals on the alkyl or aryl groups forming C—H bonds, which hinders the combination reactions (*e.g.*, $\equiv C_1\bullet + \equiv C_2\bullet$) responsible for the free-carbon formation [300]. In addition, even if the free-carbon forms, it can also be removed at temperatures $\geq$800 °C by reaction with ammonia via the evolution of HCN and H_2 [174,300]. Moreover, the pressure (either mechanical-hot pressing or gaseous-hot isostatic pressing) and temperature-related processing parameters such as heating rate, dwelling temperature and holding time can also affect the free carbon in the ceramics. For instance, vacuum promotes carbothermal reactions and can therefore boost the depletion of free carbon. Added pressure has been proven to result in a high free carbon content, as it can hinder the carbothermal reactions occurring at high temperatures [18,301,302].

3.4. Processing of PDC powders

The as-pyrolyzed ceramic powders can be heat-treated at elevated temperatures (usually > 1100 °C) in order to obtain crystalized ceramic powders (annealing) or monoliths (sintering), and the amorphous ceramics will undergo further phase separation and crystallization under this condition, generally leading to the formation of a ceramic (nano)composite with multiple phases [36,120,303–307]. The ordering of the free carbon in the ceramic matrix increases with increasing of annealing temperature, which has been proven by TEM and Raman spectroscopy [177,245,307,308]. In addition, the carbothermal reactions between the free carbon and oxygen- or nitrogen-containing phases occur significantly when the temperature is higher than 1500 °C, resulting in a reduce of carbon, oxygen and nitrogen content with releasing of gaseous products (*e.g.*, CO, SiO or N_2), generation of new phases as well as a mass loss of the ceramic materials [177,188,241,245,307,309,310].

In order to prepare fully dense ceramic monoliths, the as-pyrolyzed ceramic powders are also consolidated at high temperatures using hot pressing [90,301,305,306,311–313] or spark plasma sintering [302,310,314–322]. Normally, the obtained dense monoliths exhibit much better mechanical properties than the ceramic monoliths prepared by pyrolysis of the shaped preceramic precursors (so called green body) [321,323].

Moreover, the as-pyrolyzed ceramic powders can be subject to high-pressure and high-temperature conditions in a laser-heated diamond anvil cell (LHDAC) or a multianvil apparatus to synthesize novel ceramic materials with excellent structural and functional properties [324]. For instance, the spinel-type γ-Si_3N_4 has been synthesized in a multi-anvil apparatus using amorphous Si_3N_4 as starting materials which are obtained by pyrolysis of silicon nitride imide [*i.e.*, $Si_2N_2(NH)$] in ammonia atmosphere [325]. The Vickers hardness of the γ-Si_3N_4 was measured to be around 35 GPa, which is considered to be the third hardest material in the world after diamond and c-BN up to now [326,327].

In addition to thermal treatment, the PDC powders can be used for preparing hierarchically porous carbide-derived carbon (CDC) materials with high specific surface area (SSA) by HF acid etching at room temperature or Cl_2 etching at high temperatures [109,204,328–335]. For example, Vakifahmetoglu et al. produced a hierarchically micro-/mesoporous carbon with a high specific surface area (SSA, 2700 m^2/g) by etching the polymer-derived SiOC ceramics with chlorine gas at 1200 °C. They found that the chemical composition and free carbon content of SiOC ceramics can affect the final SSA and pore size distribution of the SiOC-CDC materials, which further affect their hydrogen and methane storage capacities [329].

4. Microstructure of PDCs

4.1. Overview

As mentioned above, the amorphous PDCs will undergo a devitrification processes when they are subject to elevated temperature conditions, leading to the formation of amorphous multiphase systems via redistribution reactions of the chemical bonds (*i.e.*, phase separation) and, subsequently, to the nucleation and coarsening of nanocrystals (*i.e.*, crystallization). Particularly, the free carbon phase after phase separation is subjected to a graphitization process, which plays an important role in the microstructural evolution of PDCs. Following the phase separation and crystallization, the decomposition of PDCs occurs at higher temperatures (≥1500 °C) with the releasing of gaseous products (*e.g.*, CO, SiO, or N_2) generally because of the carbothermal reactions between the free carbon and oxygen- or nitrogen-containing phases. The high-temperature properties of PDCs such as the resistance to phase separation, crystallization and thermal degradation depend to a large extend on the microstructure of amorphous phase which is strongly related to the molecular structure and composition of the associated preceramic precursors [304].

In addition, PDCs consist of nanodomains that persist up to very high temperatures, which is one of the most intriguing characteristics of this class of materials. The nanodomains are firstly discovered by small-angle X-ray scattering (SAXS) in the Si(B)CN ceramics with the size ranging from 1 to 5 nm and then in the SiOC ceramics [336–339]. In several studies, the nature of nanodomains was proposed to be the basis for the remarkable resistance of PDCs to crystallization [338,340–342].

The microstructure of PDCs has been comprehensively investigated by various techniques that can be classified into two categories. In the first category, the techniques can provide average or integral information of the microstructures, such as X-ray diffraction (XRD), small-angle X-ray scattering (SAXS), small-angle neutron scattering (SANS) as well as MAS-NMR, FTIR and Raman spectroscopy. In the second category, the techniques are able to provide the information regarding the local properties at the nanometer scale, *e.g.*, scanning electron microscopy (SEM), transmission electron microscopy (TEM), electron energy loss spectroscopy (EELS) and energy-filtered transmission electron microscopy (EF-TEM). The detailed information of these techniques can be found in the previously published reviews [18] and will not be presented herein. Furthermore, theoretical studies and simulations have also been used to characterize the microstructures of PDCs because current experimental techniques sometimes are difficult to ascertain the detailed molecular/atomic structures and how they influence the properties of PDCs, particularly those related to the nanodomains [340,341,343–346]. Thus, several modes have been developed for explaining the relationship between the microstructure and properties of PDCs [31,336,340,343].

Polymer-derived silicon oxycarbide (SiOC) and silicon carbonitride (SiCN) based ceramics are two typical PDCs possessing unique microstructures and resultant interesting properties, which are hard to observe in other materials [31]. The SiOC-based ceramics can be characterized as amorphous materials with silicon atoms tetrahedrally coordinated by oxygen and carbon atoms [31,36,179,347]. Thus, within the SiOC-based ceramics, SiC_4, SiC_3O, SiC_2O_2 and SiO_4 tetrahedral units (so-called "mixed bonds") can be clearly detected by solid-state MAS NMR spectroscopy [31,348]. The carbon atoms have two hybridization methods. One is sp^3 hybridization which is for the C−Si bond in the Si-based ceramic matrix (*i.e.*, carbidic carbon), and the other one is sp^2 hybridization which is for the C−C bond in the segregated or free carbon phase (*i.e.*, graphitic carbon). In 2005, a classic model was proposed by Saha et al. for the microstructure of SiOC-based materials (see Fig. 7a) [209,338]. This model (referred to hereafter as Model 1) is consistent with the SAXS and solid-state MAS NMR data as well as the experimentally determined properties of SiOC ceramics (*e.g.*, high creep resistance and unique viscoelastic behavior). In accordance with the Model 1, three constituents construct the SiOC-based ceramics: *(1)* clusters of silica tetrahedra that form the heart of the nanodomains; *(2)* the graphene cage-like network that encases the nanodomains and *(3)* the monolayer of SiC_xO_{4-x} mixed bonds ($0 \le x \le 4$) that interconnect the silica clusters with the graphene network. Thus, the graphene layers and the SiC_xO_{4-x} mixed bonds form the interdomain boundary of the silica nanodomains. The SAXS data suggested that the diameters of the silica-rich nanodomains are in the range of 1 to 5 nm, while the widths of the interdomain boundaries (or domain walls) were found to range from 0.8 to1.5 nm [338].

In addition to Model 1, another model (referred to hereafter as Model 2) consisting of two continuous interpenetrating phases (*i.e.*, silica-rich phase and free carbon) and a carbon-rich SiO_xC_{4-x} interface (Fig. 7b) was also proposed. In Saha's work, the Model 2 was ruled out because it was not consistent with the unique creep and viscoelastic behavior of the tested SiOC ceramics [209,338]. In 2010, Widgeon et al. investigated the fractal spatial distribution of the SiC_xO_{4-x} structural units based on high-resolution ^{29}Si NMR spin-lattice relaxation studies [348]. They found that the structure of the tested SiOC ceramics consists of a continuous mass fractal

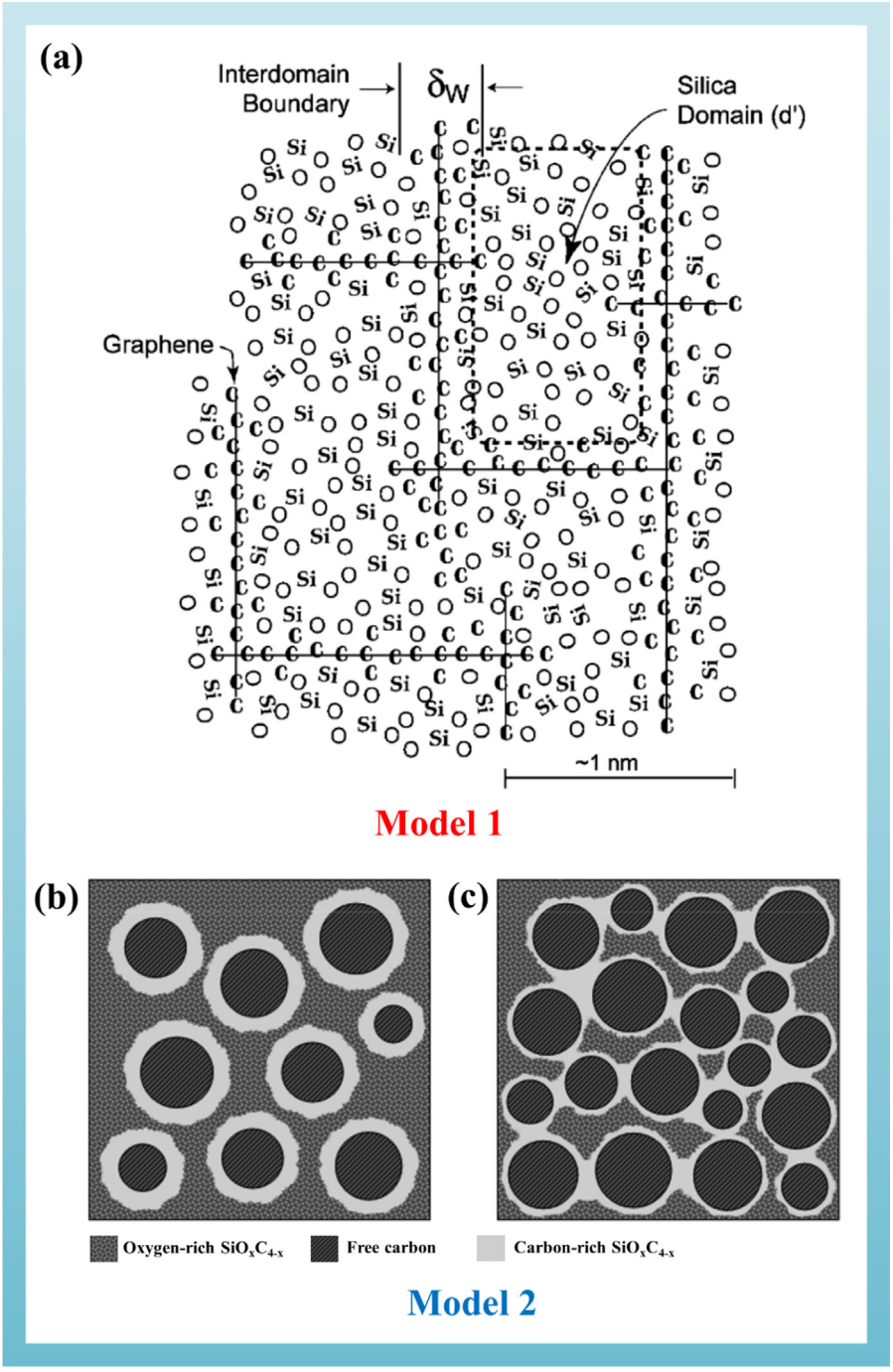

Fig. 7. Two proposed models for the nanodomain structures in polymer-derived SiOC ceramics [209,338,348].

backbone of corner-shared SiC_xO_{4-x} tetrahedral units with "voids" occupied by free carbon nanodomains, which is more consistent with the proposed Model 2 (Fig. 7b). In this model, the oxygen-rich SiC_xO_{4-x} units with $x < 2$ are located at the interior of this backbone with a mass fractal dimension of ~2.5 (instead of 3), which is a typical dimension for a tri-dimensionally homogeneous space filling/distribution. The carbon-rich units with $x \geq 2$ display a slightly lower dimensionality (2.1–2.3) and occupy the interface between the backbone and the free carbon nanodomains. Moreover, for the carbon-rich SiOC ceramics, the structure may also contain spatially bicontinuous nanodomains of free carbon and SiC_xO_{4-x} structural units (Fig. 7c) [348]. The experimentally characterized mass-fractal dimension of the oxygen-rich SiC_xO_{4-x} units however is not completely consistent with the presence of isolated silica-rich nanodomains as suggested in the structure discussed in "Model 1". Actually, the mass-fractal dimension for such finite (*i.e.*, isolated)

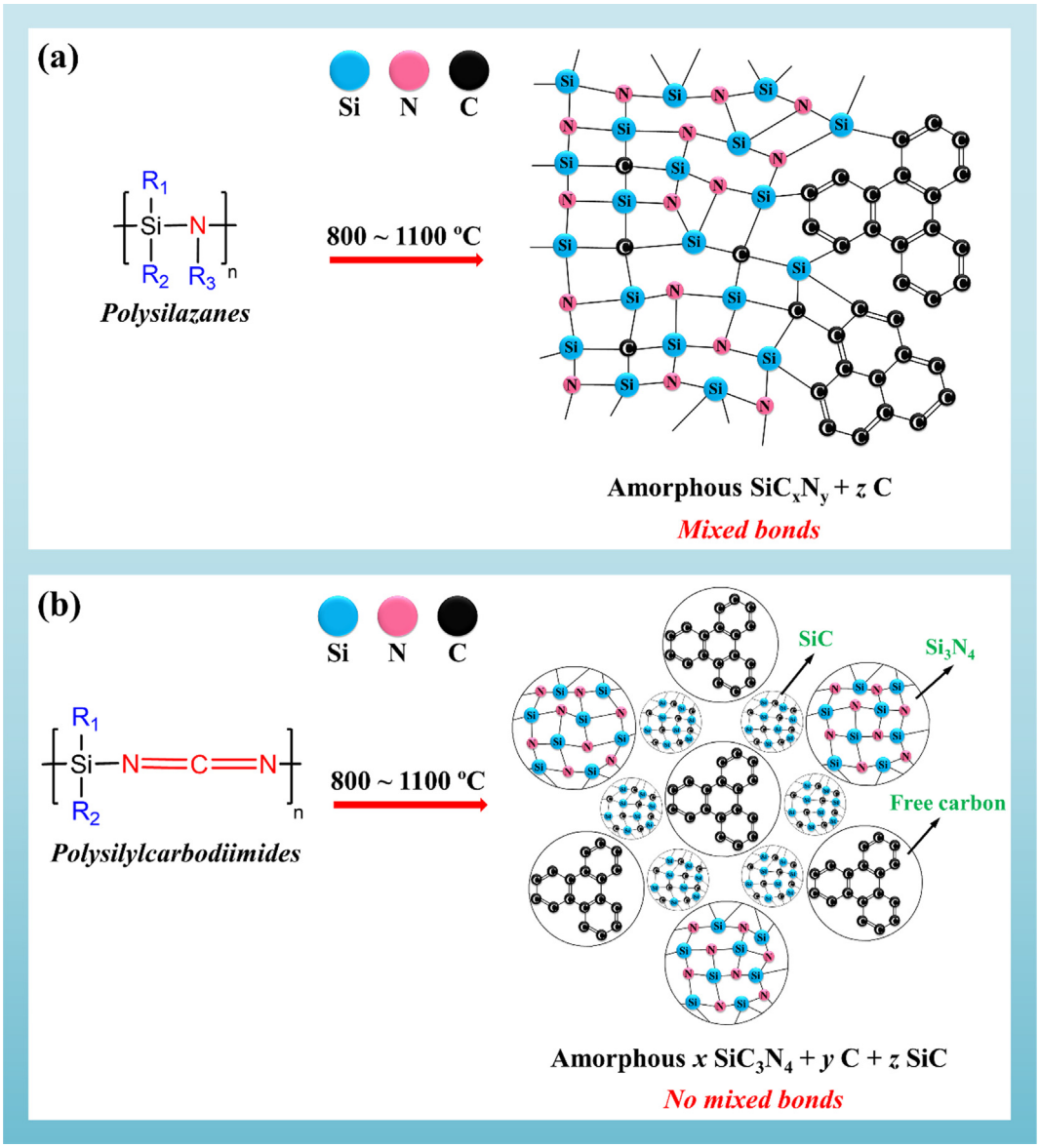

Fig. 8. Schematic illustration of the microstructure of amorphous SiCN ceramics derived from polysilazanes (a) and from polysilylcarbodiimides (b) [18,31].

clusters should be significantly lower than 2.5 [348,349].

In the case of SiCN-based ceramics, a least two classes of microstructures can be expected after pyrolysis of the preceramic polymers at 800–1100 °C, depending on the different molecular structures of preceramic polymers (Fig. 8) [82]. Within the polysilazane-derived SiCN ceramics, a single amorphous SiCN phase with tetrahedrally coordinated Si atoms bonded to either nitrogen or carbon or a mixture of carbon and nitrogen (*i.e.*, SiC_xN_y) as well as a free carbon phase can be identified via solid-state NMR spectroscopy (Fig. 8a). In contrast, the polysilylcarbodiimide-derived SiCN ceramics consist of a separated amorphous Si_3N_4 phase and a free carbon phase. No significant concentration of SiC_xN_{4-x} mixed bonds can be detected in the polysilylcarbodiimide-derived SiCN ceramics [176,350–352]. In the case of carbon-rich polysilylcarbodiimides, three amorphous phases composed of Si_3N_4, free carbon, and dispersed SiC nanodomains can be analyzed in the resultant SiCN ceramics (Fig. 8b) [176], which has been confirmed by elemental analysis, calorimetry [353], electrical conductivity, and SAXS analysis [339]. The formation of these two different amorphous structures in the SiCN ceramics leads to distinct thermal stabilities against crystallization. With an analogous C/Si ratio, the amorphous SiCN ceramics obtained from polysilazanes crystallize at temperatures 50–100 °C lower than that derived from polysilylcarbodiimides [18].

Similar to the SiOC ceramics, the X-ray amorphous SiCN ceramics are not strictly amorphous because they contain short-range structural features, namely nanodomains. As mentioned above, the nature of nanodomains is the basis for the excellent resistance of

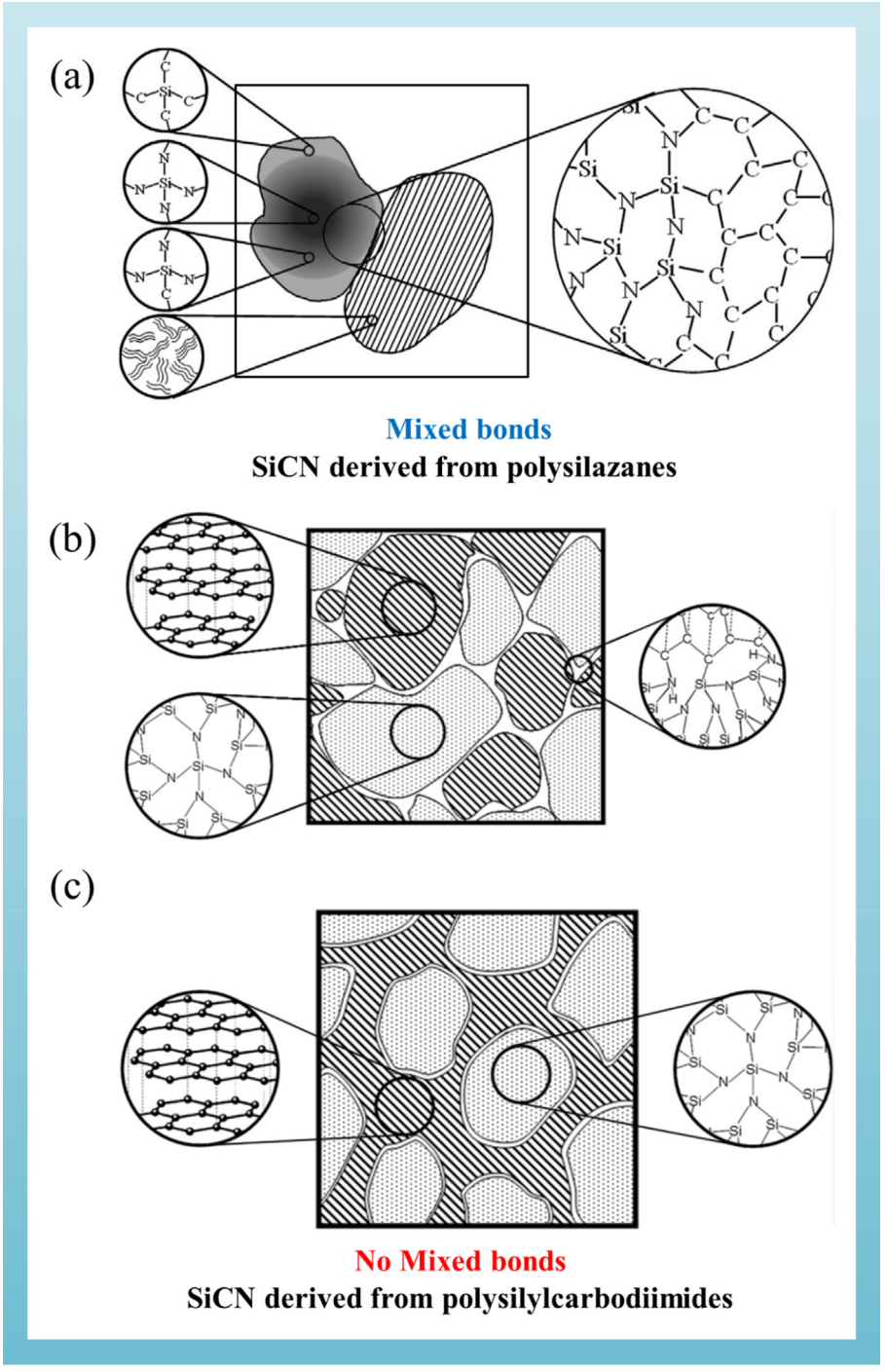

Fig. 9. Proposed nanodomain structural models for SiCN ceramics derived from precursors with different molecular structures at 800 °C. Model (a) reflects the situation in SiCN ceramics derived from polysilazanes, which are comprised of a Si-containing area (filled with black color) and a free carbon area (filled with stripes). Within the Si-containing area, there are SiN_4 domains, SiC_4 domains and SiC_xN_{4-x} interfacial domains with mixed bonds [355]. Models (b) and (c) represent polysilylcarbodiimide-derived SiCN ceramics with carbon content of 39.16 wt% and 57.37 wt%, respectively. The nanometer-scale amorphous/turbostratic carbon and Si_3N_4 nanodomains are shown with stripes and dots, respectively, and the white regions are interfacial areas. Model (c) describes a carbon-rich SiCN with Si_3N_4 nanodomains embedded in a continuous matrix of amorphous/turbostratic carbon [354]. The atomic structures in these nanodomains are shown schematically in the insets.

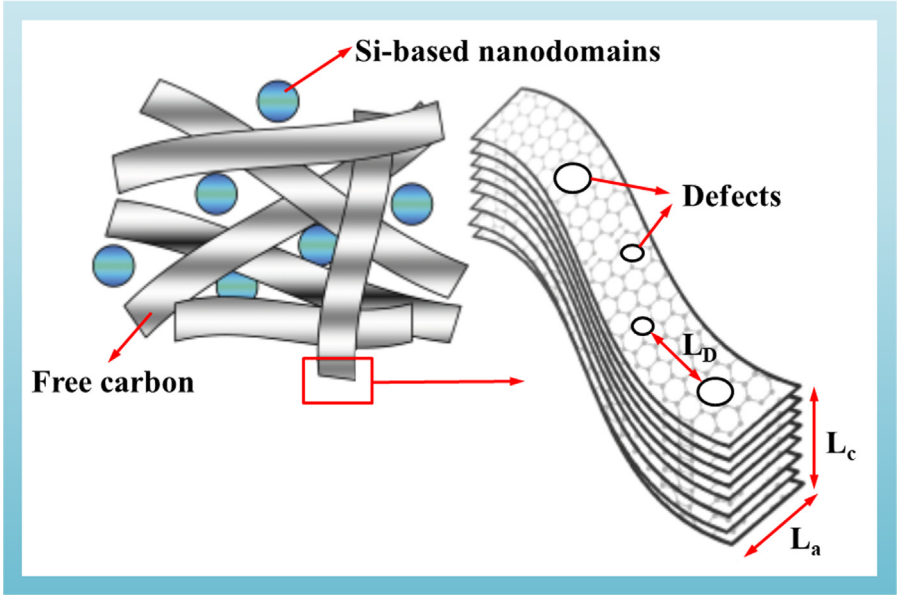

Fig. 10. Model illustrating the structure of free carbon nanodomains in PDCs. L_a represents the in-plane crystallite size of graphitic carbon or lateral cluster size along the sixfold ring plane of the amorphous or turbostratic carbon; L_c is the crystallite thickness of graphitic carbon or stacking thickness of turbostratic carbon; L_D is the inter-defect distance between two defects in one free carbon nanodomain [31,339].

PDCs to crystallization even at ultrahigh temperatures. The characteristic nanodomain microstructures are schematically illustrated in Fig. 9 [354,355]. Within the polysilazane-derived SiCN ceramics, the silicon atoms are tetrahedrally coordinated by carbon and nitrogen via sp^3-hybridization, forming SiC_xN_{4-x} mixed bonds ($0 \leq x \leq 4$) in the SiCN nanodomains, and the carbon atoms are bonded to each other through sp^2-hybridization in the free carbon nanodomains (Fig. 9a) [82,356,357]. Differently, no SiC_xN_{4-x} mixed bonds (only SiN_4 tetrahedral bonds) appear in the nanodomains of the polysilylcarbodiimide-derived SiCN ceramics despite that some SiC_xN_{4-x} mixed bonds may be present at the interfaces of the Si_3N_4 and free carbon nanodomains (Fig. 9b and c) [354]. The SAXS and TEM reveal that the sizes of the nanodomains are 1–3 nm and they gradually increase with the annealing temperature [31,337,354]. Moreover, the model for the structure of the free carbon nanodomain has also been proposed in literatures (Fig. 10) based on TEM images and Raman spectra of PDCs [31,339]. Three parameters (L_a, L_c and L_D) can be used to describe the general status of the free carbon nanodomains (will be discussed later).

The microstructure of other PDCs (*e.g.*, SiC, Si_3N_4, SiBCN) after pyrolysis can also be described using the nanodomain model. For instance, the amorphous SiC ceramics derived from polycarbosilanes consist of amorphous SiC nanodomains with sp^3 hybridized Si—C bonds and free carbon nanodomains with sp^2 hybridized C—C bonds. The interface of these two nanodomains may contain SiC_xO_{4-x} mixed bonds due to the oxygen contamination [188]. The amorphous Si_3N_4 ceramics obtained from thermal ammonolysis of perhydropolysilazane are composed of amorphous Si_3N_4 and Si nanodomains [358]. The SiBCN ceramics prepared by means of pyrolysis of the boron-doped polysilazanes generally consist of amorphous SiCN, free carbon and BC_xN_y nanodomains [156,336]. Particularly, with the incorporation of boron the thermal stability of the SiBCN is highly improved due to the formation of BC_xN_y intergranular nanodomains [14,156,359,360].

4.2. Microstructural characterization of the in situ formed carbon

4.2.1. Transmission electron microscopy (TEM)

As aforementioned, a main feature of PDCs is their capability to incorporate free carbon into the microstructure. In order to deeply understand the fate and role of free carbon, numerous techniques have been employed to collect the information of free carbon in the PDCs. TEM combined with selected-area electron diffraction (SAED), energy-dispersive X-ray spectroscopy (EDX or EDS) as well as electron energy loss spectroscopy (EELS) have been widely used to directly characterize the morphology, crystallinity, distribution and structural evolution of the free carbon within the PDCs because this technique can provide the information regarding the local properties of the materials at the nanometer scale [41,179,194,208,361,362].

Generally, the PDCs prepared through pyrolysis at 800–1100 °C are characterized by a random glassy network. The size of free carbon phase in the PDCs pyrolyzed at temperatures lower than 1200 °C is rather small [41,163,166,179,189,363,364]. Thus, in the SiOC-based ceramics pyrolyzed at 1000–1100 °C, only the so-called basic structural units (BSU) of the free carbon with few lamellar carbon layers can be observed (Fig. 11a) [178,347]. It's hard to image free carbon phase in the SiCN-based ceramics pyrolyzed at 1000 to 1100 °C (Fig. 11) [364]. In some SiCN and SiBCN ceramics the free carbon layers cannot be detected even after annealing at 1400 °C due to their excellent crystallization resistance [41,163,365].

In the PDCs heat-treated at temperatures ≥1400 °C, the lattice fringes of the free carbon with an interplanar distance of around

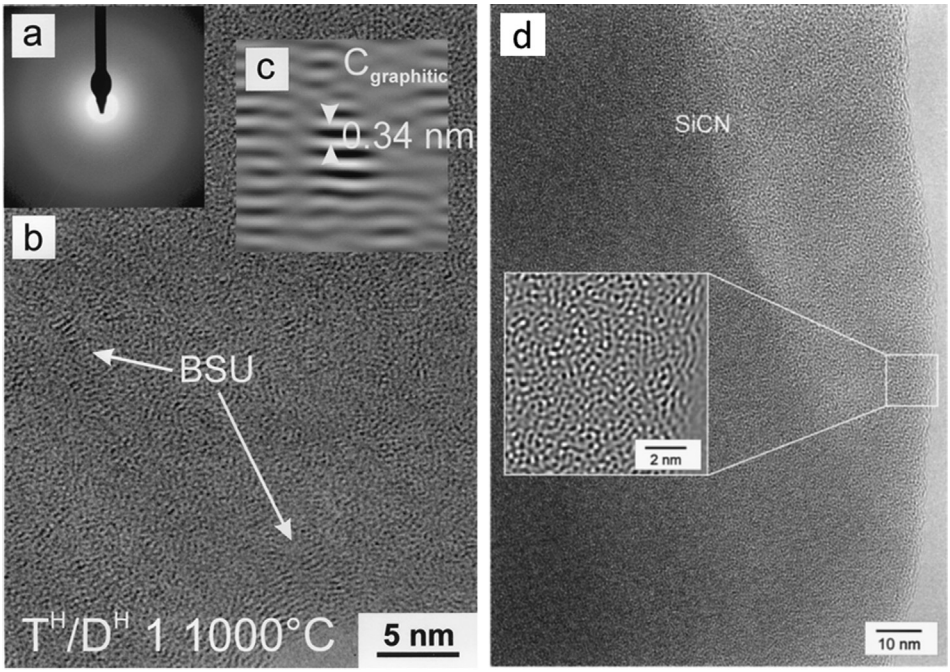

Fig. 11. High-resolution TEM micrographs of the typical amorphous structure of SiOC (b) and SiCN (d) pyrolyzed at 1000 °C (reprinted with permission of Wiley) [163,178]. The inset (a) displays the selected area electron diffraction (SAED) patterns, indicating the amorphous feature. The inset (c) shows a basic structural unit (BSU) of free carbon with an interplanar distance of around 0.34 nm between the graphene layers [178].

0.34 nm become clearer (Figs. 12 and 13) [188,194,361,366–368]. The grain sizes of free carbon clusters enhance with increasing of carbon content and heating temperatures, and the entangled carbon ribbons forming a percolation network can usually be observed in the carbon-rich PDCs (Figs. 12 and 13) [163,165,179,189,329,362,368]. Moreover, it should be noted that, in order to clearly image turbostratic carbon, different defocus settings can be utilized since the free carbon and ceramic matrix might be imaged better under different focusing conditions (see Figs. 12c and 12d) [41,361].

Interestingly, after introducing transition metal elements (*e.g.*, Hf, Ti and Ta) into PDCs, some free carbon with totally different morphology appears [245,310,368]. For instance, within a SiC/HfC(N)-based ceramic nanocomposite, the presence of a unique core–shell structure has been identified (Fig. 13a–c), *i.e.*, the HfC_xN_{1-x} nanoparticles are encapsulated by an *in situ* formed carbon shell. The ceramic nanocomposite was prepared upon pyrolysis and subsequent annealing of a single-source precursor synthesized by means of chemical modification of a commercially available allylhydridopolycarbosilane (SMP10, Starfire system, USA) by a tetrakis (dimethylamido)hafnium (IV) [$Hf(NMe_2)_4$] compound. As shown in Fig. 13b, the carbon shell is highly disordered and totally different from the carbon ribbons that appear in the same samples even after annealing at 1700 °C [368]. After further annealing, the samples heat-treated at 1900 °C the amorphous carbon shell significantly graphitizes, and typical lattice fringes of the graphitic carbon appear (Fig. 13c) [369]. Interestingly, Wen et al. found that, after annealing at the same temperature, the carbon shell on the HfC_xN_{1-x} core is much thicker than that on the TaC_xN_{1-x} core, and it is possible to tune the thickness of the carbon shell by forming $(Hf,Ta)C_xN_{1-x}$ solid solutions with different atomic ratio of Hf to Ta [310]. Within the SiC/C ceramics derived from SMP10 and without Hf, no carbon core/shell structure appears (Fig. 13d).

4.2.2. Raman spectroscopy

Raman spectroscopy is one of the most sensitive methods and an important nondestructive tool for characterization of the free carbon, particularly regarding its structural evolution at elevated temperatures [360–362,370–377]. Raman spectroscopy became a major experimental technique to characterize the microstructure of carbonaceous materials since 1970′s–1980′s, when Tuinstra and Koenig firstly reported an empirical relationship between the crystallite size (L_a) of carbon clusters (see definition in Fig. 10) and the intensity ratio of the two major Raman peaks of disordered non-graphitic carbon, and Lespade et al. gave the first theoretical explanation of this relationship [378,379]. After that, numerous researches on carbon materials using Raman spectroscopy were reported, such as diamond [380] and graphite [381], as well as glassy carbon [382] and a-C:H films [383,384]. The Raman spectra of free carbon in the PDCs were firstly reported in the characterization of SiC fibers in 1980's [377,385,386].

As shown in Fig. 14, the typical signals of free carbon in the first-order Raman spectra are the so-called D and G bands which are identified at approximately 1350 cm^{-1} and 1580 cm^{-1}, respectively. The G band is due to stretching vibrations of sp^2-carbon in the basal-plane of ideal graphitic lattice (*i.e.*, E_{2g}-symmetry, see Fig. 14b) [381]. The G band generally appears for highly oriented polycrystalline graphite (HOPG) or single graphitic crystals with L_a larger than 100 nm [387]. The D band is a defect-induced band, which corresponds to a graphitic lattice vibration mode with A_{1g}-symmetry (see Fig. 14b) and is well known to represent the

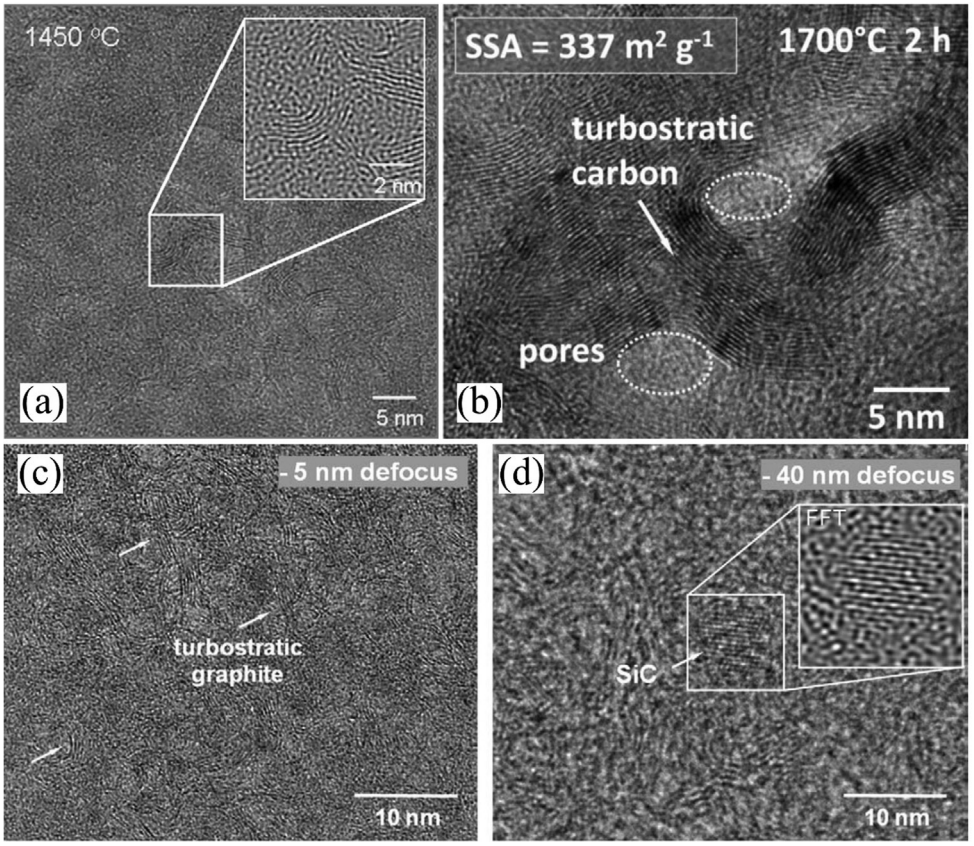

Fig. 12. TEM micrographs of a carbon-rich SiOC ceramic obtained at 1450 °C (a) and SiCN ceramic formed at 1700 °C (b) as well as of SiOC ceramic pyrolyzed at 1400 °C under different focusing conditions (c and d) (reprinted with permission of Elsevier) [179,361,362]. Insets in (a) and (d) are high-resolution TEM images clearly showing the lattice fringes of free carbon and β-SiC, respectively.

disordering of the free carbon [388]. The origin of the D band was attributed to double resonant Raman scattering after being debated for a long time [389,390]. In the Raman spectra of some PDCs, a shoulder (centered at ≈1620 cm^{-1}) at the high-wavenumber edge of the G band is visible and named D′ band (Fig. 14a), which is also defect-induced but corresponds to a graphitic lattice mode with E_{2g} symmetry [29,387,391]. The relative intensities of both the D and D' bands enhance with increasing wavelength (λ) of the excitation source because of resonance effects [392]. The difference is that the D band is mostly induced by the carbon atoms at the edge of graphene layers of polycrystalline carbonaceous materials consisting of large amount of small graphitic crystallites, whereas the D' band is assigned to a lattice vibration analogous to that of the G band but involving graphene layers at the surface of a graphitic crystal [387]. In addition, G′, D + G and 2D′ bands sometimes appear in the second-order Raman spectra of the PDCs at around 2700 cm^{-1}, 2945 cm^{-1} and 3245 cm^{-1}, respectively. All the analyzed bands in the second-order Raman spectra can be attributed to overtones and combinations of known lattice vibration modes. Accordingly, the G' band is an overtone of the D band (also named 2D band), which is usually found in defect-free graphite samples. The shape profile of the G' band provides information on the stacking thickness of graphene layers (*i.e.*, L_c, see definition in Fig. 10) [31]. The D + G band can be assigned to a combination of the G and D modes which is characteristic for disturbed graphitic structures. The 2D' band is the first overtone of the D′ band [387]. The intensity, position and width of these bands vary greatly depending on the structural organization of the ceramics and on the used excitation energy [31,393,394].

The intensity ratio of the D band and G band [I(D)/I(G)] in the Raman spectra is a measure of the structural disordering of free carbon. The higher the I(D)/I(G) value, the higher the disordering of free carbon [245,368]. Three primary reasons can be attributed to the disordering of the free carbon phase in PDCs: *(1)* the presence of edges in the graphene layers; *(2)* the deviation from planarity of graphene layers; and *(3)* the presence of carbon atoms in sp^3 hybridization state [31]. The I(D)/I(G) ratio can also be utilized to estimate the lateral crystallite size (*i.e.*, size of carbon clusters along the sixfold ring plane, denoted as L_a, see Fig. 10) of the carbon clusters [378]. Up to now, three correlations between the I(D)/I(G) and L_a values have been proposed. The first correlation between the L_a [nm] and the I(D)/I(G) ratio can be present as follows (named TK-correlation) [395,396]:

$$\frac{I_D}{I_G} = \frac{C(\lambda)}{L_a} \tag{4.1}$$

where I(D) and I(G) are peak amplitudes. $C(\lambda)$ is a wavelength-dependent pre-factor which can be calculated using the following

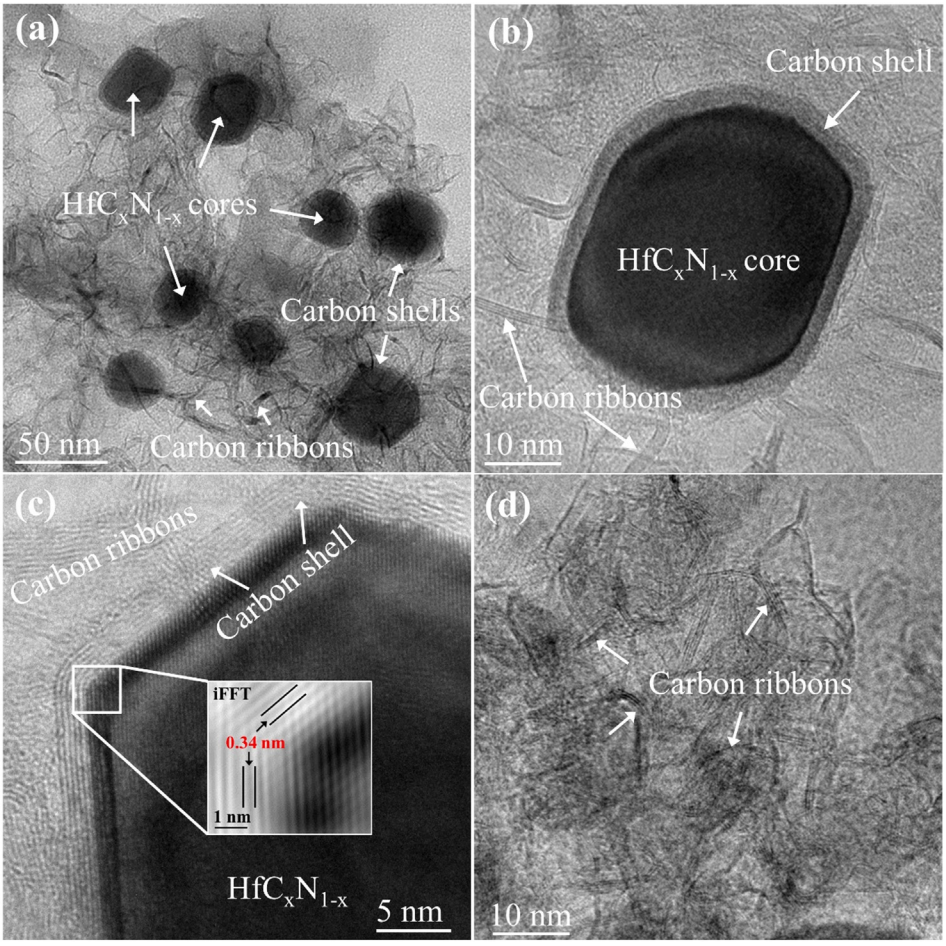

Fig. 13. TEM images of SiC/HfC$_x$N$_{1-x}$/C ceramics after annealing at 1700 °C (a and b), 1900 °C (c) and of SiC/C ceramics after annealing at 1700 °C (d), respectively (reprinted with permission of Wiley) [368,369]. The inset in (c) clearly shows the lattice fringes of free carbon with an interplanar distance of 0.34 nm [369].

equation:

$$C(\lambda) = C_0 + \lambda C_1 \tag{4.2}$$

where $C_0 = -12.6$ nm, $C_1 = 0.033$, and λ [nm] is the wavelength of the excitation source. This relationship is valid for 400 nm $< \lambda <$ 700 nm [392].

However, numerous evidence proved that the TK-correlation is invalid for the amorphous carbon clusters with L_a values lower than 2 nm [389,396]. Therefore, Ferrari and Robertson proposed the following correlation for $L_a < 2$ nm (named Ferrari-Robertson correlation) [396]:

$$\frac{I_D}{I_G} = C'(\lambda) \times L_a^2 \tag{4.3}$$

where $C'(\lambda)$ is a wavelength-dependent pre-factor (≈ 0.55 nm^{-2} at $\lambda = 514.5$ nm) [41].

Cançado and colleagues developed a general expression for the calculation of L_a [nm] from the I(D)/I(G) ratio, in which the excitation laser energy (written here with the laser line wavelength λ, nm) is involved (named Cançado-correlation) [397]:

$$L_a = (2.4 \times 10^{-10})\lambda^4 \left(\frac{I_D}{I_G}\right)^{-1} \tag{4.4}$$

where, the laser line wavelength λ should be in the visible range. The I(D) and I(G) are integrated intensities.

Usually, the free carbon in PDCs is characterized using a visible-laser Raman spectroscopy with the wavelength of 514.5 nm, and the I(D)/I(G) values are generally in the range of 0–5 [41,191,307,329,339,355,362,376,383,398,399]. Up to now, several L_a values have been estimated using the three correlations mentioned above, and the values amount to around 1 to 20 nm depending on different PDC samples [41,58,176,339,355,364,366,372,374,375,383,398,400,401]. Nevertheless, the estimation of the L_a based on

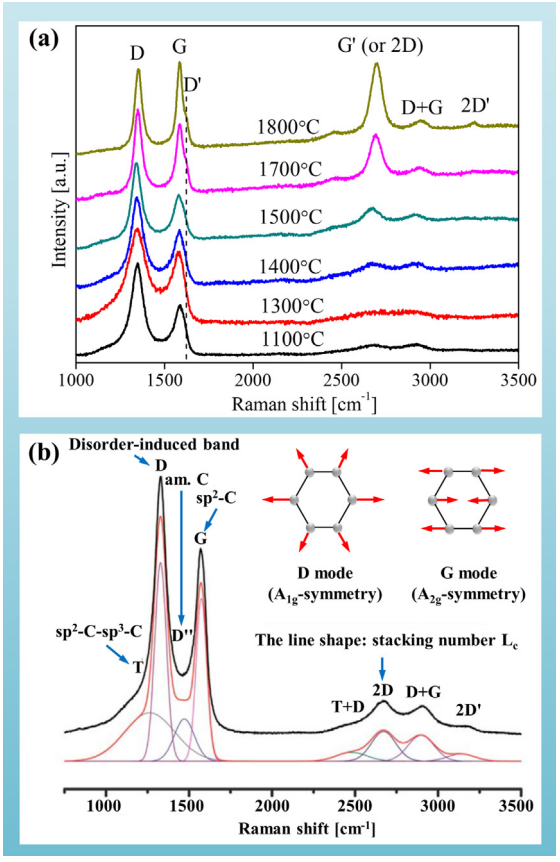

Fig. 14. Raman features of free carbon phase evolution in PDCs as a function of heating temperatures (a) and the characteristic carbon Raman modes and their definition (b). The spectra in (a) were recorded on a SiC/HfC(N)-based ceramic derived from a hafnium-modified allylhydridopolycarbosilane [245], and the spectra in (b) were collected on a carbon-rich SiCN ceramic derived from poly(phenylvinyl)silylcarbodiimide [31].

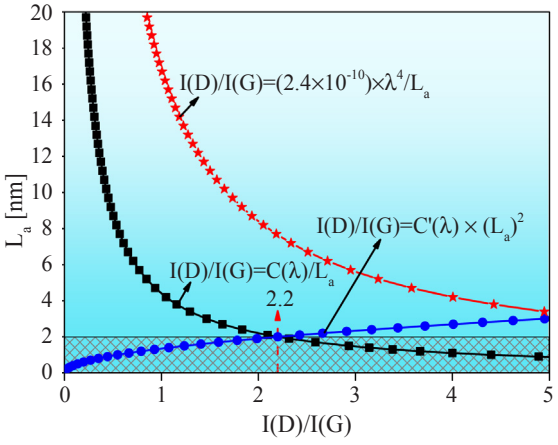

Fig. 15. Relationship between the intensity ratio I(D)/I(G) and the lateral crystallite size of carbon L_a according to the three different correlations. Here, λ is 514.5 nm. *C(λ)* and *C'(λ)* are 4.4 nm and 0.55 nm^{-2}, respectively.

the I(D)/I(G) values should be taken with caution. The relationship between the I(D)/I(G) and L_a values is plotted according to the three correlations (Fig. 15) using the mostly used laser wavelength (514.5 nm). The TK-correlation and Cançado-correlation show the same trend, but the calculation method of the intensities of the D and G bands is different (the former uses peak amplitudes, while the latter uses integrated intensities). If only the Cançado-correlation is applied for estimation, the L_a values will be always larger than 2 nm because the I(D)/I(G) values of the PDCs is seldom larger than 8.4 (when λ = 514.5 nm). When TK-correlation and Ferrari-

Robertson correlation are used for estimation, there will be also some problems. For instance, if the I(D)/I(G) ratio is lower than c.a. 2.2 (when λ = 514.5 nm), the L_a values estimated by both TK- and Ferrari-Robertson correlations are theoretically acceptable. However, this is not the truth. If the I(D)/I(G) ratio is higher than c.a. 2.2, the L_a values cannot be calculated by any correlation despite there must be a L_a value. Most importantly, these two correlations give an opposite trend. Accordingly, when calculating the L_a values of the PDCs, other complementary characterization techniques such as TEM and XRD are highly demanded in order to estimate the range of the L_a values first [366]. In addition, the extraction of the I(D)/I(G) ratio from the Raman data whether using the peak amplitudes or the integrated band intensities should be considered. One should also keep in mind that the L_a values are not always proportional to the annealing temperature and holding time in different PDCs due to the distinct chemical compositions and microstructural evolution [41,58,176,355,383,399–402].

Moreover, the inter-defect distance L_D (see definition in Fig. 10) could be estimated from the I(D)/I(G) ratio employing the following equation [403]:

$$\frac{I_D}{I_G} = \frac{C^{''}(\lambda)}{L_D^2} \tag{4.5}$$

where $C''(\lambda)$ is ≈107 nm^2 when the wave length λ is 514.5 nm. However, the equation is valid only when the L_D is larger than 6 nm [403]. That means the equation is invalid for high defect density, but it can still help us to compare the samples prepared in different processing routes.

When the heat treatment temperatures on the PDCs are not high enough (< 1300 °C), the D and G bands usually overlap to some extent, which complicates a separation of the profiles [41]. Thus, Gaussian, Lorentzian or Pseudo-Voigt fitting of the Raman bands can be performed in order to extract the precise I(D)/I(G) intensity ratios [389]. Furthermore, in order to improve the quality of the fitting curves via taking into account shoulders at the peak flanks, the so called minor bands are included. Consequently, the minor bands T (centered at ~1200 cm^{-1}, also named I band in some literatures, corresponding to sp^2-sp^3 bonds or C—C and C═C stretching vibrations of polyene-like structures) and D″ (appear at ~1500 cm^{-1}, attributed to the fraction of amorphous carbon contained in the samples) are included in the fitting curves of the Raman spectra of PDCs (see Fig. 14b) [41,387,389,390,404].

4.2.3. X-ray diffraction (XRD)

XRD is a powerful and quick method for the determination of grain sizes of the crystallized phases in the PDCs. The grain sizes, lattice parameters and weight fractions of different phases can be estimated by means of Rietveld refinement of the XRD patterns using appropriate functions [310]. For instance, the peak shapes can be modeled using the Thompson-Cox-Hastings pseudo-Voigt function for estimation of average grain sizes and the pseudo-Voigt function for lattice parameters and weight fraction [405]. Mera et al. estimated the L_c value of the free carbon nanodomains within the carbon-rich SiCN ceramics annealed at 2000 °C employing Rietveld refinement of the XRD patterns, and the result is ≈5.67 nm. Nevertheless, the amorphous free carbon in the PDCs cannot be detected. Generally, only the formation of graphitic carbon at very high temperatures (≥1900 °C) can be characterized by XRD method [29,362]. Moreover, the XRD measurement has a detection limit (1–2 vol%). As a result, identification of the free carbon with low concentration using XRD analysis is also impossible [18].

In addition, based on the XRD patterns, the lateral crystallite size (L_a) and the crystallite thickness (L_c) of the crystalized free carbon are proposed to be calculated using the Scherrer equations as follows [406–409]:

$$L_a = \frac{1.84\lambda}{B * cos\theta} \tag{4.6}$$

$$L_c = \frac{0.94\lambda}{B * cos\theta} \tag{4.7}$$

where B is the full width at half maximum (FWHM) of the diffraction peaks, λ the X-ray wavelength and θ the Bragg angle of the diffraction maximum. The diffraction peaks (0 0 2) and (1 0 0) are used for L_c and L_a, respectively [409]. Nevertheless, this method is rarely used in the PDC research field due to the relatively low concentration and low crystalline degree of the free carbon.

4.2.4. Magic angle spinning-nuclear magnetic resonance (MAS-NMR) spectroscopy

The MAS - NMR spectroscopy is one of the most accurate average techniques for the investigation of the type of coordination and of the local chemical environment of NMR sensitive elements (*e.g.*, ^{1}H, ^{29}Si, ^{11}B, ^{13}C, ^{15}N) in amorphous and crystalline PDCs. Actually, the phase-separation process in PDCs was originally discovered using NMR spectroscopy [18].

The free-carbon phase can be analyzed by means of ^{13}C solid-state MAS-NMR, which has been widely reported since 1990s [163,171,245,348,354,357,359,360,373,410–412]. The sp^2-carbon atoms in the free carbon cause a resonance in the ^{13}C spectrum at 120–150 ppm depending on the different local environment of the free carbon. This signal is distinct from that caused by the tetragonally-coordinated sp^3-carbon atoms with respect to the chemical shift values and spin-lattice relaxation time [163,383]. Consequently, it is easy to be identified in the ^{13}C NMR spectrum. Fig. 16 shows the ^{13}C NMR spectra of the polyvinylsilazane-derived powders after thermal treatment at different temperatures from 300 °C to 1500 °C. The signal for the sp^2-carbon atoms appears at c.a. 135 ppm in the ^{13}C NMR spectra of the samples heat-treated at temperatures exceeding 600 °C, indicating that the free carbon formed at around 600 °C in this system [373]. The broad nature of the peak indicates an amorphous structure of the initially formed free carbon phase. Actually, the MAS-NMR is one of the best methods to investigate the initial formation of free carbon in the PDCs because other techniques such as Raman spectroscopy, TEM, XRD generally have detection limits on the size of the free carbon

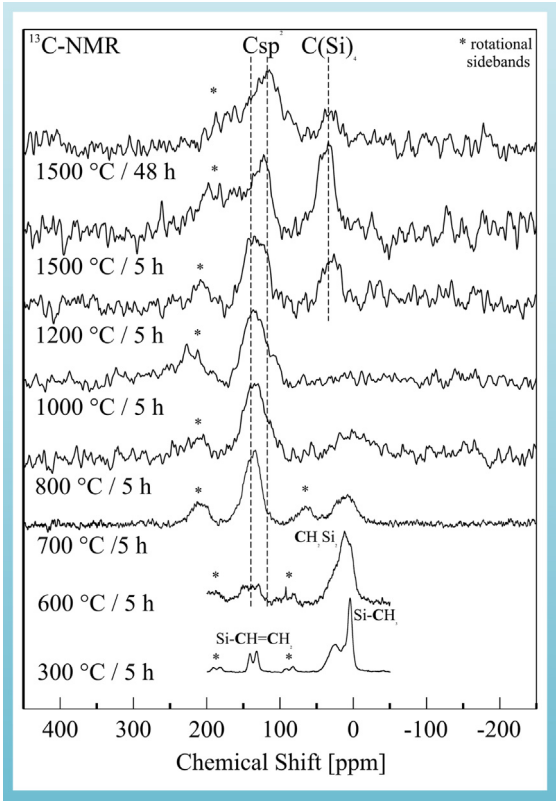

Fig. 16. ^{13}C MAS-NMR spectra of a polyvinylsilazane-derived powders heat treated at different temperatures from 300 °C to 1500 °C in N_2-atmosphere (asterisks denote spinning sidebands) (reprinted with permission of Elsevier) [373].

clusters [18]. After further annealing at elevated temperatures (1200–1500 °C), the NMR signals for the free carbon show a small high-field shift (from 135 to 125 ppm) and a narrowing (from 40 to 30 ppm) of the peak. This behavior can be attributed to an increased ordering of the free carbon which is probably caused by the elimination of hydrogen atoms bonded to the periphery of the free carbon [373]. Within some PDCs such as SiCN or SiBCN, the free carbon might be bonded to or doped with some other atoms (*e.g.*, Si, N and B), which causes the low-filed shift of the sp^2 resonance from ≈125 ppm to ≈150 ppm in the ^{13}C MAS NMR spectra [176,209,359,413,414].

4.2.5. X-ray photoelectron spectroscopy (XPS)

The evolution of free carbon in the PDCs can also be identified by characterization of the transition of chemical bonds using XPS, as the variation of the relative concentration of the chemical bonds can be calculated from the ratio of the integration areas underneath of their corresponding peaks in the XPS spectra [402]. The C−Si, C═C, and C−C/H bonds should be the main chemical bonds related to the free carbon, whose peaks appear in the XPS C 1s spectra with the binding energy of around 283.6, 284.4, and 285.0 eV, respectively [58,370,402,415–418]. The C−Si bonds (sp^3 hybridization) are mainly in the SiC-based ceramic matrix and partially in the SiCN-based ceramic matrix but are rare at the interface between the free carbon and the Si-based ceramic matrix. The C═C bonds (sp^2 hybridization) are primary chemical bonds in the free carbon phase. The C−C bonds (sp^3 hybridization) are in the aliphatic carbon chains of the precursors, which decrease with increasing of the pyrolysis temperature [402]. The C−H bonds (sp^3 hybridization) are generally present in the periphery of the free carbon within the PDCs obtained at temperatures lower than 1250 °C. Fig. 17 shows a typical C 1s XPS spectrum for an amorphous carbon-rich SiC(O) derived from a polycarbosilane (PCS), which indicates the existence of the C−Si, C═C and C−C/H bonds after deconvolution of the spectrum via Gaussian/Lorentzian fitting. The relative concentration of the chemical bonds can be estimated upon fitting as well. The increased C═C bonds and decreased C−C/H bonds suggest a sp^3-sp^2 transition with increasing pyrolysis temperature [402]. In addition to these chemical bonds, some other chemical bonds (*e.g.*, C−N/O, C═O and C═N with the binding energy of around 286.2, 288.1 and 287.8 eV, respectively) may also be found in some PDC samples [58,370,417]. However, these chemical bonds are rare in the free carbon phase or even in the PDCs, and they may come from the functional groups on the surface of the materials [370].

4.3. Structural evolution of the in situ formed carbon

Using advanced characterization techniques as mentioned above, the structural evolution of the *in situ* formed free carbon with

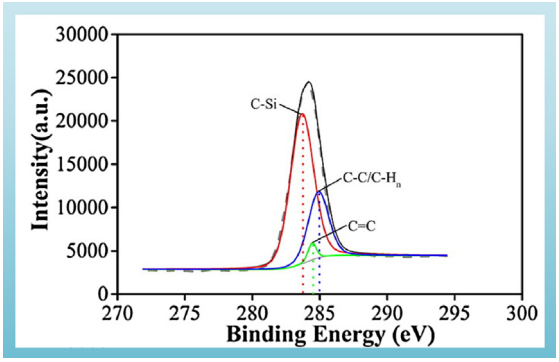

Fig. 17. XPS spectra of C 1s electron state obtained from an amorphous C/SiC(O) pyrolyzed at 1000 °C (reprinted with permission of American Chemical Society) [402].

increasing of temperature has been intensively studied [17,308,364,412,419–421]. With increasing thermolysis temperatures, the general trends can be summarized as the following four steps: *(1)* precipitation of hydrogenated amorphous excess carbon by decomposition of aromatic hydrocarbons; *(2)* nucleation of basic structural units (BSU); *(3)* growth of the turbostratic free carbon clusters via edge-to-edge linkage of BSUs; *(4)* graphitization of free carbon network or nanodomains [169,241,422,423]. Depending on the different molecular structure of the preceramic polymers (*e.g.*, polysiloxane or polysilazane, carbon-rich or carbon-poor polymers, rather linear or highly-branched), the onset temperature of the four steps varies to some extent [423]. Taking SiCN-based ceramics derived from polysilazane as an example, the typical structural evolution of free carbon in the PDCs can be schematically illustrated in Fig. 18.

The MAS NMR spectroscopy reveals that the initial precipitation of free carbon during the polymer-to-ceramic transformation starts at 600–800 °C, depending on the molecular structure of the polymers [245,423]. Using the EPR (or ESR) spectroscopy, the precipitation of excess carbon can be characterized in the carbon-rich samples pyrolyzed even at 400 °C [423]. The excess carbon is derived from the decomposition of aromatic hydrocarbons which come from the intermediately formed aliphatic hydrocarbons via cracking and reorganization during the heating process. Generally, at lower temperatures (< 800 °C), the hydrogenated excess carbon remains amorphous (mainly sp^3-hybridized) and homogeneously dispersed in the amorphous ceramic matrix (Fig. 18) [160].

With increasing pyrolysis temperatures (800–1000 °C), the carbon layers stack in turbostratic order, forming the basic structural units (BSUs) of free carbon (*i.e.*, nucleation) [169]. The BSUs are face-to-face associations of 2–3 three aromatic carbon layers (diameter < 1 nm) with sp^2-hybridiezed carbon atoms, which are the primary periodic aromatic entities to appear in most carbon materials. The initially formed BSUs are isolated to each other, and the peripheral carbon atoms are saturated by hydrogen atoms (Fig. 18). Accordingly, the ratio of sp^3 to sp^2 hybridization is still very high [189]. During the polymer-to-ceramic transformation process, the free carbon is always the first phase to nucleate at relatively lower temperatures [163,169,424,425]. Accordingly, after pyrolysis at 800–1000 °C, the PDCs mainly composes of a highly turbostratic free carbon phase and an amorphous Si-based ceramic matrix.

When the heating temperature rises up to 1000–1200 °C, the aromatic C-H groups in the periphery of the BSUs become not stable. Thus, the residual hydrogen atoms are removed as H_2 in this temperature range, inducing an unsaturation of the peripheral carbon atoms. The unsaturations are subsequently eliminated by the edge-to-edge linkage of neighboring BSUs, leading to the formation of elongated free carbon stacks with the length of around 3–4 nm and a significant transition of sp^3 to sp^2 hybridization (Fig. 18). Wang et al. estimate the activation energy for the sp^3-sp^2 transition of the free carbon within the polymer-derived SiC at 1000–1150 °C to be 3.4–3.8 eV, which agrees well with that in other carbonaceous materials (3.5 ± 0.9 eV) [195,426]. At temperatures higher than 1250 °C, almost no hydrogen atoms appear in the PDCs [188,189,399,423]. In addition, the large elimination of hydrogen at high pyrolysis temperature may destabilize such the mixed bonds at the interface between the free carbon and Si-based ceramic matrix and therefore lead to a gradual separation of free carbon phase from the ceramic matrix. This process generally occurs by means of bond switching events without significant atomic diffusion, as shown schematically in Fig. 19 [354].

After further heat treatment at elevated temperatures (> 1400 °C), the growth and rearrangement of free carbon regions continue and result in an entangled free carbon network or nanodomains with graphitic carbon nanocrystallites (Fig. 18). In this temperature range, a high-field shift of the peaks for free carbon in the ^{13}C NMR spectra, a narrowing of the Raman bands, a reduction of the I(D)/I(G) ratio, a change in the electron spin resonance (ESR) signal, and a ribbon-like carbon with clear lattice fringes and interplanar spacing (0.34 nm) in the high-resolution TEM images can be observed (see figures in Section 4.2) [163,383]. Delverdier et al. found in TEM micrographs that the length of the ribbon-like free carbon in the Si−C system (C/Si atomic ratio: 1.4) derived from polycarbosilane increases to 5–6 nm at 1400–1600 °C and up to 10–12 nm at 1800 °C. However, with increasing heating temperature, the number of carbon layers within a carbon ribbon does not change remarkable (always around 2–6 layers) [189].

When the processing temperature exceeds 1450 °C, obvious carbothermal reactions between the free carbon and oxygen- or nitrogen-containing phases (*e.g.*, SiO_xC_y, SiO_2, Si_3N_4) occur, leading to a significant degradation of the ceramics but dramatical grain growth of SiC phase. Please note that this temperature applies for the bulk ceramics. Actually, for the ceramics with high specific surface area, such as powders, the onset temperature for decomposition is significantly lower [116]. The following equations are

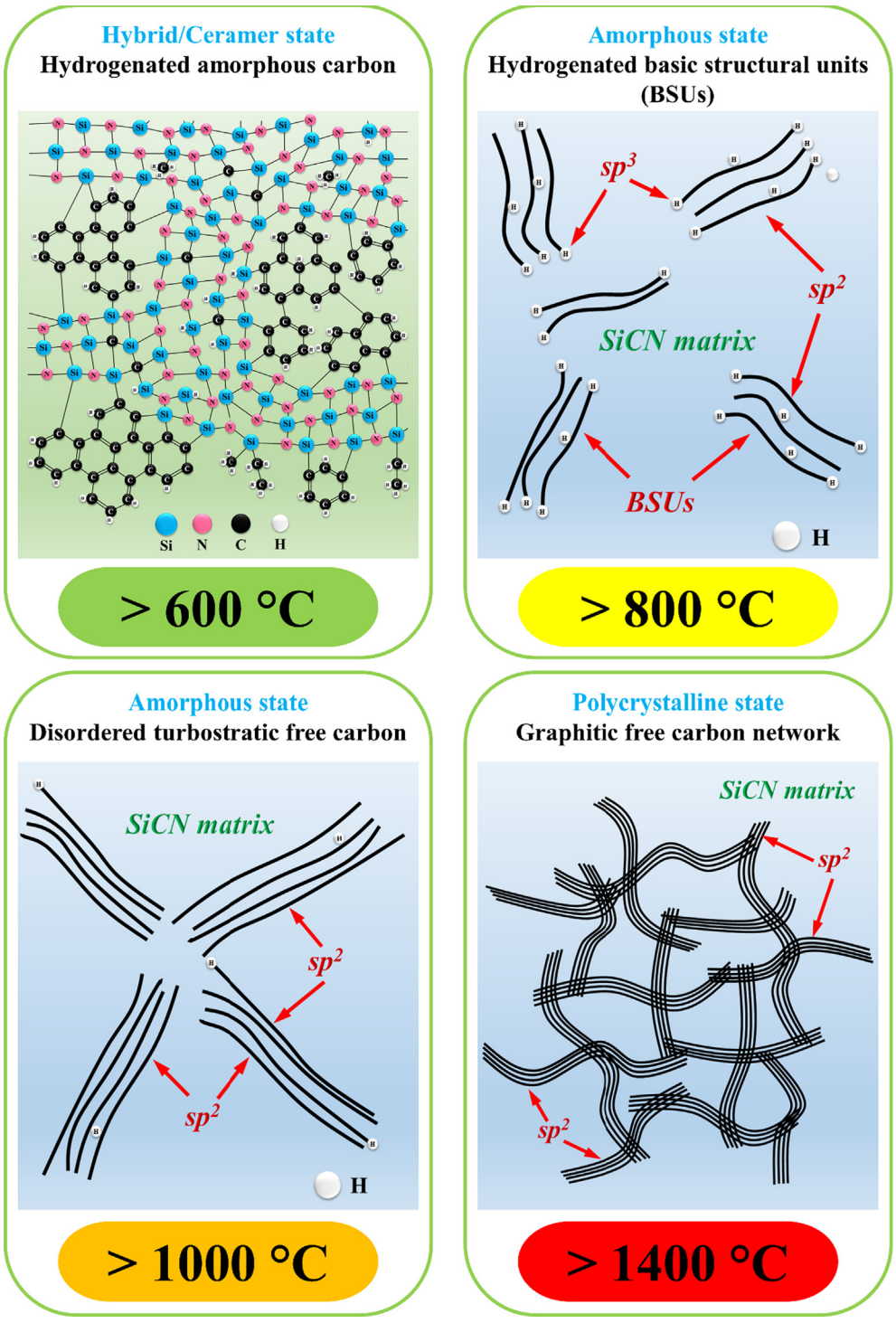

Fig. 18. Illustration of the structural evolution of free carbon during pyrolysis of preceramic polymers.

typical carbothermal reactions occurring in PDCs at temperatures ≥ 1450 °C:

$$SiO_xC_y(s) \rightarrow SiO(g) + (x-1)CO(g) + (y-x+1)C(s) \tag{4.8}$$

$$SiO_2(s) + C(s) \rightarrow SiO(s) + CO(g) \tag{4.9}$$

$$SiO(s) + 2C(s) \rightarrow SiC(s) + CO(g) \tag{4.10}$$

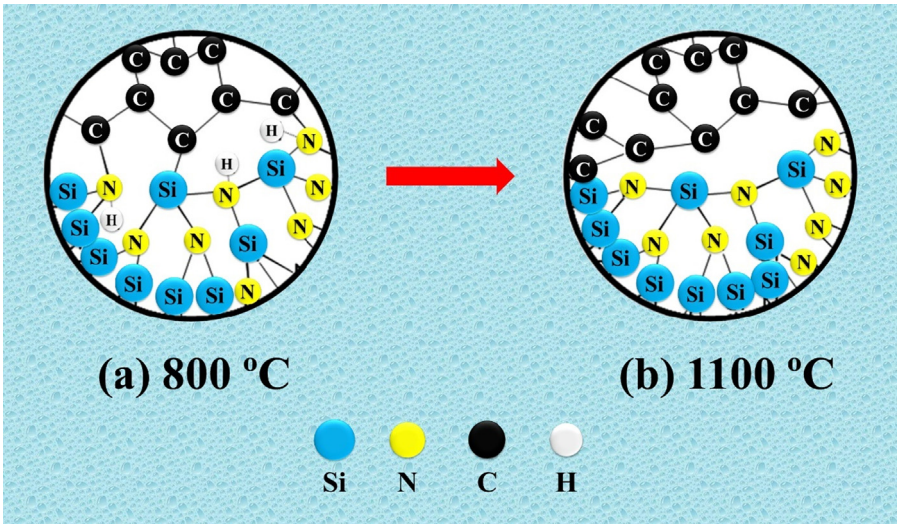

Fig. 19. Schematic representation of mixed bonds at the interface between the ceramic matrix and free carbon within a carbon-rich SiCN ceramic derived from poly(phenyl)silsesquicarbodiimide (a) as well as loss of hydrogen and of mixed bonds upon pyrolysis of the same polymer at 1100 °C, facilitated by local bonding switching (b) [354].

$$Si_3N_4(s) + 3C(s) \rightarrow 3SiC(s) + 2N_2(g) \tag{4.11}$$

where, Eqs. (4.8), (4.9) and (4.11) result in a degradation of the ceramic matrix, while equations (4.10) and (4.11) lead to the remarkable grain growth of SiC phase and elimination of free carbon [169,241,354,362].

Recently, An's group investigated the lateral size of the free carbon as a function of pyrolysis temperatures [58,355,402]. As shown in Fig. 20, with increasing pyrolysis temperature, the lateral size of free carbon in the SiAlCO ceramics decreases first and then increases at temperatures higher than 1200 °C [58]. This phenomenon has been analyzed in several PDC systems (*e.g.*, carbon-rich SiC, SiAlCO and SiCN), and it can be clearly interpreted by the Ferrari Model [396,427]. Firstly, the decrease in the lateral size at lower temperatures is due to the sp^3-sp^2 transition and rearrangement of distorted aromatic rings to six-membered rings. Secondly, the increase in the lateral size at elevated temperatures results from the in-plane growth of nano-polycrystalline graphite [58].

5. Influence of the *in situ* formed carbon on the microstructure of PDCs

5.1. Energetics consideration

The energetics of PDCs have been studied recently via a experimental calorimetry conducted in oxidative molten oxide solvents in order to know their thermodynamic properties [428–431]. The thermodynamic behavior of a material is a macroscopic manifestation of their atomic, nano- and micro-scaled structure and bonding. Particularly, the enthalpy of formation reveals the number, type, and strength of chemical bonds as well as the short-, mid- and long-range order within the materials [31]. The formation reaction of

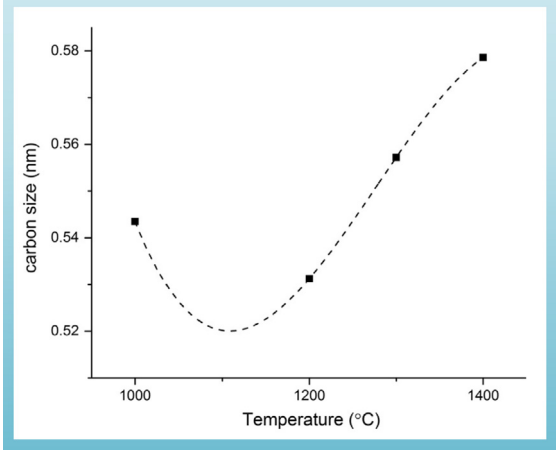

Fig. 20. Plot of the lateral size of free carbon as a function of pyrolysis temperature (reprinted with permission of Elsevier) [58].

amorphous $Si_xO_yC_z$ and $Si_xC_yN_z$ ceramics (x + y + z = 1) from their crystalline constituents at 25 °C can be written as the following equations [353,432]:

$$0.5y\ SiO_2\ (cristobalite, 25\ ℃) + (x - 0.5y)\ SiC\ (25℃) + (z - x + 0.5y)\ C\ (graphite, 25℃) \rightarrow Si_xO_yC_z (25℃) \quad (5\text{-}1)$$

$$(0.25z)\ Si_3N_4\ (\beta, 25\ ℃) + (x - 0.75z)\ SiC\ (25℃) + (y - x + 0.75z)\ C\ (graphite, 25℃) \rightarrow Si_xC_yN_z\ (25℃) \quad (5\text{-}2)$$

In the SiOC system, the calorimetric measurements reveal that the amorphous SiOC phase possesses a negative (exothermic) enthalpy of formation relative to their crystalline constituents (*i.e.*, SiC, cristobalite, and graphite). The $Si_xO_yC_z$ ceramics derived from a variety of precursors exhibit the enthalpy of formation mostly in the range of −20 to −70 kJ/mol, some of them can reach to −128 kJ/mol, indicating promising energetical stability. Up to now, there are no significant correlations between the enthalpies and the composition of the ceramics have been determined, but the enthalpies of formation from the elements (Si, O, C) become less negative (exothermic) as the amount of free carbon increases [428]. In the SiCN system, however, the enthalpy of formation of the amorphous SiCN phase relative to the crystalline constituents (*i.e.*, Si_3N_4, SiC, and graphite) is less negative than that of the SiOC phase, and some of them are near zero or slightly positive (≈4 kJ/mol). These materials seem to be stabilized by the entropy arising from disorder and amorphization [353]. Several amorphous SiCON ceramics show mainly negative enthalpy of formation from SiO_2, SiC, Si_3N_4 and graphite, and part of these values are substantially more negative than those of the SiOC or SiCN ceramics. However, their structure has not been characterized in detail [429].

Combined with solid-state MAS NMR spectroscopic measurements, the energetic stabilization of the SiCN (SiOC) ceramics can be attributed to the presence of mixed bonds (*i.e.*, Si atoms in the center of a tetrahedron containing both N (O) and C atoms) in the interfacial regions between the Si_3N_4 (SiO_2) and free carbon nanodomains [31,353,428]. The hydrogen in the ceramics seems to affect the calorimetric results by way of stabilizing the domain boundaries, but further systematic studies are needed [31,354].

5.2. Composition diagram analysis

Generally, the molecular formula of the SiOC and SiCN ceramics can be written as n SiC • $(1 - n)$ SiO_2 • x C and n Si_3N_4 • $(1 - n)$ SiC • x C ($0 \le n \le 1$, $x \ge 0$), respectively, for analysis. Fig. 21 shows the ternary composition diagram of the SiOC and SiCN ceramics. The diagrams possess two important tie lines, one is connecting the SiC and SiO_2 (or Si_3N_4) and the other between the carbon apex and SiO_2 (or Si_3N_4). Basically, the composition of the SiOC and SiCN ceramics with excess carbon after pyrolysis is lying within the triangle SiC-SiO_2-C and Si_3N_4-SiC-C (see points *X1* to *X6* in Fig. 21), respectively [35,104,428,433]. Using the straight line that passes through the points *X* and the carbon apex (the blue dotted line), the *n* and *x* values (*i.e.*, the mole fraction of free carbon) from the composition of the ceramics can be obtained [338]. For instance, the mole fraction of free carbon in *X1* and *X5* is larger than that in *X2* and *X6* despite the carbon content in *X1* and *X5* is lower than that in *X2* and *X6*, respectively. Moreover, the samples with the composition on the SiC-SiO_2 and Si_3N_4-SiC tie lines have no free carbon (*i.e.*, $x = 0$).

The diagram can be used to theoretically calculate the limits for the weight change of the PDCs as well as predict the variation of free carbon content. As shown in Fig. 21b, the composition diagram of SiOC allows a quick estimate of the amount of CO that would be lost via the carbothermal reaction as described in Eqs. (4.9) and (4.10). For instance, an initial composition of a SiOC ceramic is marked as *X3*, and then the weight loss can be estimated by considering the triangle SiC-CO-SiO_2. The removal of CO by carbothermal reaction means that the composition of the SiOC ceramic moves toward the SiC-SiO_2 tie line along the straight line passing through CO apex and point *X3* (*i.e.*, the red solid line in Fig. 21b), ending on the point Q on the SiC-SiO_2 tie line. Then, mole fraction of crystalline SiC remaining in the residue after completion of carbothermal reaction is n_Q, and the mole fraction of CO lost to volatilization (y_{co}) can be given by the following equations [434]:

$$y_{co} = \frac{a}{a + b} \quad (5.3)$$

The composition at point *K* represents the case of complete carbothermal reaction of silica by free carbon, producing stoichiometric SiC with releasing of CO gas. The composition points in the triangle SiC-SiO_2-K (*e.g.*, *X3*) yield SiC and SiO_2 after complete carbothermal reaction (*i.e.*, point Q), whereas the points in the triangle SiC-K-C (*e.g.*, *X4*) transform into only SiC and C after fully releasing CO (*i.e.*, point *R*) [434].

Regarding the SiCN ceramics, for example, one initial composition is shown by the point *X5* in Fig. 21c, which can be written as n_5 Si_3N_4 • $(1 - n_5)$ SiC • x_5 C. Basically, the change in the composition due to either reaction with atmospheric nitrogen (mass gain) or evolution of nitrogen via carbothermal reaction with free carbon (mass loss), must fall along the straight line that passes through the

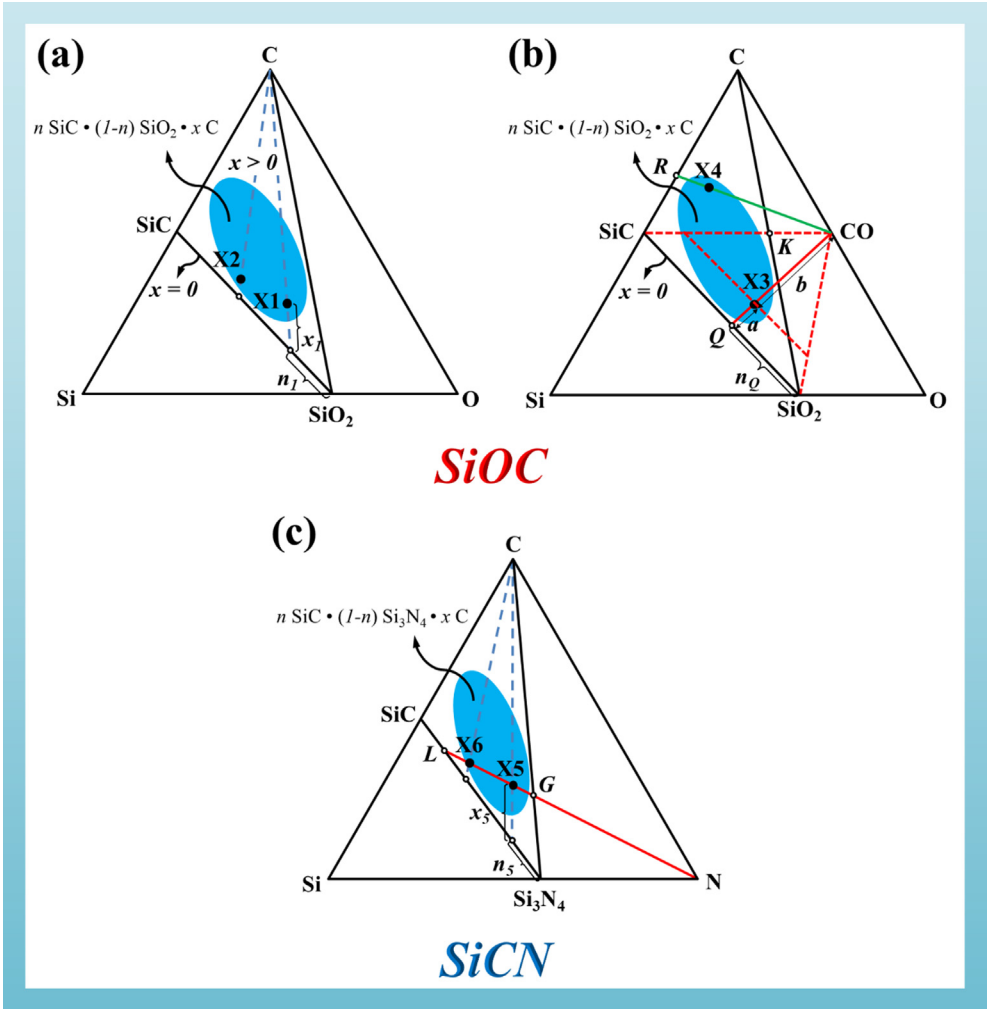

Fig. 21. Composition diagrams for SiOC *(a* and *b)* and SiCN *(c)* ceramics, denoted as n SiC • $(1 - n)$ SiO_2 • x C and n Si_3N_4 • $(1 - n)$ SiC • x C ($0 \leq n \leq 1$, $x \geq 0$), respectively.

point *X5* and the nitrogen apex (*i.e.*, the red solid line in Fig. 21c). Principally, the compositions of PDCs after either mass gain or mass loss are lying at the intersection of this straight line and the edges of the triangle Si_3N_4-SiC-C (*i.e.*, between the points *L* and *G* in Fig. 21c) [435]. Thus, points *L* and *G* represent the limits of mass loss and mass gain of the ceramics, respectively. The variation of free carbon content can be predicted via the combination of the two straight lines (*i.e.*, the blue dotted line and red solid line in Fig. 21c). For instance, the sample with the composition at point *X5* can transform to *X6* after high-temperature annealing (> 1500 °C) in an atmosphere with low nitrogen partial pressure and finally to point *L* with no free carbon in the residue [419,435,436]. The predictions have been proven by experimental results [419,434,436].

5.3. Crystallization and decomposition

The role of free carbon on the microstructural evolution of the PDCs with respect to crystallization and decomposition under different heat treatments is one of the most intriguing questions in this field of research. In former times, the free carbon was thought to be detrimental to the high-temperature stability of the final PDCs. The decomposition of SiOC phase as well as carbothermal reactions between the free carbon and the nitrogen- or oxygen-containing phases (*e.g.*, SiO_xC_y, SiO_2 and Si_3N_4) are considered as the main reason for the decomposition of PDCs at high temperatures [165,174,175,184,185]. However, in recent years, this view has been completely revised due to the fact that, under certain conditions, some higher free carbon-containing PDCs exhibit better resistance toward crystallization and decomposition than the carbon-poor PDC analogues [165–167,176,178–180,186,187]. Based on these investigations, it was concluded that the fine distributed free carbon within the PDCs is essential for the hindering of crystallization of the ceramics and lowering the carbothermal reactivity up to very high temperatures and, simultaneously, generates a complex microstructure of the PDCs [176,180,287,354,437–439].

5.3.1. Si-C system

The inhibiting effects of free carbon on the crystallization of SiC crystals have been found in several SiC-based ceramics derived from polycarbosilanes [180,287,438,439]. Delverdier and Monthioux compared the effects of free carbon on the crystallization behavior of SiC phase in two different SiC-systems: the Si-C system with C/Si atomic ratio of 1.4 and the carbon-enriched Si-C system with the C/Si atomic ratio of 2.1 [189]. They found that the grain growth of the SiC crystals can be divided into 2 steps due to the presence of free carbon: *(1)* the primary crystal growth and *(2)* the secondary crystal growth. The results show that an excess of free carbon delays the occurrence of the first SiC crystals by 100–200 °C and inhibits the primary crystal growth of SiC in the temperature range from 1000 to 1400 °C, due to that the free carbon phase forms a network of open cages around SiC crystals. The SiC crystals therefore are located in the cavities of this network, and the grain growth is only possible via diffusion processes (*e.g.*, structural rearrangements or migration of defects) at the interface between SiC crystals and intergranular phase. At higher temperatures (≥1500 °C), carbon depletion occurs due to the carbothermal reactions between the free carbon and oxygen containing phases (*e.g.*, SiO_xC_y) resulting from oxygen impurities of the starting material or the inert atmosphere. Accordingly, the carbon network is destroyed, and the SiC crystals are expelled from the carbon network, becoming free to coalesce by impingements. Under this condition, the SiC crystals can grow very fast by coalescence mechanism, which is regarded as the secondary crystal growth [189,439].

5.3.2. Si-O-C system

The influence of free carbon on the microstructure of PDCs can also be seen from the different high-temperature stability of the polymer-derived SiOC ceramics and a simple mixture of amorphous silica and carbon. The SiOC ceramics can be described by a structural model shown in Fig. 7, which consists of graphene sheets interconnected into a cellular network containing silica nanodomains. The graphene sheets and SiC_xO_{4-x} mixed-bonds (*i.e.*, the tetrahedra containing silicon bonded to both oxygen and carbon) constitute the domain walls which connect the graphene to the SiO_4 tetrahedra [338]. The SiOC ceramics after pyrolysis at 1100 °C is generally X-ray amorphous, and the amorphous state can persist up to very high temperatures [36,165,179,361,440]. Crystallization behavior of amorphous SiOC ceramics has been studied up to 1500 °C. In all cases, the crystallization product is reported to be only β-SiC, which comes from the carbothermal reaction between silica and free carbon or from decomposition of SiO_xC_y phase [434]. Interestingly, no cristobalite crystals appear at such a high annealing temperature despite that pure silica crystallizes into cristobalite at temperatures as low as 1000 °C [441–443]. The silica within the SiOC ceramics crystallizes into cristobalite only when the free carbon is removed by oxidation, proving that the free carbon plays an important role in the crystallization behavior of the SiOC ceramics [444]. The effect of free carbon on the crystallization resistance of SiOC ceramics is realized through its nanodomain structure, as the nucleation of silica crystallites requires the growth of embryos up to a critical size (a few nanometers). However, forming such a large nucleus requires diffusion of the silica over distance much longer than the size of the existing silica nanodomains, making it hard to reach the critical size of the nucleus of silica in a laboratory time scale [428,445]. In early studies, researchers attempted to improve the crystallization resistance of silica via physically adding carbon into it. However, this approach was neither successful in incorporating large amounts of carbon into silica nor did it produce a remarkable enhancement in the crystallization temperature of silica due to the essential insolubility of carbon in silica [446,447].

5.3.3. Si-C-N system

Polymer-derived ternary SiCN ceramics is a new class of PDCs exhibiting excellent thermal stability to exceptionally high temperatures [176]. There are two classes of precursors can be used for the SiCN ceramics, *i.e.*, polysilazanes and polysilylcarbodiimides. Recent researches suggest that the polysilylcarbodiimide-derived SiCN ceramics are thermally more stable than the analogous ones derived from polysilazanes due to the distinct microstructures (Fig. 8) [82,448,449]. One important reason for the excellent thermal stability of the SiCN materials in terms of degradation and crystallization resistance is the presence of nanodomains as discussed in Section 4.1 (Fig. 9) [337]. Mera et al. investigated the crystallization resistance of SiCN ceramics derived from polysilylcarbodiimides with different carbon content. The results indicate that the temperature of crystallization depends on the free carbon content. The carbon-rich SiCN ceramics with the highest free carbon content exhibit the highest thermal stability against crystallization [176]. Similar to the SiOC ceramics, the amorphous SiCN ceramics crystallize directly into α and β-SiC at temperatures exceeding 1500 °C via the carbothermal reaction between the free carbon and the amorphous Si_3N_4 phase, as shown in Eq. (4.11). The crystalline Si_3N_4 (α-/β-Si_3N_4) can only appear in the samples after annealing at temperatures ≥1500 °C despite that the carbon-free amorphous Si_3N_4 has been shown to crystallize readily at temperatures ≥1200 °C [352]. It is believed that the free carbon seals off the amorphous Si_3N_4 nanodomains and therefore inhibits its nucleation process. Moreover, the free carbon at the interface of the Si_3N_4 nanodomains can prevent the out diffusion of nitrogen and improve the thermal stability of Si_3N_4 clusters [437]. Within the carbon-rich SiCN ceramics, the crystallization of SiC and Si_3N_4 as well as carbothermal reaction occurs at even higher temperatures [176].

6. Effects of the *in situ* formed carbon on structural properties of PDCs

6.1. Mechanical properties

From the view point of history, the potential of PDCs was recognized due to its possibility for producing SiC-based ceramic fibers with high thermo-mechanical performance [4–10]. After decades of development, the tensile strength, Young's modulus and the high-temperature stability of SiC-based fibers have been improved significantly by means of tuning the chemical/phase composition of fibers by carefully controlling the chemical composition of precursors and optimizing the processing technologies (*e.g.*, replacing the oxygen curing process by electron-beam irradiation). The detailed progress has been reviewed in several literatures

Table 1
Density (ρ), free carbon content (C_{free}), processing temperature (T), Vickers hardness (H_v), Youngs' modulus (E), fracture toughness (K_{Ic}) and Poisson's ratio (υ) of pressureless sintered dense SiOC ceramics and amorphous SiO_2 (n.d. = not determined).

Samples	ρ [g/cm^3]	C_{free} [wt.%]	T [°C]	H_v [GPa]	E [GPa]	K_{Ic} [MPa m$^{1/2}$]	υ	Ref.
a-SiO_2	2.2	0	n.d.	6–7	72	0.77	0.17	[455,456,692]
$SiC_{0.33}O_{1.33}$	2.23	< 1	1000	8.6	n.d.	0.70	n.d.	[693]
$SiC_{0.375}O_{1.25}$	2.2	4.01	1000	10.6	n.d.	0.57	n.d.	[693]
$SiC_{0.33}O_{1.33}$	2.28	< 1	1200	8.4	102	n.d.	n.d.	[455]
$SiC_{0.43}O_{1.29}$	2.26	1.56	1200	9.2	102	n.d.	n.d.	[455]
$SiC_{0.49}O_{1.25}$	2.25	2.78	1200	9.3	113	n.d.	n.d.	[455]
$SiO_{1.60}C_{0.80}$	2.23	11.39	1100	6.4	101	n.d.	0.11	[456]
$SiC_{0.99}O_{1.25}$	2.32	12.2	1200	11.0	107.9	n.d.	n.d.	[453]
$SiC_{1.02}O_{1.21}$	2.16	12.3	1200	10.8	106.7	n.d.	n.d.	[453]
$SiC_{2.34}O_{1.06}$	1.95	30.6	1200	9.7	95.8	n.d.	n.d.	[453]
$SiC_{3.36}O_{1.00}$	1.83	40.7	1200	9.4	92.8	n.d.	n.d.	[453]
$SiC_{4.07}O_{1.18}$	1.82	52.7	1200	8.4	93.3	n.d.	n.d.	[453]
$SiC_{4.30}O_{1.20}$	1.82	54.2	1200	8.8	86.7	n.d.	n.d.	[453]
$SiO_{1.32}C_{6.43}H_{0.11}$	1.6–1.7	61	1100	5.5–8.6	66	n.d.	n.d.	[361]

[18,117,119,150,450]. Despite the claim of near stoichiometry, there is still a small amount of free carbon in the SiC fibers (*e.g.*, the C/Si ratio of the Hi-Nicalon-Type-S fibers is around 1.05) [117]. As a result, the role of free carbon on the mechanical properties of ceramic fibers cannot be ignored. Firstly, the elastic modulus of SiC-based fibers significantly varies as a function of C/Si ratio. The elastic modulus increases with decreasing free carbon content. However, the tensile strength of SiC fibers appears to be independent of chemical composition or crystallite sizes [175]. Secondly, the presence of free carbon clusters is considered to hinder the grain growth of SiC grains during fiber production and application at high temperatures because the free carbon phase forms an intergranular framework between the SiC nanocrystals (see Section 5.3.1) [117]. For instance, the free carbon in the Hi-Nicalon Type-S fiber limits the grain size of SiC grains to around 50 nm, which makes the SiC fibers possess good strength retention after exposure at 1600 °C in argon for 10 h. For a pure stoichiometric polycrystalline SiC fiber, an explosive growth of the grains and a catastrophic fall in strength may occur if a grain growth limiting mechanism is absent [451]. However, oxidation of free carbon in oxidative environment at high temperatures is harmful to the strength of the fibers. Moreover, at temperatures higher than 1200 °C, the decomposition product of SiO_xC_y phase can react with free carbon to form secondary SiC phase (SiO + C = SiC + CO), leading to a significant grain growth of the SiC crystals. Accordingly, nowadays researchers are seeking oxygen-free SiC fibers with appropriate free carbon content in order to improve the thermal stability but avoid the dramatical decreasing of mechanical properties at high temperatures [117,188,452].

In addition to fibers, the study of mechanical properties of bulk PDCs has been conducted for several years, and two systems have been investigated in some detail, *i.e.*, SiOC (Table 1) and SiCN (Table 2) systems. Generally, the effects of free carbon on the mechanical properties strongly depend on their grain size, content and distribution within the ceramic matrix [364,453]. Compared with vitreous silica, the SiOC ceramics exhibits significantly improved mechanical properties, such as Young's modulus, Hardness and creep resistance, due to the enhanced connectivity of the SiOC glass network upon the partial exchanging of bivalent oxygen by tetravalent carbon (*i.e.*, the presence of carbidic carbon) [207,454,455]. The unique mechanical properties are strongly affected by the *in situ* formed segregated carbon as well. As shown in Table 1, the Vicker's hardness of SiOC ceramics with low free carbon content (< 5 vol%) is determined to be 8–11 GPa, which is obviously higher than that of the vitreous silica (6–7 GPa) [347,455,456]. Nevertheless, the incorporation of large amount of free carbon (> 50 vol%) slightly reduces the Vicker's hardness of SiOC ceramics [302].

Very recently, Sorarù et al. investigated the influence of free carbon on the elastic modulus and hardness of SiOC ceramics prepared at 1200 °C using a nanoindentation technique. They found that both the elastic modulus and the hardness of SiOC ceramics

Table 2
Density (ρ), free carbon content (C_{free}), processing temperature (T), Vickers Hardness (H_v), Youngs' modulus (E), crack tip toughness (K_{I0}) and Poisson's ratio (υ) of pressureless sintered dense SiCN ceramics (n.d. = not determined).

Sample	ρ [g/cm^3]	C_{free} [wt.%]	T [°C]	H_v [GPa]	E [GPa]	K_{I0} [MPa m$^{1/2}$]	ν	Ref.
$SiC_{0.95}N_{0.85}O_{0.1}H_{0.14}$	2.3	14.42	1000	15–26	155	n.d.	n.d.	[433]
$SiCN_{0.78}O_{0.08}H$	1.85	14.10	800	8.3	82	0.56	0.245	[364,459]
$SiC_{0.98}N_{0.84}O_{0.05}H_{0.78}$	1.90	14.35	900	9.5	106	0.57	0.24	[364,459]
$SiCN_{0.80}O_{0.07}H_{0.51}$	2.00	14.42	1000	11.3	117	0.88	0.22	[364,459]
$SiC_{0.96}N_{0.80}O_{0.05}H_{0.39}$	2.10	13.52	1100	9.7	127	1.1	0.21	[364,459]
$SiC_{0.95}N_{0.77}O_{0.18}$	2.16	14.02	1200	9.6	140	0.72	0.22	[364,459]
$SiC_{0.90}N_{0.76}O_{0.14}$	2.15	12.54	1300	7.9	117	1.23	0.23	[364,459]
$SiC_{4.47}N_{1.03}H_{0.58}O_{0.06}$	1.96	52.52	1100	8.5	92	n.d.	n.d.	[463]
$SiC_{1.20}N_{1.29}H_{0.02}$ $O_{0.04}$	2.49	23.31	1100	10.8	116	n.d.	n.d.	[463]
$SiC_{0.67}N_{0.80}$	2.32	6.86	1100	13	121	n.d.	n.d.	[458]

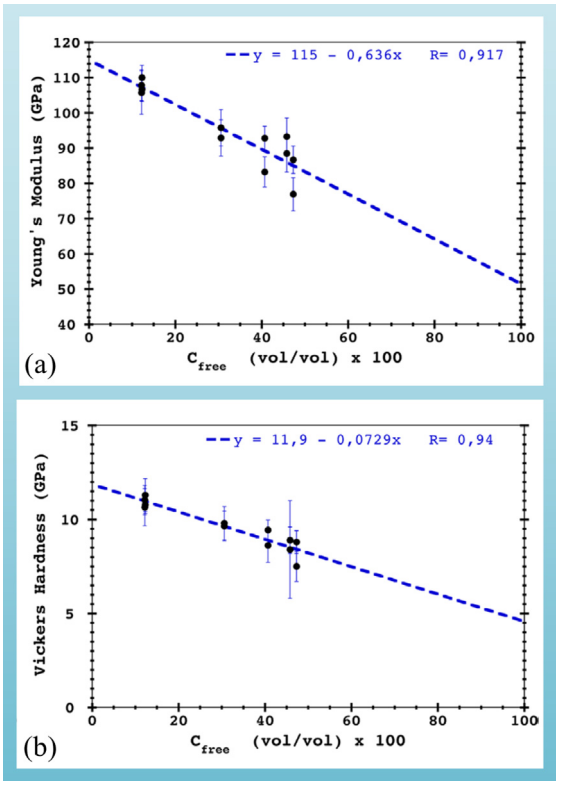

Fig. 22. Plots of the Young's modulus *(a)* and Vickers hardness *(b)* of SiOC ceramics as a function of the volume fraction of free carbon (C_{free}) (reprinted with permission of Wiley) [453].

decrease with increase in the free carbon content, and the relationship follows a simple rule of mixtures model (see Fig. 22) [453]. The experimental values are summarized in Table 1. It shows that the elastic modulus of the SiOC with the highest free carbon content is 20–30% lower than that of the analogy with the lowest free carbon content. Regarding the fracture toughness and the Poisson's ratio, however, the role of free carbon has never been systematically investigated.

Concerning the high-temperature creep resistance, the SiOC ceramics are characterized to exhibit steady-state creep behavior, and the viscosities (η) are around 2 orders of magnitude higher than the recorded values for the vitreous silica (Fig. 23) due to the enhanced connectivity of the SiOC glass network upon the partial exchanging of bivalent oxygen by tetravalent carbon [206–208,454,457]. In addition, the crystallization process of the SiOC ceramics at temperatures > 1150 °C can induce a dynamic increase in the η values (see the red arrows in Fig. 23). The η values herein were calculated from steady-state-creep rates ($\dot{\varepsilon}$) according to the following equation [457]:

$$\eta = \frac{\sigma}{2(1+\upsilon)\dot{\varepsilon}} \tag{6.1}$$

where σ and υ are the applied stress and the Poisson's ratio, respectively.

Recently, Ionescu et al. conducted a case study regarding the influence of carbidic carbon and segregated carbon on the creep behavior of SiOC ceramics [207]. They found that, as compared to vitreous silica, the presence of carbidic carbon in the single-phase amorphous SiOC glass induces a significant increase in the viscosity and glass transition temperature (T_g) but a strong decrease in the activation energy for creep (E_a) (Fig. 24). The phase-separated SiOC ceramics (*i.e.*, the phase-separated sample SG1 in Fig. 24) are analyzed to exhibit significantly lower T_g values but larger E_a values than those of their single-phase counterparts. Comparing the phase-separated SG1, SG2 and MK samples with different segregated carbon content (Fig. 24), one can see that the creep resistance of the phase-separated SiOC ceramics can be remarkably enhanced upon incorporation of segregated carbon. Interestingly, a small content of segregated carbon (≈5.8 vol%) is sufficient to provide the phase-separated SiOC ceramics with similar T_g and E_a values as compared to single-phase SiOC glasses [207]. Therefore, if the SiOC materials will be used at high temperatures at which the phase separation process is prone to occur, the compositions having free carbon are mandatory to provide an improved creep resistance.

Interestingly, the presence of high fraction of segregated carbon is also the reason for the viscoelastic behavior of amorphous SiOC glass at high temperatures, which is unexpected in amorphous materials [179,209]. As shown in Fig. 25, the creep strain in SiOC glass at 1050 °C is partially and time-dependently recoverable when the sample is unloaded. A schematic model with the SiO_2 nanodomains encapsulated in graphene cages (Model 1 in Fig. 7) was proposed to explain this behavior [209]. When a compressive stress is applied, the graphene cages will be deformed together with the embedded silica phase. When releasing the load, the graphene cages

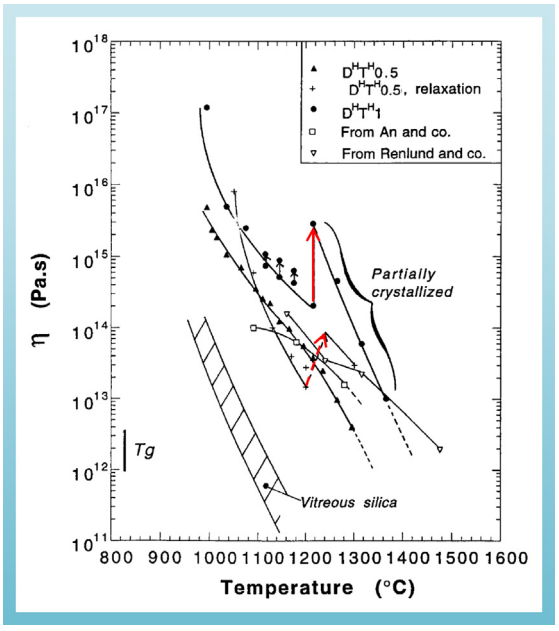

Fig. 23. Temperature dependence of the viscosity (η) of SiOC glasses (the red arrows indicate ranges where dynamic crystallization occurs to form β-SiC and, to a lesser extent, β-SiO_2 precipitates) (reprinted with permission of Wiley) [457].

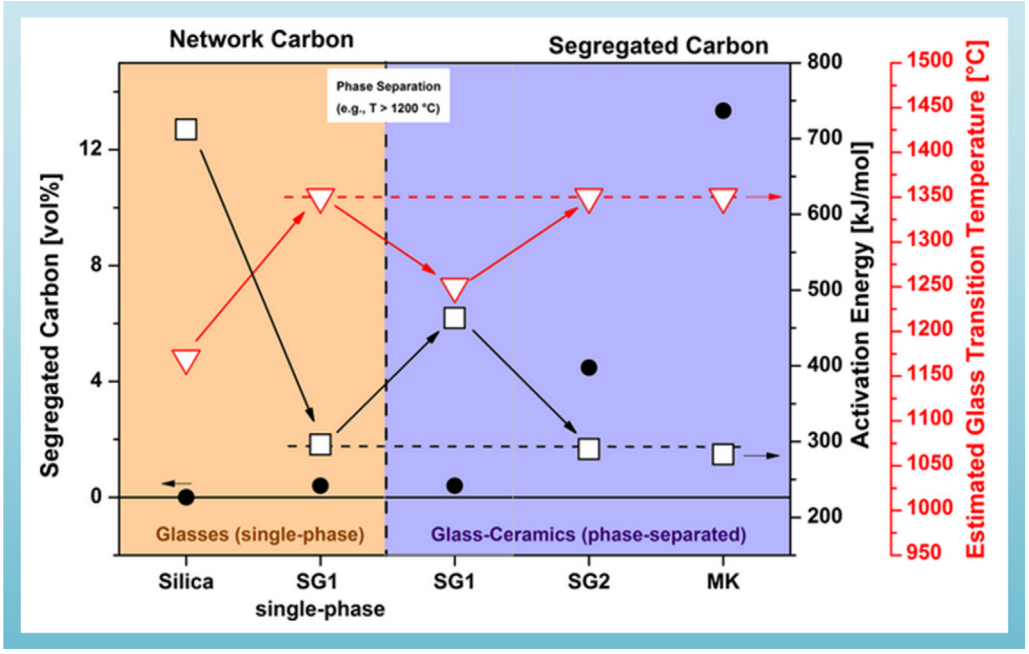

Fig. 24. The activation energy (black squares) for creep and the glass transition temperature (T_g, red triangles) as a function of the volume fraction of segregated carbon (filled circles) in SiOC materials (reprinted with permission of Wiley). The vitreous silica besides the single-phase SG1 sample is used as bench mark material for comparison, in which there is no carbidic and free carbon [207].

can gradually recover to their original shape dragging the entrapped SiO_2 glass phase along, resulting in no permanent creep deformation [179,209].

It is not very easy to investigate the mechanical properties of the SiCN-based ceramics due to the limitations in the fabrication of suitable bulk test specimens, particularly systematically study the role of free carbon. However, as a consequence of the common feature, the mechanical properties of amorphous SiCN ceramics resemble the vitreous SiO_2 glass more than polycrystalline SiC or Si_3N_4. Because of the stronger Si—C and Si—N covalent bonds, SiCN is harder and stiffer than SiO_2 glass [458]. Recently, Shah et al. prepared a fully dense SiCN monoliths using a novel pressure casting process and studied their mechanical properties using different

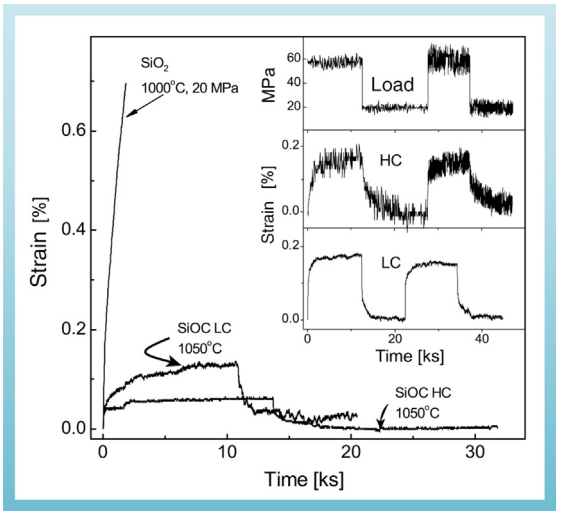

Fig. 25. The comparison between the creep response of vitreous silica (SiO_2) and the viscoelastic response of SiOC glass with low (SiOC LC) and high (SiOC HC) free carbon content. The amorphous SiOC glass does not exhibit large steady state permanent creep, as does SiO_2; instead the SiOC glass shows viscoelastic strain, which is recovered upon unloading (reprinted with permission of Elsevier) [209].

methods (Table 2). In their studies, the fracture strength of the SiCN monoliths was measured up to 1.1 GPa, Young's modulus is 155 ± 10 GPa, and the Vickers hardness increases from 15 GPa at an applied load of 1 N to 26 GPa at 3 N. Interestingly, the hardness to modulus ratio of these SiCN materials is two to three times higher than that of the crystalline Si_3N_4 or SiC. One possible explanation for this phenomenon is that the free carbon supports most of the load in elastic deformation, but the Si-C-N matrix supports the load in the indentation experiments [433].

Janakiraman et al. prepared a fully dense SiCN monolith using a liquid poly(ureamethylvinyl)-silazane precursor and systematically characterized its mechanical properties (Table 2) [364,459]. They found that the increase in the mechanical properties of the amorphous SiCN materials (*i.e.*, $SiCN_{0.78}O_{0.08}H$, $SiC_{0.98}N_{0.84}O_{0.05}H_{0.78}$, $SiCN_{0.80}O_{0.07}H_{0.51}$ and $SiC_{0.96}N_{0.80}O_{0.05}H_{0.39}$) results from the improved network connectivity realized from the stripping of hydrogen, whereas the mechanical properties of the phase-separated SiCN ceramics heat-treated at temperatures higher than 1000 °C (*i.e.*, $SiC_{0.95}N_{0.77}O_{0.18}$ and $SiC_{0.90}N_{0.76}O_{0.14}$) are primarily determined by the nanostructures [364,459–462]. The crack tip toughness (K_{I0}) of the SiCN ceramics is also characterized using a novel crack opening displacement (COD) approach. The measured K_{I0} values range from 0.6 to 1.2 MPa $m^{1/2}$ depending upon the microstructure of the materials varying from amorphous to phase-separated states. The segregated carbon within the phase-separated SiCN materials provides low energy fracture paths which control the micromechanics of crack propagation [459]. Moreover, in the nanoindentation reverse analyses, the phase-separated SiCN materials display relatively lower strain hardening exponent values compared to the amorphous counterparts due to the emergence of shear deformation promoted by the segregated carbon phase [462]. Klausmann et al. prepared two SiCN coatings with different segregated carbon content using two polysilylcarbodiimides with distinct molecular structures. They reported that the high-carbon-content SiCN coatings exhibit lower hardness (5.4–7.5 GPa, depending on the synthesis temperature) and elastic modulus (56–92 GPa) as compared to the lower carbon-content SiCN coatings with hardness of 9.8–11 GPa and elastic modulus of 105–112.5 GPa [463]. Accordingly, the free carbon generally reduces the elastic modulus and hardness of the phase-separated SiCN ceramics due to their lower density and deformation resistance as well as a weakening effect in disrupting the continuous Si−C−N tetrahedral network. This is similar to the case of SiOC materials as shown in Fig. 23. However, comparing the mechanical properties list in Table 2 and the corresponding microstructure, it can be seen that this effect becomes significant only when the size and amount of the free-carbon nanodomains reach a critical level where their plastic deformation is promoted [364,433,458,461].

The high-temperature creep behavior of amorphous SiCN ceramics have also been studied by An and co-workers [464]. Three creep stages have been determined during the creep experiments conducted at 1090–1280 °C. In stage I, the strain rate decreases rapidly with time, and the deformation is accompanied by densification of the materials due to the elimination of open and closed porosity. In stage II, the samples exhibit a steady-state creep rate, and the density remains essentially constant until the end of the deformation test. In stage III, the creep rate gradually declines to values that are below the sensitivity of the apparatus, showing a creep-hardening behavior. The shear viscosity of the amorphous SiCN ceramics in stage II is nearly Newtonian, and it is measured to be approximately 10^3 times higher than that of fused silica (Fig. 26) [464]. Moreover, the viscosity of the amorphous SiCN-based ceramics can be further improved with the addition of boron. For instance, Riedel et al. reported that the viscosity of an amorphous $Si_2B_{1.0}C_{3.4}N_{2.3}$ ceramic in stage II is six orders of magnitude higher than that of fused silica at 1550 °C [465]. In addition, Wan et al. studied the creep behavior of a Si_3N_4/SiC nano-nano composite produced by pyrolysis of a commercial polyureasilazane at 1450 °C and subsequent sintering at 1600 °C. They found that the Si_3N_4/SiC monoliths without sintering aids exhibit the best high-temperature creep resistance among the counterparts due to the limited formation of intergranular glassy phases that are effective as fast route for mass transfer [466]. Nevertheless, the effects of free carbon on the high-temperature creep behavior and the associate

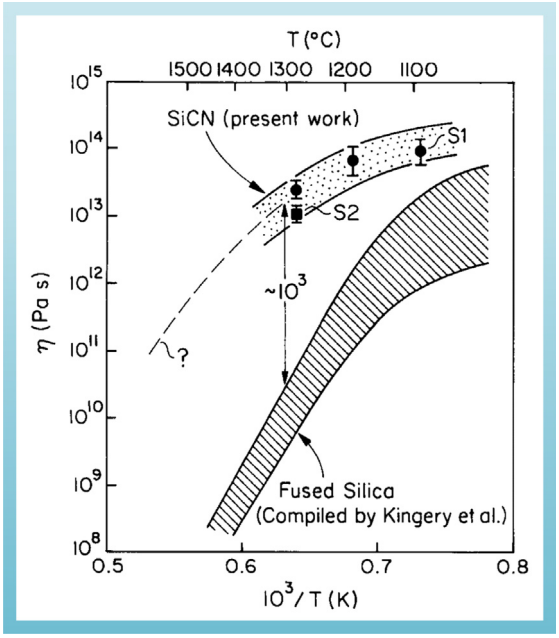

Fig. 26. The shear viscosity of two SiCN ceramics composed of $Si_{1.7}C_{1.0\pm0.1}N_{1.5}$ (S1 is pyrolyzed at 1000 °C, and S2 is further heat-treated in nitrogen for 10 h at 1300 °C) and the data envelope for the viscosity of fused silica (reprinted with permission of Wiley) [464].

mechanisms of the SiCN ceramics have been rarely discussed, which are open questions for future studies.

6.2. Thermal properties

The thermal properties of PDCs are also important for their high-temperature applications, such as the thermal conductivity (K) representing the heat transfer ability of the materials [467–469], the coefficient of thermal expansion (CTE) describing how the size of an object changes with a temperature variation [441,470], the specific heat capacity (C_p) which is a measure of how much heat is needed to raise the temperature of one kilogram of a materials by 1 Kelvin [313], the thermal diffusivity (α) characterizing the rate of transfer of heat of a material from the hot end to the cold end [313] as well as the thermal shock resistance (TSR) indicating the capability to withstand sudden changes in temperature either during heating or cooling [471]. In recent years, some important progress has been made in the study of the thermal properties of PDCs despite the research regarding the SiCN-based ceramics is still scarce (Table 3).

The thermal conductivity is the most studied thermal property of PDCs. Generally, amorphous PDCs show poor thermal conductivity due to the low mass fractal dimension of the glassy matrix, residual hydrogen and the existence of dangling bonds [116,469,472–474]. As listed in Table 3, amorphous SiOC glass exhibits quite low intrinsic thermal conductivity (≈1.2 W/(m K) at room temperature), which is even lower than that of fused silica (≈1.4 W/(m K)) [313,319,475,476]. Moreover, the K values of macro-porous SiOC ceramics can be further reduced to 0.041 W/(m K), suggesting that amorphous SiOC ceramics hold great promise as a thermal insulation material for application at high temperatures [473]. Gurlo et al. studied the temperature dependence of amorphous SiOC glass together with fused silica, amorphous carbon and cross-planed graphite (Fig. 27). Two amorphous SiOC glasses ($SiO_{1.59}C_{0.66}$ and $SiO_{1.54}C_{0.53}$) were synthesized in the same way up to 1100 °C, but the $SiO_{1.59}C_{0.66}$ glass was subsequently hot-pressed in argon at 1600 °C. The results show that the thermal conductivities of both SiOC glasses are almost independent of temperature from 200 to 1000 °C. The $SiO_{1.54}C_{0.53}$ sample obtained at 1100 °C (≈ 0.5 W/(m K)) possesses the lowest thermal conductivity, which might be due to the large open porosity (12 vol%) [475].

The phase separation of SiOC materials can significantly enhance the K values because of the precipitation of SiC and segregated carbon phase with relatively higher thermal conductivities [476]. The K values of dense crystallized SiC have been measured to be higher than 200 W/(m K) [477], and the lowest thermal conductivity reported for any form of amorphous SiC is around 4 W/(m K) [478], which is still substantially higher than that of all amorphous SiOC glasses (Table 3) or fused silica. The thermal conductivity of carbon varies from 2.2 W/(m•K) for amorphous carbon [479] to 600 W/(m K) for graphite (in a crystallographic direction) [476]. Therefore, the effects of both SiC and segregated carbon within the phase-separated SiOC ceramics should be considered, especially when they form a percolating network [475]. Very recently, Stabler et al. investigated the influence of phase separation as well as chemical and phase compositions on the thermal conductivity of SiOC materials [6]. It was found that, after phase separation, the thermal conductivities (K) of the SiOC materials with similar chemical composition and porosity have been enhanced from 1.18 (at 100 °C) and 1.60 (at 1300 °C) W/(m K) to 1.42 (at 100 °C) and 1.77 (at 1300 °C) W/(m•K), respectively (Table 3). With increasing free carbon content (from 0.11 wt% to 12.67 wt%), the K values of the phase-separated SiOC ceramics grow from 1.42 (at 100 °C) and

Table 3
Reported open porosity (ζ), free carbon content (C_{free}), processing temperature and pressure (T, P), thermal conductivity (K), coefficient of thermal expansion (CTE) as well as specific heat capacity (C_p) of PDCs. Herein, RT, PL, LT and HT represent room temperature, pressureless, low temperature (100–1000 °C) and high temperature (around 1100–1300 °C), respectively (n.d. = not determined).

Samples	ζ [vol.%]	C_{free} [wt.%]	T, P [°C], [MPa]	K [W/(m K)]	CTE [10^{-6} K^{-1}]	C_p [J/g K]	Ref.
$SiO_{1.38}C_{0.32}$	0.3	0.27	1100, PL	1.18 at 100 °C 1.60 at 1300 °C	3.23 (LT)	0.79 at 50 °C 1.18 at 1000 °C	[313]
$SiO_{1.41}C_{0.30}$	0	0.11	1600, 50	1.42 at 100 °C 1.77 at 1300 °C	1.84 (LT) 4.41 (HT)	0.79 at 50 °C 1.11 at 1000 °C	[313]
$SiO_{1.50}C_{0.71}$	0	9.12	1600, 50	1.50 at 100 °C 1.92 at 1300 °C	2.02 (LT) 4.87 (HT)	0.78 at 50 °C 1.22 at 1000 °C	[313]
$SiO_{1.27}C_{0.97}$	0	12.07	1600, 50	1.46 at 100 °C 2.06 at 1300 °C	3.09 (LT) 5.29 (HT)	0.70 at 50 °C 1.24 at 1000 °C	[313]
$SiO_{0.94}C_{1.13}$	1.6	12.67	1600, 50	2.15 at 100 °C 2.72 at 1300 °C	3.23 (LT)	0.73 at 50 °C 1.22 at1000 °C	[313]
$SiC_{0.40}O_{1.77}$	30	5.68	1300, 10	1.37 at RT	n.d.	n.d.	[319]
$SiC_{0.42}O_{1.72}$	10	5.55	1300, 80	1.38 at RT	n.d.	n.d.	[319]
$SiC_{0.46}O_{1.84}$	1	7.24	1500, 10	1.38 at RT	n.d.	n.d.	[319]
$SiC_{0.40}O_{1.61}$	8	4.11	1500, 80	1.37 at RT	n.d.	n.d.	[319]
$SiC_{1.10}O_{1.51}$	0	15.70	1450, 40	1.3 at RT	n.d.	n.d.	[472]
$SiC_{1.10}O_{1.48}$	0	15.54	1550, 40	1.6 at RT	n.d.	n.d.	[472]
$SiC_{1.11}O_{1.52}$	0	15.90	1650, 40	1.8 at RT	n.d.	n.d.	[472]
$SiO_{1.54}C_{0.53}$	12	6.10	1100, PL	0.5 at RT	n.d.	n.d.	[475]
$SiO_{1.59}C_{0.66}$	0	8.90	1600, 30	1.3 at RT	n.d.	n.d.	[475]
$SiO_{1.65}C_{0.42}$	0	4.95	1600, PL	1.3 at RT	n.d.	n.d.	[475]
$SiC_{0.60}O_{1.53}$	n.d.	7.4	1650, 41	n.d.	3.14 (average)	n.d.	[441]
SiC	3.0	n.d.	900, PL	2.4	n.d.	n.d.	[480]
SiC	4.1	n.d.	1150, PL	3.8	n.d.	n.d.	[480]
SiC	9.7	n.d.	1400, PL	12	n.d.	n.d.	[480]
SiC fiber (Tyranno SA)	n.d.	2.37	> 1700, PL	64.6 at RT	4.5 (LT)	1.4 at RT	[482]
$SiC_{1.6}N_{1.3}$	9.6	28.90	1400, PL	n.d.	3.08 (100 °C) 3.96 (1200 °C)	n.d.	[470]

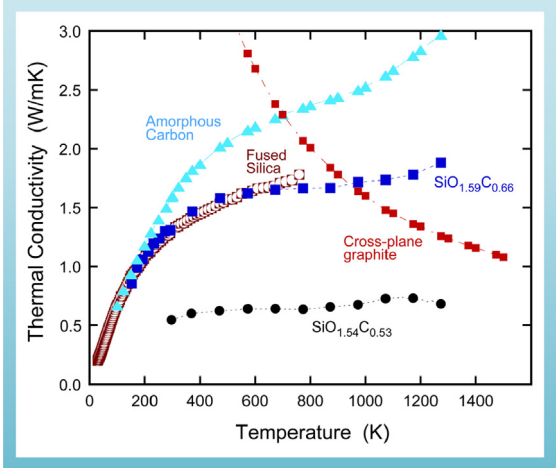

Fig. 27. The thermal conductivities of two amorphous SiOC glasses ($SiO_{1.59}C_{0.66}$ and $SiO_{1.54}C_{0.53}$), fused silica, cross-plane graphite and amorphous carbon (reprinted with permission of Wiley) [475].

1.77 (at 1300 °C) W/(m•K) to 2.15 (at 100 °C) and 2.72 (at 1300 °C) W/(m K), respectively. Interestingly, the $SiO_{0.94}C_{1.13}$ sample exhibits a much higher K value than that of the $SiO_{1.27}C_{0.97}$ sample at both low and high temperatures despite they have comparable free carbon content (12.07 wt% vs. 12.67 wt%), which is considered to rely on the different content of SiC nanoparticles (Table 3) [6]. A similar trend has been characterized in the spark plasma sintered SiOC monoliths reported by Mazo et al. [476].

The effects of free carbon on the thermal conductivity of SiC-based materials derived from polycarbosilanes are to some extent different from that of the Si-O-C system. The researchers found that reducing the segregated carbon present in the amorphous SiC matrix or at the SiC grain boundaries will lead to an increase of the thermal conductivity of the polymer-derived SiC ceramics (the free carbon is regarded as "impurity" here) [480,481]. One good example is the well-crystalized SiC fiber (*e.g.*, Tyranno SA) which has low free carbon content but shows thermal conductivity higher than 60 W/(m K) (see Table 3) [482]. This observation is attributed to two factors: First, the thermal conductivity of the crystallized SiC matrix is higher than that of the segregated carbon

[319,476,480]. Second, the free carbon can suppress the grain growth of the SiC nanoparticles (see Section 5.3.1) and therefore hinder the increase of overall thermal conductivity.

Surprisingly, the intrinsic thermal conductivities of SiCN materials in both single-phase and phase-separated status have not been investigated yet. This might be due to the limitations in the fabrication of suitable bulk testing specimens. From some literatures, we know that the thermal conductivity of amorphous SiCN glass is also rather low, resembling the amorphous SiOC glass and fused silica [469,474]. However, the role of free carbon in the thermal conductivity of the Si-C-N system has not been reported yet.

The coefficient of thermal expansion (CTE) of PDCs has been reported in some literatures (Table 3). Most of the CTE values of "pure" PDCs are measured to be around $3 \times 10^{-6}\ K^{-1}$, which are nearly one order of magnitude higher than that of vitreous silica ($0.57 \times 10^{-6}\ K^{-1}$), but the values are still very low. Stabler et al. found that, different from the thermal conductivity discussed above, the phase separation of SiOC materials leads to a decrease in their CTE values (see $SiO_{1.38}C_{0.32}$ and $SiO_{1.41}C_{0.30}$ in Table 3). The CTE values of the phase-separated SiOC ceramics enhance with increasing segregated carbon content (see $SiO_{1.41}C_{0.30}$, $SiO_{1.50}C_{0.71}$, $SiO_{1.27}C_{0.97}$, $SiO_{0.94}C_{1.13}$ in Table 3), which is in agreement with the larger CTE values of pyrolytic carbon ($4–6 \times 10^{-6}\ K^{-1}$) [483] and β-SiC ($4.3–4.9 \times 10^{-6}\ K^{-1}$) [484], respectively. As a result, the CTE of the phase-separated SiOC ceramics can be adjusted to the value of the single-phase SiOC glass (*e.g.*, the CTE values of the $SiO_{1.38}C_{0.32}$ and $SiO_{0.94}C_{1.13}$ samples are $3.23 \times 10^{-6}\ K^{-1}$ at room temperature). This behavior proves the possibility of tailoring the CTE of SiOC materials by adjusting the free carbon content. Moreover, the CTE of SiOC-based ceramics can be further enhanced via the incorporation of additional phases, either by the pyrolysis of metal-containing single-source precursors yielding Si(M)OC ceramic nanocomposites (*e.g.*, Si−Al−O−C ceramics) [93], or by the use of highly conductive fillers (*e.g.*, $MoSi_2$) [471,485]. Conversely, the CTE can also be reduced by similar means [486,487]. For example, very recently, Fedorova et al. prepared a β-eucryptite-containing SiOC material whose CTE values can be adjusted from slightly positive to moderate negative upon tuning the phase composition and changing the unit cell parameters of the β-eucryptite phase [487]. As shown in Table 3, the CTE values of both SiOC and SiCN materials at higher temperatures (1100–1300 °C) are larger than that at lower temperatures. Therefore, increasing CTE values of PDCs have to be considered when anticipating applications at temperatures beyond 1000 °C [313].

The specific heat capacity (C_p), thermal diffusivity (α) and thermal shock resistance of PDCs have been occasionally reported in some literatures [313,471,488]. Stabler et al. found that the temperature dependence of the C_p values of the SiOC samples with low carbidic carbon content resembles that of vitreous silica, whereas that of the samples with a higher carbidic carbon content resembles that of β-SiC [313]. The thermal shock resistance of PDC materials can be improved by either foam formation [488], fiber-reinforcement [489], or by filler addition [471,490]. Nevertheless, the role of free carbon on these properties have been rarely reported.

6.3. Oxidation resistance

Excellent oxidation resistance up to exceptionally high temperatures (1500–1600 °C) is one of the most important features of PDCs [51,65,323,444,491–497]. Due to the formation a dense and continuous oxide layer (mainly SiO_2), the Si-based PDCs exhibit a parabolic oxidation behavior (so called passive oxidation) with the parabolic rate constants and activation energies similar to that of pure SiC and Si_3N_4 ceramics [51,444,496–498]. The oxidation behavior of PDCs including the Si−C, Si−O−C, Si−C−N, Si−B−C−N, Si−Al−C−N systems has been extensively studied [51,52,54,79,80,315,444,492,496,499]. A summary of this subject can be found in Ref. [500].

Burns et al. investigated the effect of free carbon on the oxidative stability of amorphous SiCN ceramic powders at 1200 °C in air. The results show that the influence of free carbon content on the oxidative stability of an amorphous SiCN ceramics is in accordance with a percolation theory, and the percolation threshold of the free carbon can be affected by the specific surface area of the ceramics. The microstructure of amorphous SiCN ceramics can be described as SiCN and free carbon nanodomains randomly dispersed in space [337,354]. When the amount of segregated carbon is relatively low, the SiCN is therefore a continuous phase. During the oxidation process, a dense and continuous SiO_2 scale formed on the surface of the SiCN phase can protect further oxidation of both the free carbon and the SiCN phases. In this case, the free carbon has little to no bad influence on the oxidation resistance of the SiCN ceramics. As the weight percent of free carbon increases, it becomes a continuous phase at the percolation threshold. Under this condition, oxygen can "percolate" through the SiCN matrix, leading to a catastrophic loss of oxidation resistance. In this study, the percolation threshold of free carbon in the unground SiCN ceramics is around 35–40 wt%, while it shifts to about 15–20 wt% after being ground into 40–60 μm fine powders with increased specific surface area [170].

Bahloul et al. found that the effects of free carbon on the oxidation resistance of SiCN-based ceramics depend on the initial conditions of pyrolysis because the structural evolution and the distribution of free carbon are affected by the temperature and duration of the heat treatment [501,502]. For the amorphous SiCN ceramics pyrolyzed at lower temperatures (≤1200 °C), the free carbon is embedded in the continuous SiCN phase. Accordingly, the free carbon can be protected by the dense and continuous silica scale formed on the surface of SiCN phase. The oxidation of the SiCN phase facilitated by the combustion of free carbon via creating micropores/cracks, is also suppressed. For the crystallized SiCN ceramics obtained at elevated temperatures (≥1400 °C), the size/length of free carbon increases, and they may form a continuous network within the SiCN matrix (the percolation threshold decreases when the aspect ratio of the dispersive phase increases). In this case, the free carbon will be oxidized first and then facilitate the oxidation of the rest of SiCN-based ceramics [501,502]. Moreover, in the following up studies, Bahloul et al. found that, compared to the influence of content, the reorganization of free carbon during the high-temperature treatment affects more strongly on the oxidation resistance of the SiCN based ceramics [503].

Wen et al. investigated the isothermal oxidation behavior of dese monolithic (Hf,Ti)C/SiC- and (Hf,Ta)C/SiC-based ceramic

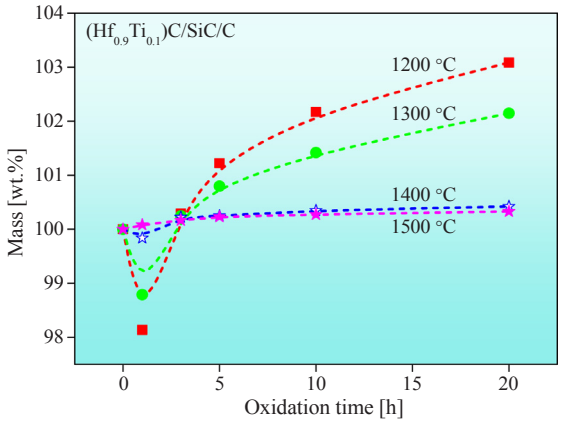

Fig. 28. Isothermal oxidation curves of $(Hf_{0.9}Ti_{0.1})C/SiC$ dense monoliths at temperatures from 1200 to 1500 °C. The mass loss in the first 3 h is due to the oxidation of free carbon (reprinted with permission of Wiley) [504].

nanocomposites derived from chemically modified allylhydridopolycarbosilane at 1200–1500 °C in air. The nanocomposites contain around 5–7 vol% of free carbon. Because the onset temperature for oxidation of the free carbon is lower than that of the other phases, the oxidation curves are characterized by a mass loss at the beginning followed by a parabolic mass gain in the end (Fig. 28) [310,495]. Actually, this phenomenon appears widely in crystallized PDCs in both, isothermal or non-isothermal, oxidation experiments [310,495,501,502]. Interestingly, as shown in Fig. 28, the effect of free carbon on the mass loss at lower temperatures is more obviously than that at higher temperatures. At 1500 °C, almost no mass loss can be characterized. This can be explained that at higher temperatures, the formation rate of dense oxide scale is much faster than that at lower temperatures, which protects the free carbon immediately from oxidation [495,504].

Brewer et al. studied the oxidation behavior of SiOC powders with different free carbon content at 600–1200 °C for 500 h [505]. They found that the samples with larger amount of free carbon completely convert into SiO_2 at 600 and 800 °C, whereas the samples with lower free carbon content show better oxidation resistance, owing to the large amount of free carbon forming a continuous network within the SiOC ceramics. The combustion of the free carbon networks will lead to a lot of micropores and cracks for oxygen transportation into the SiOC matrix. In addition, at 1000 and 1200 °C the samples exhibit better oxidation resistance than those at 600 and 800 °C. This is because, at higher temperatures, the faster formed passivating silica scale prevents the samples from further oxidation [505]. This behavior has also been analyzed in oxidation of dense monolithic (Hf,Ti)C/SiC- and (Hf,Ta)C/SiC-based ceramic nanocomposites as mentioned above (see Fig. 28) [495,504]. Moreover, Modena et al. studied the oxidation kinetics of polymer-derived amorphous SiOC ceramics containing different amounts of free carbon at 1350 °C in air. They found that the parabolic $\alpha \cdot K_{xp}$ constants increase with increasing of free carbon content in the SiOC nanostructure. This result suggests that the free carbon activity in SiOC glass is likely less than unity, which explains the passive oxidation behavior of SiCO in nature [444].

6.4. Corrosion resistance

The corrosion resistance of PDCs is also one of the most important parameters for its structural and functional applications in harsh environments. Up to now, the corrosion resistance of PDCs has been investigated in various aggressive media, such as alkaline solutions [506,507], hydrofluoric solutions [508,509], hot sulfuric acid solutions [75], water vapor [52,510], hydrothermal conditions [60,511], sodium salts [509,510], and ultrahigh-temperature ablation [61,489]. Moreover, in order to prepare porous ceramics foams with high specific surface area and carbide derived carbon materials, the corrosion resistance of the PDCs is also an interesting research topic [204,334,335]. As a consequence of the common feature, the corrosion resistance of the PDCs is mainly related to their chemical/phase compositions and microstructures, including the amount and network structure of free carbon phase [184,512].

Soraru et al. measured the corrosion resistance of SiOC glasses in both alkaline and hydrofluoric solutions. The test data reveal that SiOC glasses are more durable than fused silica and soda-lime glass due to the presence of Si—C bonds. This is because, compared to the strongly polarized Si—O—Si bonds, the Si—C bonds is more resistant to a nucleophilic attack by OH^- or F^- ions [184]. The role of the segregated carbon phase is twofold. On the one hand, the free carbon provides an intergranular phase between the silica nanodomains which are surrounded by SiO_xC_y phase with mixed bonds [338]. This microstructure limits the degradation of the SiO_xC_y phase to form the more-soluble SiO_2 and prevents the formation of a continuous SiO_2 network. On the other hand, the free carbon is insoluble in both alkaline and hydrofluoric solutions. Consequently, it will act as a chemical and physical barrier to hinder the attack or diffusion of OH^- or F^- ions at and within the surface of the SiOC ceramics. Moreover, because of the dissolution of silica species, the free carbon phase accumulates progressively on the surface, and thereby provides further physical barrier between the SiOC ceramics and the aggressive solutions [184]. Linck et al. studied the corrosion behavior of SiOC-based ceramic nanocomposites under hydrothermal conditions at moderate temperatures (150–250 °C). The results show that the ternary SiOC ceramics exhibit a remarkably higher hydrothermal corrosion resistance (up to 5 orders of magnitude) than that of SiC. The excellent corrosion resistance might be

attributed to the high amount of segregated carbon (ca. 37 mol.%) which cannot be corroded by the hot aqueous media [511].

The researches mentioned above are mainly regarding the SiOC-based ceramics because the study concerning the role of free carbon on the corrosion resistance of PDCs is rarely reported. The positive effects of the free carbon might be also suitable for other PDCs such as SiC- and SiCN-based ceramics due to the similar morphology of the free carbon in these ceramics [18,82]. Accordingly, more systematic researches on this topic are needed in the future.

6.5. Tribological properties

In recent years, the study of tribological properties (incl. friction, lubrication and wear) of PDCs has been of enormous practical importance because multiple industrial applications of the PDCs such as brake valves, micro-electro-mechanical systems (MEMS) and other similar motion-controlled mechanisms require good wear properties and appropriate friction coefficients [82,105,205,513]. The researches regarding the tribology of PDCs and their composites have been reported since 2005 despite that the potential tribological applications of PDCs was recognized several years earlier [107,205,513–517]. Generally, the friction behavior is characterized by the coefficient of friction (COF), which is defined as the ratio of friction force F_f and the normal force F_n. The wear behavior is described by the coefficient of wear (k), which is defined for the steady-state wear as the following equation:

$$k = \frac{3HV}{F_n L} \tag{6.2}$$

where H is Brinell hardness of the softer wearing material, V the volumetric loss of the softer material after sliding for a distance L, and F_n the normal load [106,518].

One motivation for the fundamental investigation on the tribological properties of PDCs is the presence of graphite-like free carbon within the ceramic matrix [104,205]. The graphite is a well-known solid lubricant with the COF of around 0.15–0.2, but it can be much higher (up to 0.8) when measured in vacuum or dry inert environments with less than 100 ppm of H_2O. It's well accepted that the lubricity of graphite in air is related to its lamellar and hexagonal structure, and the ease of slip of the graphite basal planes increases from intercalation of adsorbed water and oxygen [519–521]. Accordingly, the role of free carbon on the tribological behavior of PDCs under different conditions is attractive and important for their practical applications.

Klaffke et al. characterized the friction and wear behavior of the SiCN ceramics obtained at different temperatures. They found that the formation and organization of graphitic free carbon with increasing pyrolytic temperatures from 800 °C to 1100 °C strongly influence the reduction of COF (decreases from 0.45 to 0.16 in normal air at room temperature) and k because the graphite-like free carbon acts as an inbuilt solid lubricant (Fig. 29a) [106]. The mechanism is usually related to a thin graphitic "transfer layer" at the interface between the specimen and the counter body and subsequently shields the counter body from direct contact with the specimen's surface, resulting in a reduction of friction and wear coefficients [106,205]. Similar role of free carbon has been analyzed in the polymer-derived SiCN sub-millimetre thick miniaturized components, SiOC-$ZrSi_2$ coating and sputtered SiCN films [108,522,523].

Cross and co-workers evaluated the fundamental tribological behavior of amorphous SiCN ceramics pyrolyzed at 1000 °C using a ball-on-disk linear wear tester at various contact pressures. The bulk SiCN exhibits a low friction coefficient and good wear resistance in humid environments but shows significant fracture and gouging in dry environments at higher contact pressures [513]. In their following up work, Cross et al. found that, in dry environments, the tribological behavior of $SiC_xO_yN_z$ is divided into two regimes: one is the low-friction regime with a COF of ≈0.2 and negligible wear, and another is the high-friction regime with a COF of ≈0.7 and

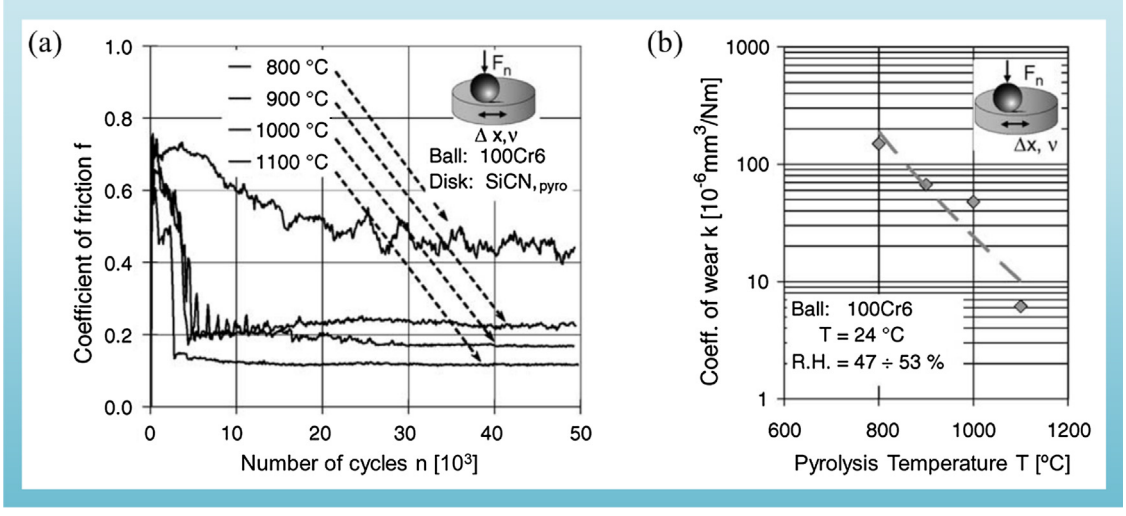

Fig. 29. Evolution of coefficient of friction *(a)* and coefficient of wear *(b)* in tests with 100Cr6 against SiCN obtained at different pyrolytic temperatures (in normal air) (reprinted with permission of Elsevier) [106].

high wear. The transition occurs at a critical value of contact stress which appears to be related to the onset of fracture of the ceramics and moves to a higher value in the ceramics with higher modulus and hardness. In a humid environment, the COF remains unchanged at around 0.2 because the critical value of contact stress moves beyond the experimentally accessible regime [104]. Accordingly, in their studies, as long as the contact stress is below a critical value, all $SiC_xO_yN_z$ ceramics display low friction in both dry and humid environments, and the effects of free carbon seem to be negligible even in the carbon-rich samples. This result is different from Klaffke's work mentioned above because their experiments appear to be performed in the high-friction regime. Consequently, a high COF value, a high rate of wear and a "transfer layer" can be characterized [104]. That means the role of free carbon on the tribological properties of PDCs might be effective only when the contact stress is beyond the critical value. However, this hypothesis should be further proven in the future. The role of free carbon combined with the influence of working environments, loading strength, materials of counter parts, sliding distance on the tribological properties of PDCs need more systematic studies.

7. Influence of the *in situ* formed carbon on functional properties of PDCs

7.1. Electrical properties

Electrical properties of the PDCs have been widely investigated since the early discovery of these new materials due to their functional applications for high-temperature microelectromechanical systems (MEMS), hash-environmental sensors, micro glow plugs as well as electrode materials for lithium-ion batteries and pacemakers [58,91,92,265,367,524–533]. The intrinsic room-temperature DC electrical conductivity of PDCs varies up to 15 orders of magnitude (typically from 10^{-10} to 10^{-8} to 1 S/cm) depending on the phase composition and the microstructure of ceramics, which are determined by the molecular structure of preceramic precursors, processing techniques and parameters of heat treatments (incl. temperature, atmosphere and holding time) [18,194]. Moreover, PDCs are reported to exhibit several unusual electrical properties compared to other traditional polycrystalline ceramics, such as high-temperature semiconducting behavior up to 1300 °C [192,534], anomalously high piezoresistivity [48,57,201,202,230] and profound doping effect [535,536]. It's well accepted that the intriguing properties are mainly related to the unique microstructure of PDCs comprised of a silicon-based ceramic matrix and an *in situ* formed free carbon as well as the distinct electrical properties of these phases [537,538].

7.1.1. Electrical conductivity

Among the phases occurring in the PDCs, most of them are insulators (*e.g.*, SiO_2 and Si_3N_4) or semiconductors (SiC, SiO_xC_y, SiC_xN_y and amorphous carbon) with the room-temperature DC electrical conductivity in the ranges of 10^{-14}–10^{-12} S/cm for insulators and 10^{-4}–10^{2} S/cm for semiconductors. Only the segregated free carbon which exists in the form of turbostratic carbon or graphitic carbon in the PDCs has a significantly higher DC electrical conductivity in the range of 1–10^5 S/cm [423]. Therefore, the concentration and/or structural evolution of the free carbon within the PDCs strongly influences their electrical conductivity [423,539].

The effects of the concentration of free carbon on the electrical conductivity of PDCs can be divided into in three regimes (see Fig. 30). For the PDCs containing sufficient free carbon to form a percolation network (*i.e.*, the concentration of free carbon is higher than a percolation threshold, Fig. 30a), the conduction of the PDCs is realized by direct transportation of charge carriers (*e.g.*, free electrons) [191,361,423]. Under this condition, the electrical conductivity can be described using a general effective media theory (GEM) [423]. Accordingly, the mean electrical conductivity (σ_m) of the PDCs can be estimated as a function of the volume fraction (Φ) of the high-conductive phase (*i.e.*, free carbon) using the following equation [540]:

$$\frac{(1-\Phi)(\sigma_l^{1/t}-\sigma_m^{1/t})}{\sigma_l^{1/t}+A\sigma_m^{1/t}}+\frac{\Phi(\sigma_h^{1/t}-\sigma_m^{1/t})}{\sigma_h^{1/t}+A\sigma_m^{1/t}}=0 \tag{7.1}$$

$$A=\frac{1-\Phi_c}{\Phi_c} \tag{7.2}$$

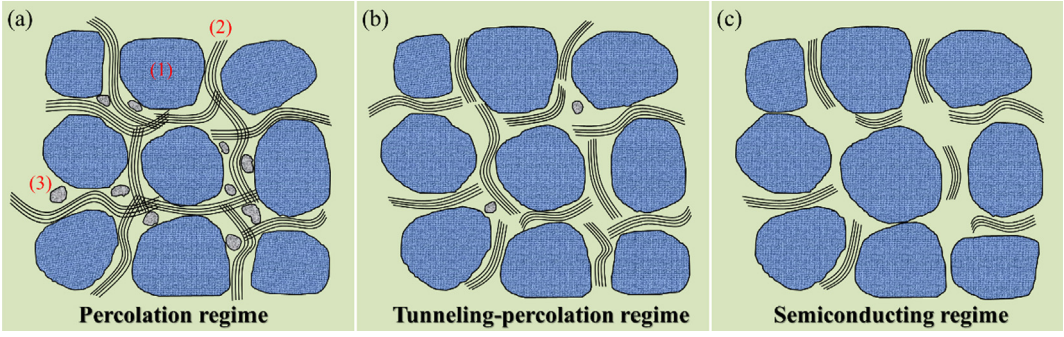

Fig. 30. Models for microstructure of PDCs in different conducting regimes. (1), (2) and (3) are SiC-based nanodomains, free carbon ribbons and α-SiC nanoparticles, respectively [685].

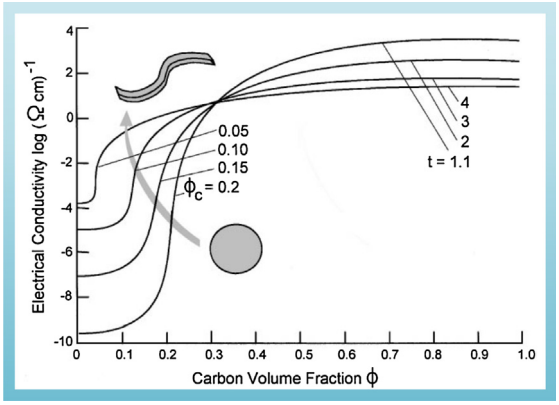

Fig. 31. Insulator-conductor percolation transitions calculated from Eqs. (7.1) and (7.2) using different values of t (from 1.1 to 4) and Φ_c (from 0.2 to 0.05) (reprinted with permission of Elsevier) [423].

where Φ_c is the percolation threshold; σ_l and σ_h are electrical conductivities of the low-conductive and high-conductive phases, respectively; A is a function of the percolation threshold Φ_c; t is a morphology parameter which is most often found to lie in the range of 1.65–2.0. For the graphite (flaky) particles in polymers, significantly higher values up to 3.1 were determined, which is related to the tunneling processes between the conducting particles [541,542]. Fig. 31 presents the mean electrical conductivity (σ_m) of a composite material (SiO_2/free carbon) as a function of the volume fraction of high conductivity phase (free carbon) according to Eqs. (7.1) and (7.2) using different values of t and Φ_c. We can see that the jump of electrical conductivity at the percolation threshold decreases with increasing elongation of the free carbon (leading to increasing t and decreasing Φ_c), and the electrical conductivity below the threshold appears to be dramatically higher than that of the systems containing regular particle morphology [423].

Basically, percolation threshold (Φ_c) of a composite material strongly depends on the particle size and shape (aspect ratio) of the conductive inclusions, and it typically varies between 1 and 60 vol% [543]. For instance, the percolation threshold has been predicted to be less than 5 vol% when the aspect ratio of the conductive component exceeds 100 [423,544]. For spherical particles with a size below 50 nm the percolation threshold will be lower than 10 vol% [368,545]. As we known from TEM images (Figs. 12 and 13) that the free carbon possesses a ribbon-like shape which has a relatively high aspect ratio. Thus, the percolation threshold of free carbon is not very high. For instance, it is measured to be 11.3 vol% for a polycarbosilane derived SiC fiber [546]. When the free carbon content is not high enough to form a percolation network, the electrical conductivity of PDCs can be subdivided into two regimes, namely, tunneling-percolation regime and semiconducting regime, with different conduction mechanisms [375]. For the tunneling-percolation regime, the free-carbon content is just higher than a threshold for tunneling process between the neighboring free carbon clusters. That means the distance between two neighboring free carbon ribbons is quite small for tunneling effect despite that they are not interconnected (Fig. 30b). In this regime, the conduction of PDCs is admitted by tunneling-percolation mechanism, and a high piezoresistivity of the PDCs can be characterized if a mechanical stress is added (will be discussed later) [202].

If the concentration of free carbon is even lower than the tunneling-percolation threshold, the conduction of the PDCs will be dominated by the amorphous semiconducting behavior (*i.e.*, semiconducting regime). The schematically models for this regime is illustrated in Fig. 30c. As amorphous semiconductors, the temperature dependence of the DC electrical conductivity (σ_{dc}) can be described as follows: under the condition of $kT \ll E_{gap}$ (k is the Boltzmann constant, T is the temperature and E_{gap} is energy gap between Fermi level and conducting band), the σ_{dc} obeys the Mott's law:

$$\sigma_{dc}(T) = \sigma_0 exp\left[-\left(\frac{T_0}{T}\right)^{\frac{1}{4}}\right] \tag{7.3}$$

The variable-range hopping (VRH) mechanism is supposed to be the explanation for this semiconducting behavior at low temperature. Many studies suggest that the amorphous semiconducting behavior of the PDCs at low temperature is also dominated by the VRH mechanism [191,423,537,538,547]. In the case $kT \gg E_{gap}$, the σ_{dc} shows an Arrhenius behavior as follows:

$$\sigma_{dc}(T) = \sigma_0 exp\left[-\left(\frac{\Delta E}{kT}\right)\right] \tag{7.4}$$

where ΔE is the activation energy (*i.e.*, energy gap between Fermi level and conducting band). This equation is associated with tunneling of charge carriers between excited states as well as excitation into the conduction band. Amorphous PDCs pyrolyzed at temperatures lower than around 1200 °C were found to behave as electron semiconductors following equation (7.3) over a wide range of temperatures [191,423,536,548]. Polycrystalline PDCs annealed at temperatures higher than about 1200 °C behave according to equation (7.4) at high temperatures [191,548]. The change in the temperature dependence of conductivity in PDC samples reveals a decrease of the energy gap (E_{gap}) with increasing pyrolysis temperature due to the nucleation and graphitization of the free carbon [191].

Recently, Wang et al. found that the conduction of amorphous SiOCN ceramics is admitted by three conduction mechanisms in

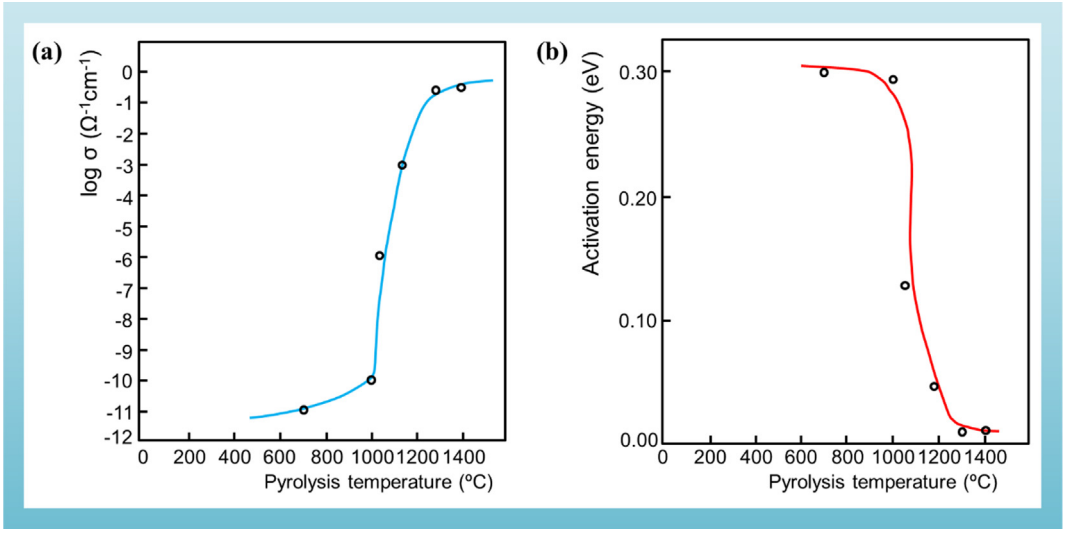

Fig. 32. Variation of the electrical conductivity (σ) of a SiC-based ceramic at 20 °C as a function of pyrolysis temperature (a) and the activation energy for the temperature-dependent electrical conductivity of the ceramics obtained at different temperatures (b) (reprinted with permission of Springer Nature) [308].

different temperature regimes, namely, the conduction in extended states occurring in the high-temperature range, the conduction in band tails occurring within the middle temperature range and the conduction in band tail hopping instead of VRH occurring in the low temperature regime [192]. Consequently, due to the amorphous nature, a better understanding of the semiconducting behavior of these materials still requires more in-depth fundamental studies concerning both microstructural characterization and electric properties.

The influence of structural evolution of free carbon on the electric properties of the PDCs is clearly reflected on the variation of the electrical conductivity (σ) and its temperature dependence (the apparent activation energy, ΔE) as a function of pyrolysis/annealing temperatures. This effect has been widely reported in various PDCs, such as Si−C [169,188,189,195,308,549], Si−C−O [361,423], Si−C−N [191,550,551], and Si−B−C−N [536] systems. Generally, the PDCs pyrolyzed at temperatures lower than 600–800 °C can be better described as insulators due to their rather low DC electrical conductivity ($\sigma < 10^{-10}$ S/cm). For amorphous PDCs obtained at pyrolysis temperatures higher than 800–1000 °C, it shows a typical amorphous semiconducting behavior with a temperature-dependence feature. After further annealing at temperatures higher than 1200–1400 °C, metallic-like (electron) conduction with electrical conductivity up to 1 S/cm can be measured in the polycrystalline PDCs which usually possess a percolation network of graphitic free carbon (see Fig. 30a) [18].

For instance, Bouillon et al. investigated the variation of electric properties of a SiC-based ceramic derived from polycarbosilane as a function of pyrolysis temperatures (T_p), and the results are shown in Fig. 32. As $T_p < 1000$ °C, the pyrolytic residues are insulators with an electrical conductivity (σ) lower than 10^{-10} S/cm at 20 °C and a ΔE of 0.7 eV. For 900 °C $< T_p <$ 1200 °C, the σ undergoes a dramatic transition, *i.e.*, the σ value at 20 °C increases by a factor of ten orders of magnitude and the ΔE value reduces to be lower than 0.01 eV. When $T_p > 1200$ °C, the ambient σ remains almost constant (close to 1 S/cm), and the ΔE is almost zero (Fig. 32b), which suggests a partly metallic behavior as in the related case of Nicalon fibres [308]. Such a process has some similarity with that of the pyrolysis of hydrocarbon polymers into pyrolytic carbon, and therefore it can be explained on the basis of the following mechanisms: *(1)* $T_p < 1000$ °C, the nucleation of segregated carbon already starts, mainly in the form of basic structural units (BSUs). However, the size of the segregated carbon is rather small, and the nature of the carbon is amorphous with a very low sp^2 to sp^3 ratio due to a large amount of faulted and hydrogenated carbon atoms (sp^3 hybridized) present at the periphery of the aromatic layers (see Fig. 18). Accordingly, either a low mobility or a low concentration of charge carriers results in a low σ and a high ΔE of the SiC-based ceramics. *(2)* 900 °C $< T_p <$ 1200 °C, the size of segregated carbon as well as the sp^2 to sp^3 ratio increases significantly via edge-to-edge linkage of neighboring free carbon units realized by elimination of hydrogen atoms. From a macroscopic point of view, the coalescence of conducting free carbon nanodomains beyond the percolation threshold gives rise to a sharp insulator-quasi metal transition. (3) $T_p > 1200$ °C, the growth and graphitization (*i.e.*, sp^3-to-sp^2 transition) of the free carbon regions are almost done and the percolation network already forms. As a result, the electric behavior of the SiC-based ceramics does not change too much [308]. This discussion is consistent with the structural evolution of free carbon as a function of heating temperatures reviewed in Section 4.3.

In other PDC systems, similar electrical behavior has been widely analyzed, but the transition temperature range sometimes is different due to the distinct thermal stabilities of precursors and resultant ceramics [169,188,189,191,195,361,423,549–551]. The DC conductivity of some PDCs can increase by several orders of magnitude with increasing pyrolysis temperature even before crystallization [191,192,548]. An's group found that the increase of electrical conductivity of the PDCs as a function of pyrolytic temperatures appears to obey Arrhenius dependence in both carbon-rich and carbon-poor systems, and the apparent activation

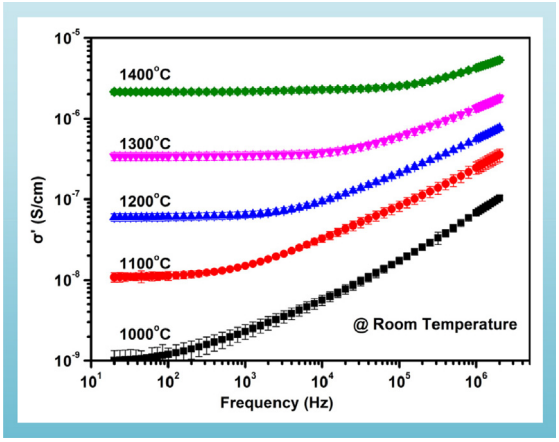

Fig. 33. The AC conductivity of amorphous SiCN ceramics annealed at different temperatures, as a function of frequency (reprinted with permission of Elsevier) [553].

energy is around 3.4 eV, which is coincided with the activation energy of sp^3-sp^2 transition (3.3–3.6 eV) during heat-treatment (see Section 4.3). Moreover, Shao et al. found that microwave post-treatment seems to be more effective to induce the sp^3-to-sp^2 transition than conventional heat treatment, as it can heat up the amorphous free carbon locally. In this work, the SiCN ceramic monoliths (obtained at 1000 ˚C) after microwave post-treatment to 1000 ˚C exhibit electrical conductivity around 40 times higher than that of the SiCN monoliths post-treated by conventional heating to the same temperature [552]. The results further confirm that the increase in the electrical conductivity of PDCs is mainly attributed to the increase in electrical conductivity of the free carbon phase via sp^3-sp^2 transition during pyrolysis and annealing (or microwave post-treatment) [195,538,551,552]. A simple model based on the electric field concentration has been proposed to explain this phenomenon [551].

The researches mentioned above is primarily focused on DC electrical conductivity of the PDCs. The studies regarding the alternative current (AC) conductivity of PDCs have also been reported recently [527,548,553–555]. Wang et al. investigated the complex impedance behavior of SiOC ceramics pyrolyzed at different temperatures. They found that the segregation of free carbon changed the complex impedance spectra of SiOC ceramics from one semicircle to two semicircles, and therefore two impedance mechanisms are involved in the ceramics synthesized at temperatures ≥ 1000 ˚C. Moreover, the complex impedance spectra show that the relaxation time of free carbon is much longer than that of the ceramic matrix, which indicates a much higher defect concentration in the free carbon [527].

Ma et al. systematically investigated the AC conductive behavior of an amorphous SiCN ceramics prepared from a commercially available liquid polysilazane [553]. The results clearly demonstrated that the AC conductivity of the amorphous SiCN ceramics exhibits a frequency-dependent switch: in the low frequency range, the conductivity is constant, whereas, in the high-frequency range, the conductivity increases with frequency (see Fig. 33). Interestingly, the AC conductivity in the whole frequency range obeys Arrhenius dependence with respect to annealing temperature with the same activation energy as the DC conductivity mentioned above, and it is essentially the same as the activation energy for the sp^3-to-sp^2 transition of the free-carbon phase. Moreover, the conductivities in both high- and low-frequency region follow a band-tail hopping process with respect to the testing temperature. The following mechanisms were proposed to explain these observations: *(1)* the frequency-independent conductivity in the low frequency region is dominated by a long-distance transport of charge carriers via matrix-free carbon path, which is enhanced by an electric-field concentration effect as mentioned above; while the frequency-dependent conductivity in the high frequency region is dominated by an interfacial polarization process governed by charge carrier relaxation in the free-carbon phase [553]. The results indicate that the free carbon strongly affects the AC conductivity of amorphous SiCN ceramics as well. The studies also indicate that the characterization of AC conductivity is a powerful method to investigate the fate and role of free carbon within the PDCs [527,553,554].

7.1.2. Piezoresistivity

Around ten years ago, a rather new finding concerning the ultrahigh piezoresistivity (*i.e.*, the variation of the electrical resistivity due to an applied stress) of amorphous PDCs has been firstly reported by Zhang et al. from An's group. In this work, an extremely high piezoresistive coefficient (also known as gauge factor) along both longitudinal and transverse directions has been detected in the SiCN monoliths, which is in the range of 1000 to 4000 and much higher than any existing ceramic materials [202]. Later on, the piezoresistive behavior has also been found in SiCNO, SiCO and SiAlCO ceramics with the piezoresistive coefficients amount to 100–1700, 145 and 7000–16000 respectively [48,201]. Particularly, SiCNO ceramics exhibit large piezoresistive coefficients at 700 ˚C to 1000 ˚C, and the values depend on both the stress and temperature, indicating them ideal candidates for sensors used in harsh environments [48]. Fig. 34 presents the piezoresistivity behavior of the SiCN and SiOC PDCs at room temperature.

Several studies demonstrated that the piezoresistive effect is dominated by the tunneling-percolation mechanism related to the presence of graphitic free carbon within the framework of the nanodomain structural model of PDCs proposed by Saha et al. (see Fig. 30b in Section 7.1). It's well accepted that the graphite-like free carbon in the ceramic matrix forms a tunneling-percolation

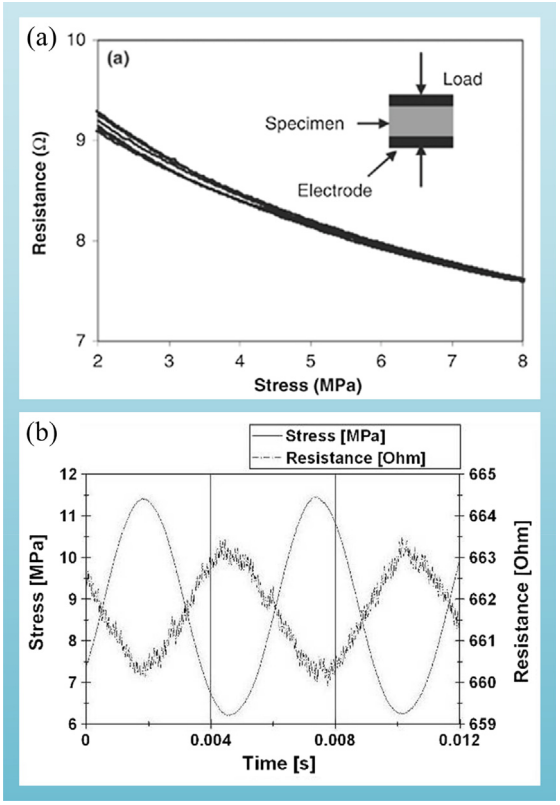

Fig. 34. Experimental proof of the piezoresistive response of (a) SiCN and (b) SiOC (both reprinted with permission of Wiley) [202,230].

structure. The resistivity of the ceramics is therefore determined by a tunneling process and is sensitive to the distance between the free carbon clusters. The slight decreases or increases in the distance between the free carbon clusters caused by the applied stress can lead to a significant variation in the resistivity, resulting in a high piezoresistive coefficient [48,55,201–203,230,556].

7.2. Electrochemical properties as electrode materials for lithium ion batteries

PDCs used as electrode materials for lithium ion batteries has been proposed very early by Dahn et al. in some patent applications since the middle of 1990s [102,557,558]. In recent 10 years, this topic has attracted increasing attention because the PDC-based anode electrodes are found to possess many desirable properties superior than or unobtainable for other materials [98,524,559–565]. For instance, the PDCs (mainly regarding the SiCN- and SiOC-based ceramics) are chemically inert with respect to battery components and are able to minimize the agglomeration of lithium ions. The PDCs are light weight but possess excellent mechanical properties. Importantly, the preceramic polymers are able to provide the PDCs with an excess of free carbon which is possible to form a continuous network for electric conduction and lithium-ion storage [561,566,567]. The silicon-based matrix also can protect the free carbon from exfoliation during charging and discharging, making it more stable than free-standing carbon materials [200]. Furthermore, the chemical and physical properties of PDCs can be designed via tuning the molecular structure of starting polymers and/or controlling the thermal-treatment parameters (*e.g.*, temperature, holding time and atmosphere) as reviewed above [99,568,569].

The role of free carbon on the electrochemical properties of PDCs as anode materials for lithium ion batteries has been found to be crucial despite that no linear relationship between the capacity and the free carbon content exist in both SiOC and SiCN materials [567,570]. Numerous studies demonstrate that carbon-rich PDCs exhibit much better electrochemical activity than the carbon-poor PDCs [99,199,200,562,563,566,570,571]. For instance, in 2006, Kolb et al. reported that anodes prepared by pure polyvinylsilazane-derived SiCN ceramic with low free carbon content show a discharge capacity < 40 mAh/g if no other conductive additives are introduced [33]. In the contrary, Graczyk-Zajac et al. investigated the electrochemical behavior of carbon-rich SiCN ceramics derived from poly(phenylvinylsilylcarbodiimide) as anode materials for lithium ion batteries. In this work, the capacity of the sample prepared at 1300 °C appears to be stable upon galvanostatic cycling and reaches almost 300 mAh/g with oxygen as the impurity [199]. Later on, the reversible capacity of carbon-rich SiCN-based anodes has been improved to be higher than 700 mAh/g with excellent cycling stability by Reinold et al. in the same research group (Fig. 35) [570].

For the SiOC-based ceramics, it is found that the amount of free carbon phase has no significant impact on the first cycle lithiation and delithiation capacities (which are proposed to be determined by the amount of SiOC phase) [560,572]. However, the

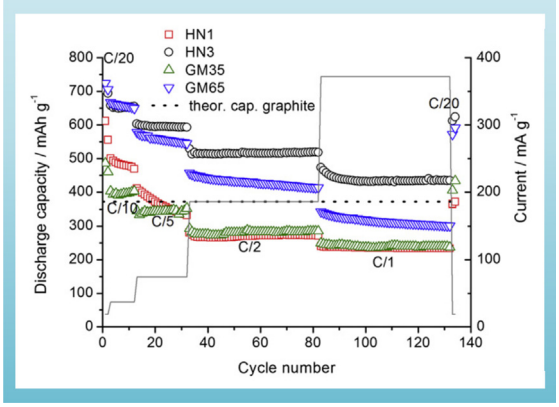

Fig. 35. Discharge capacities with corresponding rate capacities at various current rates for carbon-rich SiCN ceramics as anode materials for lithium ion batteries: HN1 ($SiC_{5.3}O_{0.2}N_{1.2}$ with 56 wt% of free carbon), HN3 ($SiC_{3.9}O_{0.1}N_{0.8}$ with 48 wt% of free carbon), GM35 ($SiC_{3.0}O_{0.2}N_{1.9}$ with 52 wt% of free carbon) and GM65 ($SiC_{3.2}O_{0.1}N_{0.9}$ with 43 wt% of free carbon). C/10, C/5, C/2 and C/1 represent the charging/discharging rates of 36, 72, 180 and 360 mA/g, respectively (reprinted with permission of Elsevier) [570].

experimental results suggest that, among the various chemical compositions, the stoichiometries with an exceptionally high free carbon content are the most promising anode materials for lithium ion batteries in terms of high reversible capacity (up to 900 mAh/g), good rate capability as well as reliable cycling stability over hundreds of cycles [37,101,561,573–579]. Furthermore, it has been proven that the electrochemical properties of PDCs as anode materials can be strongly affected if one changes the status of the free carbon (*e.g.*, amount, crystallinity or disordering) by varying the thermolysis parameters or microstructure of the PDCs. For example, appropriate heating temperature is always very important for the PDCs to maintain their electrochemical properties via keeping the free carbon in amorphous or highly disordered nature [568,575,576]. Graczyk-Zajac et al. found that the evolution of the capacity of the SiCN-based anode materials as a function of thermolysis temperature was found to be quite similar to that of soft carbons as reported in the literature [580], which proves that the segregated carbon plays a crucial role in the electrochemical activity of the SiCN materials [199]. In addition, compared with the SiOC ceramics without mixed bonds, the presence of SiO_xC_y mixed bonds in the ceramics induces the formation of a more disordered/high defect free carbon phase, leading to a higher capacity for reversible storage of Li ions [581].

The free carbon contributes to the electrochemical properties of PDCs at least in two aspects, as follows: *(1)* The lithium storage is directly correlated with the electron transfer through the electrode materials because the storage of lithium ions must be accompanied by a fast electron countercharge transport. The free carbon content can improve the lithiation capacities of PDCs by way of effectively enhancing their electrical conductivity [567]; *(2)* The free carbon phase within the PDCs provides the major hosting sites for revisable Li ions, including the edge of the graphene layers, interstitial spaces and defect sites of the free carbon (Fig. 36), similar to the storage of Li-ions in disordered carbons. Thus, the high revisable capacity and excellent cycling stability of the PDC-based anode materials can be correlated to the presence of free carbon [37,101,559,561,572,574,581,582]. For instance, Baek et al. proves

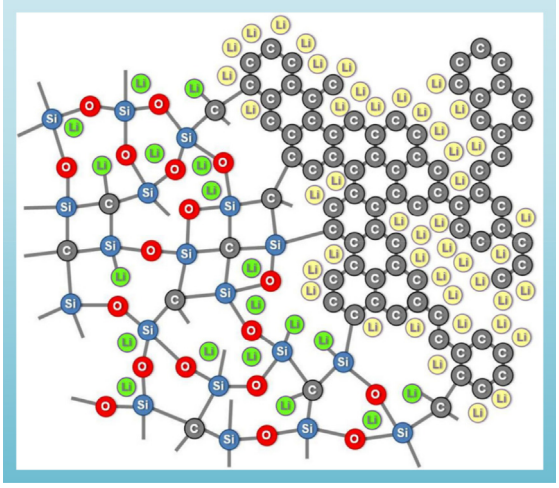

Fig. 36. Schematic model for the reversible and irreversible lithium ions storage in SiOC ceramics- The irreversibly captured Li ions in the SiOC matrix are in green color, while the reversibly Li-ions stored in the free carbon phase are marked in yellow (reprinted with permission of Wiley) [116].

that the free carbon phase acts as major electrochemically active sites for Lithium ion storage by means of systematic NMR studies on two carbon-rich SiCN ceramics derived from polyphenylvinylsilylcarbodiimide and polyphenylvinylsilazane, respectively. The results show that only the ^{13}C spectrum is strongly influenced by Li insertion/extraction [566].

The experimental observations have been confirmed by computational simulations based on first-principle studies [583–586]. Kroll et al. found that the storage of lithium ions in amorphous silica and SiOC without segregated carbon is energetically unfavorable because of a large bandgap, whereas the bandgap of SiOC ceramics can be remarkably reduced by the presence of the low laying unoccupied states stemming from the free carbon phase. Accordingly, on the one hand, the free carbon facilitates lithium ions bonded to oxygen sites via improving the electronic conduction, leading to irreversible lithium uptake. On the other hand, the free carbon contributes a major part of the reversible lithium storage capacity [586]. Liao et al. further confirmed these findings through calculating the theoretical specific capacity and reversible capacities of different SiOC compositions. They claim that the stoichiometric SiOC glass presents very low reversible capacity, whereas the reversible capacity of the SiOC ceramics increases with increasing free carbon content. Interestingly, they also found that, after reaching a maximum value, the capacity of SiOC ceramics begins to decrease with further increasing the carbon content. This behavior has been also proven in experiments [583–585]. Liu et al. demonstrated that improving the electrochemical performance of the SiOC and SiCN ceramics via increasing free carbon content is effective only in the case of intrinsically carbon-poor preceramic polymers. Nevertheless, the stability of the anode materials might be reduced if the amount of the free carbon exceeds a certain threshold [587].

7.3. Dielectric properties for electromagnetic wave absorbing and shielding applications

Electromagnetic (EM) wave absorbing and shielding materials have attracted especial attention in the past decades because of the massive increase of high frequency (in GHz range) electronic components and electronic devices, notably in telecommunication (0.8–1.5 GHz), LAN systems (2.45, 5.0, 19.0, 22.0, 60.0 GHz) and satellite broadcast systems (11.7–12.0 GHz), which generate electromagnetic pollution and cause serious electromagnetic interference (EMI) [504,588,589]. PDCs (incl. composites) are considered to be one promising choice for EM absorbing or shielding materials used in harsh environment and/or under high mechanical load due to their tunable dielectric properties and conductivities, low density, excellent high-temperature mechanical properties, oxidation and corrosion resistance as well as thermophysical and chemical stabilities [42,87,120,418,590–602]. The EM absorbing or shielding performance of PDCs has been reviewed in literatures and therefore will not be discussed herein [87,196,603,604].

When talking about the EM absorbing and shielding performance of a non-magnetic material, the dielectric property of the material should be considered first because of the impedance matching requirements [87]. The dielectric property can be expressed by a complex permittivity ($\varepsilon = \varepsilon' - j\varepsilon''$), where ε' is the real part of the permittivity and ε'' the imaginary part of the permittivity. If the materials possess very low ε' (1–5) and ε'' (< 0.01), they are EM transparent materials; the materials with low ε' (5–20) but intermediate ε'' (1–10) are considered as EM absorbing materials; If the materials have both high ε' (> 20) and ε'' (> 10), they may be suitable for EM shielding materials [87]. The EM absorbing and shielding performance of PDCs are mainly conducted in gigahertz range from 2 to 18 GHz, including the S-, C-, X- and Ku-bands [87,599,602,605,606]. Some reported complex permittivity of the PDCs at a specific frequency (10 GHz) are shown in Fig. 37 [604]. It appears that the complex permittivity of the crystallized PDCs obtained at elevated temperatures is higher than that of the amorphous PDCs obtained at lower temperatures. The complex permittivity (Fig. 37) indicates that PDCs are usually suitable for EM absorbing applications. In some cases, actually, carbon-rich PDCs as well as the PDCs with conductive fillers are available for EM shielding applications due to their improved complex permittivity and conductivity [84,607–610].

The free carbon acting as a dielectric loss phase contributes to both ε' and ε'' of the PDC materials [198,606,611–613]. Li et al. measured the complex permittivity of polymer-derived SiCN ceramics with and without free carbon. They found that, after removal of the free carbon, the ε' and ε'' values of the samples decreases from ≈11 and 5 to ≈6 and 0.7, respectively [198]. It's well known

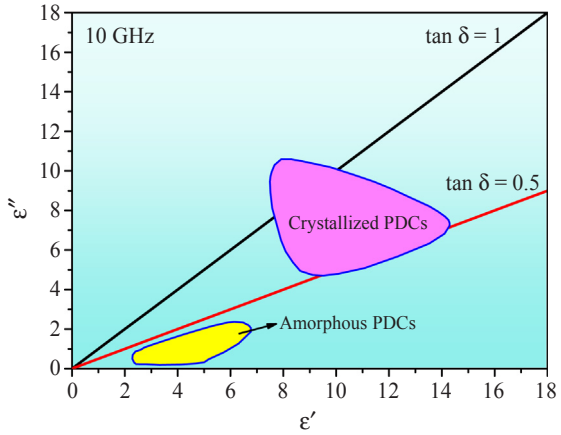

Fig. 37. Complex permittivity range of some reported PDCs (*e.g.*, SiC, SiCN, SiOC and SiBCN) under the frequency of 10 GHz [604].

that, ε' is related to the polarization effect of bound charge carriers which can be induced by electric field of the incident EM waves. According to the Debye theory, the ε' can be described as follows [595,614,615].

$$\varepsilon' = \varepsilon_\infty + \frac{\varepsilon_s - \varepsilon_\infty}{1 + [\omega\tau(T)]^2} \tag{7.5}$$

where ε_s is static relative permittivity, ε_∞ is relative permittivity at high-frequency limit, ω is the angular frequency of incident electromagnetic wave, $\tau(T)$ is temperature-dependent relaxation time of polarization. Thus, the free carbon appears to improve the ε' value via the following two mechanisms: *(1)* the heterogeneous interfaces between free carbon and ceramic matrix give rise to the interfacial polarization (also called space charge polarization) resulting from the accumulation of charge carriers [85,197,603,606,609–613,616]; *(2)* a large number of defects and dangling bonds exist in the free carbon nanodomains due to the disordered structure, which is able to enhance the polarization under EM electric field [86,197,606,608,611–613].

The effect arising from both free and bound charge carriers gives rise to the imaginary part of the permittivity (ε'') which leads to the dielectric loss ($\varepsilon''/\varepsilon'$). Based on the Debye theory, the ε'' can be described as [615]:

$$\varepsilon'' = \frac{\varepsilon_s - \varepsilon_\infty}{1 + [\omega\tau(\mathrm{T})]^2}\omega\tau(\mathrm{T}) + \frac{\sigma(\mathrm{T})}{2\pi\varepsilon_0 \mathrm{f}} \tag{7.6}$$

where $\sigma(T)$ is temperature-dependent electrical conductivity, ε_0 is the permittivity of vacuum (8.854×10^{-12} F/m) and f is the frequency of incident electromagnetic wave. The first part of the equation is related to the polarization loss of the materials, and the second part is contributed by the electric conduction loss (*i.e.*, Ohmic loss). The segregated free carbon within the PDCs has a high electrical conductivity in the range of 1–10^5 S/cm, depending on it structural evolution at different pyrolysis temperatures [423]. Consequently, in addition to the polarization loss, the free carbon also leads to the conduction loss, which increases the ε“ and the dielectric loss ($\varepsilon''/\varepsilon'$) of the PDCs [86,197,608–612,617]. Moreover, the structural evolution of free carbon as a function of pyrolysis/annealing temperatures strongly affects the variation of complex permittivity of the PDCs and their EM absorbing and shielding performance. Generally, the PDCs obtained at higher temperatures exhibit higher ε' and ε'' values because of more completely segregated free carbon and improved electrical conductivity of the free carbon after graphitization [86,197,198,603,608,610,611,618]. Furthermore, as discussed in Section 7.1.1, the electrical conductivity of the free carbon and amorphous PDCs is temperature dependent. Consequently, the dielectric properties and resulting EM absorbing/shielding performance of the PDC materials should be also strongly influenced by their working temperatures [615]. But the effects of free carbon on the high-temperature dielectric properties and EM absorbing/shielding performance of the PDCs is rarely reported and systematically discussed up to now [610].

7.4. Optical properties

The optical properties of materials are used to define how they interact with light. The optical properties of PDCs are mainly concerning their photoluminescent behavior. Several studies related to the photoluminescent properties of PDCs (*e.g.*, SiCN [95,619], SiOC(H) [97,297,528,530], SiBN [620,621], SiBOC [622] and SiCNO [94,623]) have been reported in recent years despite that it is very hard to investigate due to the presence of free carbon. The free carbon can strongly absorb the emitted visible light, which is therefore detrimental for the photoluminescent behavior of PDCs [528,529].

In order to investigate the photoluminescent properties, the free carbon content should be extremely low. One strategy for eliminating the free carbon is selection of appropriate molecular structure and chemical composition of the starting precursor allowing for the synthesis of PDCs with a minimum amount of free carbon [624,625]. For instance, Karakuscu et al. prepared a stoichiometric SiOC film with rather low free carbon content via controlling the starting sol-gel-composition and the pyrolysis temperatures [528]. It was found that the stoichiometric SiOC films obtained at low pyrolysis temperature (800–1000 ˚C) yield UV-blue luminescence (410 nm), whereas higher preparation temperatures (≥1100 ˚C) favor green-yellow luminescence (560 nm)

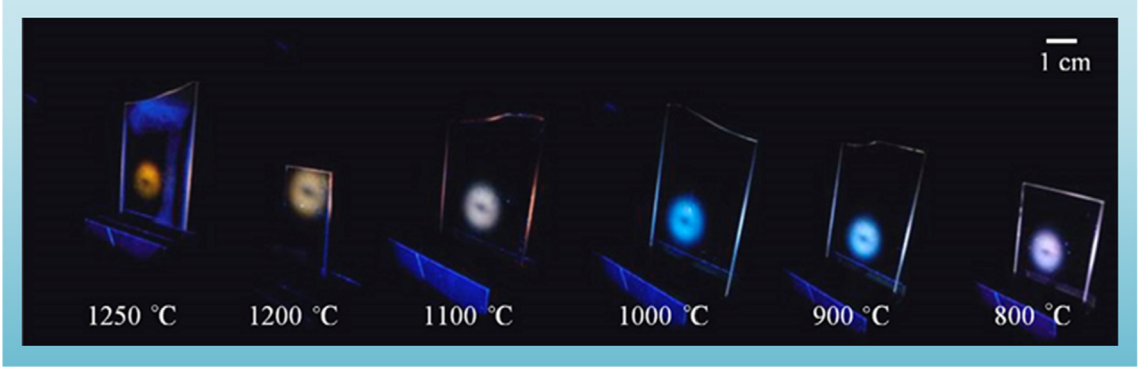

Fig. 38. Photoluminescence of SiOC films with ultralow free carbon content pyrolyzed from 800 ˚C to 1250 ˚C under UV laser excitation (reprinted with permission of Wiley) [528].

(Fig. 38). The UV-blue luminescence is attributed to defect states present in the matrix (*e.g.*, dangling bonds). The variation of color at higher temperatures results from the formation of SiC phase and precipitation of a rather small amount of free carbon (cannot be detected by analysis) during phase separation, which contribute to the luminescence in the green (550–570 nm) and yellow (580 nm) range, respectively. However, they suggest that the amount of free carbon in the SiOC films should be kept very low in order to improve the emission. A high excess of free carbon strongly absorbs the emitted visible light. Thus, the C-rich SiOC films did not provide any noticeable luminescence. Actually, the carbon-rich SiOC films show poor luminescent property although their free carbon content is less than 0.075 mol% [528,625].

Another approach for removal of free carbon is pyrolysis of the preceramic precursor in a hydrogen atmosphere at appropriate temperatures [297,626]. Narisawa et al. observed a long-lived photoluminescence decaying within a time range of 1.0–4.0 s in an amorphous Si-O-C(-H) ceramics prepared using this method [530]. Moreover, addition of boron is also able to reduce the amount of free carbon in the SiBOC ceramics by forming new B—C bonds, which can increase the complexity of the amorphous network by forming mixed boron oxycarbide units ($BO_{3-y}C_y$, $0 \leq y \leq 3$) and give rise to a wide distribution of emitting centers. As a result, a high efficient, strong broad-band tunable visible emission has been characterized from the SiBOC ceramic thin films [622].

7.5. Others

In addition to the promising carbon-related functional properties as mentioned above, some new properties of the PDCs and composites have been studied in recent years, such as biocompatibility and bioactivity [113,114,627], thermoelectric property [628], photo- and electrochemical- catalytic activity [629,630], adsorbing capability [631–634] as well as gas separation capability [635–637], where the free carbon may also determine the respective performance. For instance, the free carbon might influence the biocompatibility of the SiOC ceramics because of its similarity to pyrolytic carbon which is generally well tolerated by animal cells [638,639]. The free carbon network plays an important role in the thermoelectric properties of PDCs because it affects both, the electrical and thermal conductivity of these materials as reviewed above [313,472,475]. The electrochemical catalytic properties of PDCs should also be affected by the free carbon due to its effect on the electrical conductivity. However, up to now, no systematic research has been conducted to study these effects in detail.

8. Advanced applications of PDCs related to the *in situ* formed carbon

8.1. Structural applications

8.1.1. Ceramic fibers

As mentioned at the start of the article, the potential of the PDCs for materials science was not recognized until people manufactured small-diameter ceramic fibers via thermolysis of polyorganosilicon precursors in 1970s [4–10]. Up to now, the ceramics fibers (mainly SiC-based fibers) is still the most successful commercial application of the PDCs. For example, the SiC-based fibers have been applied as heat-resistant materials and as reinforcement for polymer matrix composites (PMCs) and ceramic matrix composites (CMCs) used for structural components in aircraft. The PMCs are being used in aircraft bodies and wings, while the CMCs are being used in exhaust flaps, seals of jet engines for a fighter and being introduced in heat-resistant parts of the new GE LEAP jet engines for passenger planes. Moreover, the felts made of SiC fibers have been used in the particulate filters for automobile engines running on sulfur-rich diesel [117,253].

The SiC-based ceramic fibers are mostly derived from polycarbosilane or polymetallocarbosilane precursors and can be classified into three generations according to their oxygen content and C/Si atomic ratio [117,253]. Because of different processing techniques, the SiC fibers have distinct microstructures (Fig. 39). The first-generation fibers are Si—C—O (Nicalon) fibers and Si—Ti—C—O (Tyranno Lox M) fibers which were developed in the 1980s. These fibers exhibit degraded strength at temperatures above 1300 °C, and therefore their maximum working temperature is only 1100 °C. This is because of the presence of large amount of oxygen (up to 11 wt%) and free carbon (the C/Si ratio is around 1.3–1.4). The typical second-generation fibers are SiC (Hi-Nicalon) fibers [117]. The oxygen content of the fibers is significantly reduced to less than 1 wt% by alternating the oxygen curing process into electron beam irradiation curing in Helium atmosphere. The strength retention temperature of these fibers was improved up to 1500 °C. However, their creep resistance is limited to a maximum of 1150 °C because the free carbon content is still very high (the C/Si ratio is around 1.4). Considering that the cost of irradiation curing process is too expensive for commercial applications, some second-generation fibers (*e.g.*, Tyranno ZM fibers) still use oxygen curing process. But the stability of the fibers was enhanced by way of changing the metal element grafted to the PCS polymer (*i.e.*, the titanium was replaced by zirconium). The third-generation fibers (*e.g.*, Hi-Nicalon Type S, Tyranno SA, and Sylramic TM fibers) are stoichiometric SiC fibers with C/Si ratio near to 1 and rather low oxygen content (< 1 wt%). They exhibit improved thermal stability and creep resistance up to 1400 °C [253]. From the developing history of the ceramic fibers, we can see that, in order to improve the performance of the fibers, the manufacturers tried several methods to reduce the oxygen content and to prepare the stoichiometric SiC fibers via controlling the chemistry of the preceramic precursors, grafting other metal elements to the polymers as catalysts and sintering aids as well as annealing the fibers at temperatures higher than 1700 °C in argon (Tyranno SA and Sylramic TM fibers) or at 1500 °C in H_2 (Hi-Nicalon Type S fibers) [70,117]. It seems that the free carbon is detrimental to the high temperature performance of the ceramic fibers. Actually, an appropriate amount of free carbon is important for the strength retention temperature of the fibers because it provides a unique grain growth mechanism which can prevent an explosive growth of the SiC grains and hinder a catastrophic fall in strength (see discussion in Section 5.3.1). For instance, a small amount of free carbon is left deliberately in the Hi-Nicalon-Type-S fibers (the C/Si ratio is 1.05),

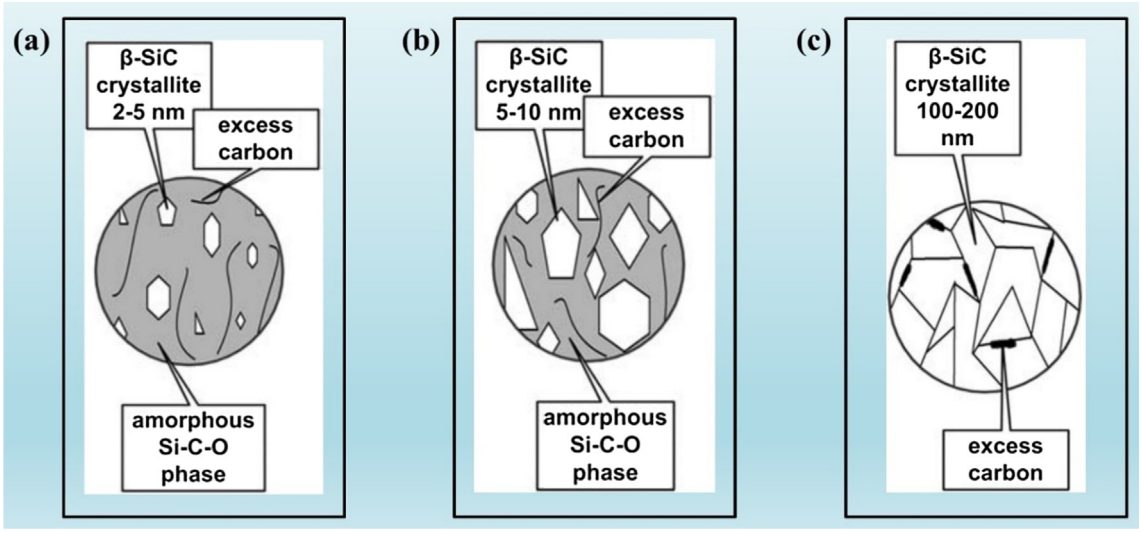

Fig. 39. Schematic structure model of commercially available SiC fibers: (a) first generation; (b) second generation; (c) third generation [212].

as it serves to limit grain growth of SiC into 50 nm and leads to good strength retention of the fibers tested at room temperature after exposure in argon for 10 h at temperatures up to 1600 °C [117,451]. Currently, the ceramic fibers derived from polysilazane are not commercially available [212], and only $SiBN_3C$ fibers have been produced in a pilot plant. The $SiBN_3C$ fibers are able to keep the amorphous state up to 1800 °C and have good high-temperature creep resistance [640,641]. However, further studied are needed to realize their industrial applications in the near future. More details of manufacture and the elemental composition of the fibres can be found in some review articles [117,212,253,451,641].

8.1.2. Ceramic matrix composites (CMCs)

CMCs are promising candidates for structural applications requiring high strength, excellent damage tolerance at elevated temperatures and low specific weight. They overcome the major disadvantages of traditional engineering ceramics, such as low fracture toughness, brittle and limited thermal shock resistance [641]. In addition, some other areas of applications (*e.g.*, pump sealings in chemical engineering and brake discs in transportation systems) are emerging in recent years [642]. Preceramic polymers have been widely used for the fabrication of CMCs in two different aspects: *(1)* providing reinforcement as ceramic fibers as mentioned above; *(2)* producing the ceramic matrix via polymer infiltration (or impregnation) & pyrolysis (PI&P) process. Compared to other technologies (*e.g.*, CVI, slurry method), preceramic polymers offer a lot of advantages, such as simpler and cheaper equipments, lower processing temperatures (which is good for strength retention of ceramic fibers), shorter cycle times, deeper infiltration depth, more homogeneous and the capability for fabricating very large and complex parts [24,25,642]. In addition, the preceramic polymers can be chemically modified with other elements (*e.g.*, Ti, Zr, Hf) to prepare CMCs with homogeneously nanostructured matrix [61,231,245,489,643–645]. Moreover, the CMCs can be machined to near-net shape before full densification and hence no extensive final machining (*e.g.*, eliminating fixtures or excess external silicon) is needed [18]. One good example is the application as brake components for high performance motorbikes (see Fig. 2j), with potential for use also in automobiles, trucks, (high-speed) trains, and airplanes [646]. Ceramic rotors were fabricated using carbon fibers as reinforcement and a polycarbosilane with SiC particles as fillers. After several times of infiltration and pyrolysis, a dense ceramic rotor can be produced. Such ceramic brake systems promise a better brake performance with a longer lifetime of the disks, better coefficient of friction, higher brake forces and delay, less wear in comparison with metal ones as well as the exclusion of fading. These advantages provide better driving comfortability and more security for motorcyclists. Furthermore, the lower density of the ceramic brake disks in comparison with metallic disks is another important advantage for light-weight requirement [18,82].

The free carbon present within the CMCs (in fibers or ceramic matrix) should also affect their structural properties (*e.g.*, tensile strength, flexural strength, Young's modulus, oxidation resistance, corrosion resistance and tribological properties) as discussed in Section 6 despite the influence has not been systematically investigated in CMCs. In addition, it is well known that a thin layer of pyrolytic carbon or boron nitride on the fibers weakens the bond at the fiber/matrix interface, which is crucial for production of CMCs with high crack resistance (by fiber "pull-out" at crack surfaces). The free carbon in either fibers or ceramic matrix might also affect the bond strength between the fiber and the ceramic matrix, which is still under discussion. The role of free carbon on the performance of CMCs for different applications (*e.g.*, heat shield systems, turbine blades, pump sealings and brake discs) under various conditions (at high temperatures or in aggressive media) requires further in detailed investigations.

8.1.3. Coatings

In addition to fibers and CMCs, another important application of PDCs is the possibility of preparing ceramic coatings and membranes by using liquid phase deposition (*e.g.*, lacquer technology, dip coating, spray coating and spin coating) and subsequent

Table 4
Summary of polymer-derived ceramic coating systems (PT = processing temperature).

Precursor systems	Coatings	Substrates	PT [°C]	Ref.
Polyhydridomethylsiloxane	SiOC	Carbon Steel/Stainless Steel	600/700	[694]
Polyhydridomethylsiloxane	SiOC	Stainless steel (AISI 304)	800	[695]
Polyhydridomethylsiloxane	SiOC	316 stainless	800	[20]
Polyhydromethylsiloxane	SiOC	Stainless Steel 316 (UNS S31600)	800	[75]
Polysilazane	SiCN	13CrMo4-5 (AISI A182)/X5CrNi18-10 (AISI 304)	700	[648]
Perhydropolysilazane/ABSE polycarbosilazane	Si_3N_4/SiCN	Stainless steel (AISI 304)	1000	[649]
Polymethoxymethylsiloxane/Hydroxy-terminated linear dimethylpolysiloxane	SiOC	Stainless Steel (#1.4301 DIN EN 10027-2)	1000	[696]
ABSE polysilazane	SiCN	Carbon fiber (Tenax HTA 5411 12k)	800	[647]
Perhydropolysilazane/KiON HTT1800	Si_3N_4/SiCN	Mild steel (13CrMo4)/stainless steel (AISI 304)	800	[21]
Polysiloxanes mixed with barium strontium aluminosilicate (BSAS)	SiOC-BSAS	C_f/SiC composite	1350	[217]
Polycarbosilane and polyvinylsilane	SiC	Porous Al_2O_3	850	[655]
Methylhydroxylsiloxane/phenylmethylhydroxylsiloxane	$SiO_xC_yH_z$	Silicon/SiO_2	C and Au ion irradiation	[657]
Allylhydridopolycarbosilane/Polycarbosilane (PCS)	SiC_xH_y	Silicon/SiO_2	C and Au ion irradiation	[657]

pyrolysis, which is a low-cost alternative to PVD and CVD methods [647]. In order to produce thick coatings (up to hundreds of micro-meters), multiple deposition steps or loading active/inert fillers can be used to minimize the amount of isotropic shrinkage as well as the resultant cracks and stresses at the substrate/coating interface [21,648]. Moreover, the processing temperature can be kept rather low (< 800 °C) to minimize damages to the substrate (Table 4). This is particularly important for the metal substrates with relatively low melting point. The reactions occurring at the substrate/coating interface during processing can also improve adhesion with the metal substrate despite that the formation of brittle phases should be avoided [20].

The PDC-based coatings have shown various applications, such as thermal/environmental barrier coatings (TBCs/EBCs) for oxidation, corrosion and mechanical protection of C/C composites, carbon fibers and metals [20,21,73–75,217,469,647–653], porous layers/membranes for catalyst support, biomedical devices or hot gas separation [654–656], as well as functional layers for microelectronic and optoelectronic devices [290,295,657,658]. Table 4 lists the well-known PDC coating systems. As reviewed in Sections 6 and 7, the presence of free carbon is expected to improve the performance of the coatings via enhancing their thermo-mechanical properties (*e.g.*, hardness, creep resistance), thermal stabilities (with respect to crystallization and decomposition), corrosion resistance, tribological properties, electric properties as well as adjusting the optical properties, thermal expansion coefficient and thermal conductivity of the materials. Nevertheless, the fundamental studies regarding the influence of free carbon on the performance of PDC coatings are rarely reported.

8.2. Functional applications

8.2.1. Sensors

Both SiCN and SiOC ceramics have been reported to exhibit excellent piezoresistive properties with extremely high piezoresistive coefficient along both longitudinal and transverse directions even at high temperatures (see Section 7.1.2). Based on this property, the SiCN and SiOC ceramics can be used as sensors for sensing pressure, vibration, acceleration as well as chemical and bio species [48,57,201,202,659,660]. PDCs have been also shown to hold promise for flux sensors or temperature sensors used in harsh environment based on their temperature-dependent electric resistances (see Section 7.1.1) [661–663]. For instance, Nagaiah et al. designed a high-temperature heat flux sensor for gas turbine engines using polymer-derived SiCN ceramics. This novel sensor possesses a temperature coefficient of resistance of 4000 ppm/°C and is found to perform quite satisfactorily at 1400 °C for a long time as compared to conventional heat flux sensors [661]. Ren et al., characterized variation of dielectric constant and loss tangent of a SiCN ceramic as a function of temperature. They found that the dielectric constant of the SiCN ceramic increases from 3.71 to 3.87, corresponding to a temperature range between 50 and 500 °C [112]. Based on this temperature-dependent dielectric behavior, the SiCN-based ceramics might be used as wireless passive temperature sensors in high-temperature applications [112,525,664,665].

In addition, the PDCs were also proven recently to be suitable materials for sensing gases, such as NO_2 [109,111,666,667], H_2 [110,666] and NH_3 [667]. Karakuscu et al., for the first time, reported the gas sensing behavior of aerogel-derived silicon oxycarbide (SiOC) glasses in 2013. The mesoporous SiOC with a specific surface area of 150 m^2/g possesses good sensing ability to NO_2 (5 ppm) in a temperature range from 300 to 400 °C. At higher temperatures, the NO_2 response disappears, whereas the investigated SiOC samples start to sense hydrogen, and the optimum sensitivity is obtained at 500 °C. Importantly, the SiOC sensor is very selective. It can sense NO_2 and H_2 in the presence of other gases such as acetone or CO, even with rather high concentrations. At low temperatures (< 300 °C), nevertheless, the values are not reliable because the conductivity of the SiOC glasses is very low [666]. However, the following up study suggests that increasing the porosity and carbon content of the SiOC ceramics in the structure can result in high electrical conductivity and a shift of NO_2 sensing ability to room temperature [111]. Vakifahmetoglu et al. also claimed that the HF-etched SiOC ceramics (leaving with porous carbonaceous matrix) with a specific surface area of 310 m^2/g can be used to detect NO_2

Table 5
Overview of various SiOC and SiCN compounds and their electrochemical characteristics. The free carbon content, first-cycle reversible capacity (C_{rev}), irreversible capacity (C_{irr}) and coulombic efficiency (η) as well as cycling current and if available capacity retention upon continuous cycling are listed (n.d. = not determined) [697].

Samples	Free carbon [wt.%]	C_{rev} [mAh/g]	C_{irr} [mAh/g]	η [%]	Cycling current [mA/g]	Capacity retention	Ref.
$SiO_{1.5}C_{3.9}$	44.3	640	340	65	14.8	n.d.	[698]
$SiO_{0.51}C_{7.78}$	65.2	608	259	70	32.7	95% after 40 cycles	[561]
$SiO_{0.29}C_{5.07}$	54.1	520	272	72	32.7	n.d.	[101]
$SiO_{1.56}C_{7.36}$	64.3	580	267	68	32.7	93% after 40 cycles	[573]
$SiO_{2.78}C_{13.1}$	70.5	469	266	64	32.7	86% after 40 cycles	[699]
$SiO_{0.85}C_{1.99}$	25.9	794	370	68	100	n.d.	[562]
$SiO_{0.90}C_{4.40}$	48.5	568	330	63	18	cycling stable	[569]
$SiO_{0.98}C_{2.47}$	32.0	605	325	65	18	cycling stable	[578]
$SiO_{1.59}C_{3.36}$	43	600	680	47	360	cycling stable	[577]
$SiO_{1.18}C_{5.52}$	54.2	504.3	287.1	63.7	37	68.8% after 60 cycles	[567]
$SiO_{0.95}C_{3.72}$	43.6	535.9	335.8	61.5	37	56.0% after 60 cycles	[567]
$SiO_{1.01}C_{2.93}$	36.8	434.3	273.8	61.3	37	58.7% after 60 cycles	[567]
$SiO_{0.93}C_{2.26}$	29.5	501.4	302.7	62.3	37	47.3% after 60 cycles	[567]
$SiO_{0.87}C_{1.62}$	20.6	682.5	495.8	57.9	37	13.5% after 60 cycles	[567]
$SiO_{1.00}C_{1.05}$	11.6	706.1	375.5	65.3	37	5.2% after 60 cycles	[567]
$SiO_{1.40}C_{0.70}$	8.1	500.7	754.6	39. 9	37	1.5% after 60 cycles	[567]
$SiC_{5.35}N_{0.98}O_{0.19}$	57.04	383	172	69	18	cycling stable	[200]
$SiC_{3.70}N_{0.69}O_{0.62}$	46.02	241	291	45	18	cycling stable	[199]
$SiO_{0.06}C_{1.54}N_{0.74}$	23.2	69	67	50.6	18.6	127.5% after 114 cycles	[587]
$SiO_{0.05}C_{2.22}N_{0.84}$	33.4	278	199	58.3	18.6	112.9% after 114 cycles	[587]
$SiO_{0.10}C_{4.04}N_{0.69}$	49.3	374	227	60.5	18.6	115.9% after 114 cycles	[587]
$SiC_{3.90}O_{0.10}N_{0.80}$	48	703	375	65	18	89% after 134 cycles	[570]
$SiC_{10.59}O_{1.56}N_{0.21}$	69.1	570	367	61	18	cycling stable	[565]
$SiC_{3.70}O_{0.10}N_{1.30}H_{0.90}$	48.1	674	525	56	18.6	68% after 134 cycles	[99]
$SiC_{5.30}O_{0.30}N_{1.20}H_{0.20}$	56.0	282	224	56	18.6	109% after 134 cycles	[99]

gas at room temperature with an easy-to-read conductance (mS range), fast response kinetics (5 min) and a complete signal recovery due to the enhanced electrical conductivity and porosity [109]. Furthermore, the amorphous SiCN-based ceramics have also been demonstrated to be suitable for H_2 sensing at high temperatures up to 500 °C based on their semiconducting behavior. The thinner SiCN ceramic layer exhibits higher sensitivity to measure resistivity with adsorbing hydrogen molecules [110]. The sensing performance of the PDCs is significantly affected by the presence of free carbon because their sensing behavior is based on piezoresistive properties, electrical conductivity, semiconducting behavior or dielectric properties, which are highly influenced by free carbon (see Section 7). The concentration, structural ordering and the morphology of free carbon strongly affect the sensitivity and selectivity of the sensors. Therefore, the role of free carbon on the sensing behavior of the PDCs should be an interesting research topic which is worth of systematical future investigation.

8.2.2. Energy and environmental applications

PDCs for energy and environmental applications have been investigated for several years, such as anode materials for lithium ion batteries, electrochemical catalyst for water splitting [668], photocatalysts for degradation of pollutants in water [103,425], porous Si_3N_4 for CO_2 capture [669], and SiC_f/SiC composite for fusion energy applications [670,671]. Herein, we mainly focus on the SiCN- and SiOC-based anode materials for lithium ion batteries, which are highly related to the free carbon (see Section 7.2).

During the past 20 years, numerous studies from the research teams of Dahn [558,579,672,673], Riedel [568,575,577,674], Raj [524,560,562,571], Kanamura [561], Soraru [37,574,578], Li [559] and Singh [564] have been reported. The performance of selected PDC materials used as anode materials are summarized in Table 5, which suggests that both SiCN- and SiOC-based ceramics are promising candidates for anode materials of lithium ion batteries. The fundamental investigations concerning the effects of free carbon on the electrochemical performance of the PDC anode materials have been reviewed in Section 5.2, showing that the free carbon plays a crucial role in the high reversible capacity, good rate capability as well as reliable cycling stability of the anode materials [572].

8.2.3. Electromagnetic (EM) wave absorbing and shielding applications

Based on excellent thermomechanical properties and tunable dielectric properties as introduced in Sections 6.1 and 7.3, respectively, the PDCs are promising EM absorbing or shielding materials, particularly suitable for that used in harsh environments (*i.e.*, in corrosive/oxidizing media or at high temperatures) and/or under high mechanical load [368]. The role of free carbon in the EM absorbing or shielding performance of the PDCs is based on the dielectric properties of the materials as discussed in Section 7.3. The free carbon acting as a dielectric loss phase can enhance both the real (ε') and imaginary (ε'') permittivity of the PDCs. When the ε' is in the range of 5–20, the increase of free carbon content and structural ordering will lead to the enhancement of dielectric loss ($\varepsilon''/\varepsilon'$),

Table 6
Reported examples of Si-containing EM absorbing materials fabricated in PDC route (EAB = Effective Absorption Bandwidth).

Samples	Matrix	Dielectric loss phase	Optimum thickness [mm]	RL_{min} [dB]	EAB* [GHz]	Ref.
Porous SiC	SiC	Segregated carbon	2.75	−10.8	2.6	[197]
SiC/C	SiC	Carbon nanowires	2.85	−21	3.2	[607]
Porous Si_3N_4/SiC	Si_3N_4	SiC	3.35	−53	3.0	[198]
SiBCN/SiC	Amorphous SiBCN	SiC-nanocrystals	2.31	−16.2	3.6	[42]
SiOC/SiC-nanowire	a-SiOC	SiC-nanowires	3.3	−20.0	1.8	[595]
SiCNO aerogel	SiCNO	Free carbon	3	−42.5	6.6	[86]
Carbon-rich SiCN	amorphous SiCN	Free carbon	2.3	−59.59	4.2	[85]
Carbon-rich SiBCN	Amorphous SiBCN	Free carbon	3.08	−71.80	3.65	[700]
SiOC	Amorphous SiOC	Turbostratic carbon	2.64	− 46	3.2	[603]
RGO-SiCN	Amorphous SiCN	Reduced graphene oxide (RGO)	2.10	−62.1	3.0	[229]
1D carbon/SiC nanocomposites	SiC	Free carbon	1.9	−57.8	7.3	[612]

which can improve the EM absorbing performance. If the ε' of the PDCs is improved to be higher than 20, the PDCs will switch into EM shielding materials due to the high impedance mismatch [229,607,609]. An increased amount of free carbon and structural ordering result in enhanced total shielding effectiveness (SE_T) in terms of both absorption shielding effectiveness (SE_A) and reflection shielding effectiveness (SE_R) [87,607,609,610,675].

8.2.3.1. Electromagnetic (EM) wave absorbing materials. The fabrication of EM absorbing materials from preceramic precursors is a new technology, emerging in recent 10 years. Basically, the EM absorbing performance of a material is evaluated by reflection loss (RL) values. According to the transmission-line theory, the RL value (in dB) of a single layer of absorber backed by a PEC (perfect electric conductor) can be calculated by the following equation:

$$RL = 20\log_{10}\left|\frac{\sqrt{\frac{\mu}{\varepsilon}}\tanh\left(j\frac{2\pi fd}{c}\sqrt{\mu\varepsilon}\right)-1}{\sqrt{\frac{\mu}{\varepsilon}}\tanh\left(j\frac{2\pi fd}{c}\sqrt{\mu\varepsilon}\right)+1}\right| \tag{8.1}$$

where d, μ ($\mu = \mu' - j\mu''$) and ε ($\varepsilon = \varepsilon' - j\varepsilon''$) denote the thickness, complex permeability and complex permittivity of the absorber, respectively; c is the speed of light in the free space and f is the frequency of the incident electromagnetic wave. The terms ε' and μ' are the real parts of the complex permittivity and complex permeability, and the terms ε'' and μ'' represent the imaginary parts of the complex permittivity and complex permeability, respectively [676–679]. The calculated RL value is always negative. Thus, a lower RL value indicates a better EM absorbing performance. Generally, an effective EM material should be able to attenuate at least 90% of the electromagnetic wave, *i.e.*, the RL should be lower than −10 dB. At RL < −20 dB, more than 99% of the waves are attenuated, and the material is said to have excellent EM absorbing capability [680].

As shown in Table 6, PDCs have been applied so far for the fabrication of several EM absorbing materials with excellent performance, and most of the dielectric loss phase is free carbon. The PDC-based EM absorbing materials have numerous advantages if compared with other materials. For instance, *(i)* PDC-based composite EM absorbing materials possess amorphous ceramic matrix exhibiting a low real part of the permittivity (ε'), which is preferable for impedance matching; *(ii)* it is easy to homogeneously embed the dielectric loss phase within the ceramic matrix by either *in situ* formation [42] or blending [594]; *(iii)* the ceramic matrix with high melting point, excellent thermal and chemical stability as well as excellent resistance against decomposition and crystallization is especially useful for application in harsh environments [176,245]; *(iv)* due to the polymeric feature of the preceramic precursors, they can be subjected to a large variety of different shaping techniques to fabricate EM absorbing materials with various shapes (*e.g.*, monoliths, coatings, fibers and porous parts) [681].

8.2.3.2. Electromagnetic shielding materials. As mentioned above, the PDCs and composites with high complex permittivity (*i.e.*, $\varepsilon' > 20$ and $\varepsilon'' > 10$) can be used as EM shielding materials [604,682]. Generally, the intrinsic complex permittivity of the PDCs are not high enough for EM shielding applications. In recent years, polymer-derived ceramic (nano)composites with conductive fillers (*e.g.*, CNTs, Reduced graphene oxide, Ti_3SiC_2) as a secondary phase enable the possibility of fabricating the state of the art EM shielding materials [84,229,610]. The *in situ* precipitated segregated carbon ribbons with high aspect ratio and electrical conductivity are good for the enhancement of the overall electrical conductivity [423,607].

The EM shielding performance of a material is assessed by the shielding effectiveness (SE) which is defined as the ratio of the power of the incident EM wave to the transmitted EM wave. For a transverse EM wave propagating into materials with negligible magnetic interaction, the SE value of the materials is expressed by the following equation in units of decibel (dB) [84,683–685]:

$$SE = 10Log_{10}\left(\frac{1}{|S_{ij}|^2}\right) \tag{8.2}$$

where S_{ij} represents the power transmitting from the testing port i to port j. In general, when an EM wave is propagating into a shielding material, the incident power can be divided into the reflected power (R), absorbed power (A) and transmitted power (T). Using the scattering parameters (*i.e.*, S_{ij}) measured by a vector network analyzer, the total shielding effectiveness (SE_T), absorption

Table 7
Reported examples of Si-containing EM shielding materials produced via the PDC route.

Samples	Matrix	Dielectric loss phase	Thickness [mm]	Frequency [GHz)]	SE_T [dB] [a]	Ref.
SiC/C	SiC	Fee carbon	2	8.2–12.4	21.5	[685]
SiC/HfC_xN_{1-x}/C	SiC	HfC_xN_{1-x} and free carbon	2	8.2–12.4	42.1	
SiC_f/SiC-Ti_3SiC_2	SiC	Ti_3SiC_2 and excess carbon	3	8.2–12.4	45	[610]
SiC/C composite	SiC	Free carbon	3.2	8.2–12.4	36	[607]
SiC_f/SiCN composites	SiCN	Free carbon	3	8.2–12.4	25	[609]
SiC_f/SiC composites	SiC	Free carbon and PyC	3	8.2–12.4	30	[688]
RGO/CNTs-SiCN nanocomposite	SiCN	Reduced graphene oxide and CNTs	2	8.2–12.4	67.2	[84]
SiC/C nanocomposites	SiC	Free carbon	2.8	12.4–18	36.8	[675]
Si_3N_4-SiOC composites	Porous Si_3N_4	SiC nanowires and free carbon	2	8.2–12.4	35	[689]
RGO-SiCN nanocomposite	SiCN	Reduced graphene oxide	2	8.2–12.4	41.2	[229]

[a] The SET valves are recorded at room temperature.

shielding effectiveness (SE_A), reflection shielding effectiveness (SE_R), R, T and A can be calculated using the following equations [84,683,684]:

$$SE_R = -10Log_{10}(1 - R) \tag{8.3}$$

$$SE_A = -10Log_{10}(\frac{T}{1 - R}) \tag{8.4}$$

$$SE_T = SE_A + SE_R = -10Log_{10}(T) \tag{8.5}$$

$$R = |S_{11}|^2 = |S_{22}|^2 \tag{8.6}$$

$$T = |S_{12}|^2 = |S_{21}|^2 \tag{8.7}$$

$$A = 1 - R - T \tag{8.8}$$

According to the shielding theory, the higher the SE_T value in dB, the less EM wave passes through the shielding materials [686]. Generally, the SE_T value of a commercially used EMI shielding material should be higher than 20 dB at the frequency of interest [687].

Up to now, a few polymer-derived ceramic composites or nanocomposites (PDC-NCs) with enhanced permittivity and shielding effectiveness (SE) have been developed (see Table 7). The results reveal that the presence of free carbon significantly enhances the EM shielding performance of the PDCs [607,609,610,675,688,689].

9. Conclusions and outlook

PDCs as a class of advanced materials with exciting structural and functional properties have received increasing attention in the scientific community of materials science in the past 50 years. Their amorphous and crystallized states are characterized by interconnected nanodomain architectures and multiphase polycrystalline nano/microstructures, respectively, which dominate their structural and functional properties as well as the resultant applications. The *in situ* formed free carbon as the most outstanding feature of PDCs plays a crucial role in their unique microstructure and structural evolution in terms of phase separation, crystallization and decomposition. In particular, the free carbon phase is essential for versatile functional and thermomechanical properties. Within the past decades, remarkable preparative progress was made with respect to accessing interesting chemical and phase compositions based on a Si-based ceramic matrix and homogeneously distributed free carbon. The status of free carbon in the PDCs in terms of concentration, distribution, morphology and crystallinity can be effectively controlled via tuning the molecular structure of the preceramic polymers as well as managing the thermal-treatment process including maximum heating temperatures, holding time, protective atmosphere and pressure. By means of various advanced characterization techniques, the structural evolution of the *in situ* formed free carbon with increasing preparation temperature has been intensively studied and can be summarized via the following four steps: *(1)* precipitation of hydrogenated amorphous excess carbon via decomposition of aromatic hydrocarbons (600–800 °C); *(2)* nucleation of basic structural units (BSU) (800–1000 °C); *(3)* growth of turbostratic free carbon clusters via edge-to-edge linkage of BSUs (1000–1200 °C); *(4)* graphitization of the free carbon network or nanodomains (> 1400 °C). Depending on the different molecular structure and elemental composition of the preceramic polymers, the onset temperature of the four steps varies to some extent.

Based on the versatile structural and functional properties, multiple future potential applications of PDCs have been evaluated. Polymer-derived high temperature resistant Si-based ceramic fibres are already on the market for a couple of decades. Glow plugs for Diesel engines and motorbike brakes based on PDCs were successfully developed and were close to be commercialized. Moreover, there are numerous PDCs with the potential of “flowing out of the Laboratory and into the Markets” (Starfire systems, Inc., USA), such as ceramic coatings, foams, aerogels, joining materials, pressure/temperature/chemical sensors, electrode materials, electromagnetic absorbing and shielding materials, photo- and electrochemical catalysts, adsorbents, liquid/gas separators, photoluminescent materials, biomedical components and microelectromechanical systems (MEMS). Each application is a complicated combination of

several properties of PDCs, which are more or less affected by the presence of free carbon. Some of the relations have been widely studied (*e.g.*, the role of free carbon in electrical properties and lithium ion storages), whereas others still need future investigations, for instance, the influence of the free carbon on biocompatibility, fracture toughness, thermal shock resistance, tribological properties, corrosion resistance, thermoelectric property, electrochemical catalytic activity as well as high-temperature electric and dielectric properties of PDCs. In recent years, several new advancements have been achieved in the field of PDCs, including the development of multi-element SiMCON-based ceramics and ceramic nanocomposites (M = metal or semimetal) with further interesting materials properties. Additive manufacturing of PDC-based complex-shaped ceramic parts with complex composition is *e.g.* presently a hot-topic on international materials related conferences. These and other advances open a variety of new avenues regarding basic and applied research in the exciting field of polymer-derived ceramics.

Declaration of Competing Interest

The authors declare that they have no known competing financial interests or personal relationships that could have appeared to influence the work reported in this paper.

Acknowledgements

Qingbo Wen thanks the Profile Area of Technische Universität Darmstadt “From Material to Product Innovation (PMP)” and the “Career Bridging Grant” for financial support. Zhaoju Yu thanks the National Natural Science Foundation of China (No 51872246) and the Alexander von Humboldt Foundation for financial support. Ralf Riedel acknowledges the long-term financial support by the German Research Foundation (DFG, Bonn, Germany) via a variety of funded individual projects in the past 25 years including the DFG-Priority programs “NanoMat” (DFG-SPP-1181) and “WeNDeLIB” (DFG-SPP-1473) as well as the Collaborative Research Centre “Electric Fatigue in Functional Materials” (DFG-SFB 595).

References

[1] Peuckert M, Vaahs T, Brück M. Ceramics from organometallic polymers. Adv Mater 1990;2:398–404.
[2] Ainger F, Herbert J. The preparation of phosphorus-nitrogen compounds as non-porous solids. Special Ceram 1960:168–82.
[3] Chantrell P, Popper P. Inorganic polymers and ceramics. Special Ceram 1965;67.
[4] Verbeek W. Production of shaped articles of homogeneous mixtures of silicon carbide and nitride. Google Patents; 1974.
[5] Verbeek W, Winter G. Formkoerper aus siliciumcarbid und verfahren zu ihrer herstellung. DE Patent. 1974;2236078:A1.
[6] Winter G, Verbeek W, Mansmann M. Production of shaped articles of silicon carbide and silicon nitride. Google Patents; 1975.
[7] Yajima S, Hayashi J, Omori M. Continuous silicon carbide fiber of high tensile strength. Chem Lett 1975;4:931–4.
[8] Yajima S, Hayashi J, Omori M, Okamura K. Development of a silicon carbide fibre with high tensile strength. Nature 1976;261:683.
[9] Yajima S, Okamura K, Hayashi J, Omori M. Synthesis of continuous SiC fibers with high tensile strength. J Am Ceram Soc 1976;59:324–7.
[10] Yajima S, Omori M, Hayashi J, Okamura K, Matsuzawa T. Liaw C-f. Simple synthesis of the continuous SiC fiber with high tensile strength. Chem Lett 1976;5:551–4.
[11] Takamizawa M, Kobayashi T, Hayashida A, Takeda Y. Organoborosilicon polymer and a method for the preparation thereof. Google Patents; 1985.
[12] Takamizawa M, Kobayashi T, Hayashida A, Takeda Y. Method for the preparation of an inorganic fiber containing silicon, carbon, boron and nitrogen. Google Patents; 1986.
[13] Greil P. Polymer derived engineering ceramics. Adv Eng Mater 2000;2:339–48.
[14] Riedel R, Kienzle A, Dressler W, Ruwisch L, Bill J, Aldinger F. A silicoboron carbonitride ceramic stable to 2,000 C. Nature 1996;382:796.
[15] Riedel R, Passing G, Schönfelder H, Brook R. Synthesis of dense silicon-based ceramics at low temperatures. Nature 1992;355:714.
[16] Riedel R, Kleebe H-J, Schönfelder H, Aldinger F. A covalent micro/nano-composite resistant to high-temperature oxidation. Nature 1995;374:526–8.
[17] Funayama O, Nakahara H, Okoda M, Okumura M, Isoda T. Conversion mechanism of polyborosilazane into silicon nitride-based ceramics. J Mater Sci 1995;30:410–6.
[18] Colombo P, Mera G, Riedel R, Soraru GD. Polymer-derived ceramics: 40 years of research and innovation in advanced ceramics. J Am Ceram Soc. 2010;93:1805–37.
[19] Blum YD, Platz RM, Crawford EJ. Glass strengthening by polymer-derived ceramic coatings. J Am Ceram Soc 1990;73:170–2.
[20] Torrey JD, Bordia RK. Processing of polymer-derived ceramic composite coatings on steel. J Am Ceram Soc 2008;91:41–5.
[21] Günthner M, Schütz A, Glatzel U, Wang K, Bordia RK, Greißl O, et al. High performance environmental barrier coatings, Part I: Passive filler loaded SiCN system for steel. J Eur Ceram Soc 2011;31:3003–10.
[22] Park CH, Joo YJ, Chung JK, Han YH, Kim CJ. Morphology control of a silicon nitride thick film derived from polysilazane precursor using UV curing and IR heat treatment. Adv Appl Ceram 2017;116:376–82.
[23] Yajima S, Hasegawa Y, Okamura K, Matsuzawa T. Development of high tensile strength silicon carbide fibre using an organosilicon polymer precursor; 1978.
[24] Chawla N, Tur YK, Holmes JW, Barber JR, Szweda A. High-frequency fatigue behavior of woven-fiber-fabric-reinforced polymer-derived ceramic-matrix composites. J Am Ceram Soc 1998;81:1221–30.
[25] Jones R, Szweda A, Petrak D. Polymer derived ceramic matrix composites. Compos Part A Appl Sci Manuf 1999;30:569–75.
[26] Klatt E, Frass A, Frieß M, Koch D, Voggenreiter H. Mechanical and microstructural characterisation of SiC- and SiBNC-fibre reinforced CMCs manufactured via PIP method before and after exposure to air. J Eur Ceram Soc 2012;32:3861–74.
[27] Poerschke DL, Braithwaite A, Park D, Lauten F. Crystallization behavior of polymer-derived Si-OC for ceramic matrix composite processing. Acta Mater 2018;147:329–41.
[28] Riedel R, Seher M, Mayer J, Szabó DV. Polymer-derived Si-based bulk ceramics, part I: Preparation, processing and properties. J Eur Ceram Soc 1995;15:703–15.
[29] Kaur S, Mera G, Riedel R, Ionescu E. Effect of boron incorporation on the phase composition and high-temperature behavior of polymer-derived silicon carbide. J Eur Ceram Soc 2016;36:967–77.
[30] Riedel R, Greiner A, Miehe G, Dressler W, Fuess H, Bill J, et al. The first crystalline solids in the ternary Si-C-N system. Angew Chem Int Ed 1997;36:603–6.
[31] Mera G, Navrotsky A, Sen S, Kleebe H-J, Riedel R. Polymer-derived SiCN and SiOC ceramics–structure and energetics at the nanoscale. J Mater Chem A 2013;1:3826–36.
[32] Pham TA, Kim DP, Lim TW, Park SH, Yang DY, Lee KS. Three-dimensional SiCN ceramic microstructures via nano-stereolithography of inorganic polymer photoresists. Adv Funct Mater 2006;16:1235–41.

[33] Kolb R, Fasel C, Liebau-Kunzmann V, Riedel R. SiCN/C-ceramic composite as anode material for lithium ion batteries. J Eur Ceram Soc 2006;26:3903–8.
[34] Nghiem QD, Kim D, Kim DP. Synthesis of inorganic–organic diblock copolymers as a precursor of ordered mesoporous SiCN ceramic. Adv Mater 2007;19:2351–4.
[35] Sorarù GD, Pederiva L, Latournerie J, Raj R. Pyrolysis kinetics for the conversion of a polymer into an amorphous silicon oxycarbide ceramic. J Am Ceram Soc 2002;85:2181–7.
[36] Pena-Alonso R, Mariotto G, Gervais C, Babonneau F, Soraru GD. New insights on the high-temperature nanostructure evolution of SiOC and B-doped SiBOC polymer-derived glasses. Chem Mater 2007;19:5694–702.
[37] Dibandjo P, Graczyk-Zajac M, Riedel R, Pradeep V, Soraru G. Lithium insertion into dense and porous carbon-rich polymer-derived SiOC ceramics. J Eur Ceram Soc 2012;32:2495–503.
[38] Naviroj M, Miller S, Colombo P, Faber K. Directionally aligned macroporous SiOC via freeze casting of preceramic polymers. J Eur Ceram Soc 2015;35:2225–32.
[39] Vakifahmetoglu C, Colombo P. A direct method for the fabrication of macro-porous SiOC ceramics from preceramic polymers. Adv Eng Mater 2008;10:256–9.
[40] Bernard S, Weinmann M, Cornu D, Miele P, Aldinger F. Preparation of high-temperature stable SiBCN fibers from tailored single source polyborosilazanes. J Eur Ceram Soc 2005;25:251–6.
[41] Gao Y, Mera G, Nguyen H, Morita K, Kleebe H-J, Riedel R. Processing route dramatically influencing the nanostructure of carbon-rich SiCN and SiBCN polymer-derived ceramics. Part I: Low temperature thermal transformation. J Eur Ceram Soc 2012;32:1857–66.
[42] Ye F, Zhang L, Yin X, Zhang Y, Kong L, Li Q, et al. Dielectric and EMW absorbing properties of PDCs-SiBCN annealed at different temperatures. J Eur Ceram Soc 2013;33:1469–77.
[43] Cinibulk MK, Parthasarathy TA. Characterization of oxidized polymer-derived SiBCN fibers. J Am Ceram Soc 2001;84:2197–202.
[44] Schiavon MA, Armelin NA, Yoshida IVP. Novel poly (borosiloxane) precursors to amorphous SiBCO ceramics. Mater Chem Phys 2008;112:1047–54.
[45] Liebau V, Hauser R, Riedel R. Amorphous SiBCO ceramics derived from novel polymeric precursors. C R Chim 2004;7:463–9.
[46] Liao N, Xue W, Zhou H, Zhang M. Molecular dynamics investigation of structure and high-temperature mechanical properties of SiBCO ceramics. J Alloys Compd 2014;610:45–9.
[47] Chelliah NM, Singh H, Raj R, Surappa M. Processing, microstructural evolution and strength properties of in-situ magnesium matrix composites containing nano-sized polymer derived SiCNO particles. Mater Sci Eng: A 2017;685:429–38.
[48] Terauds K, Sanchez-Jimenez P, Raj R, Vakifahmetoglu C, Colombo P. Giant piezoresistivity of polymer-derived ceramics at high temperatures. J Eur Ceram Soc 2010;30:2203–7.
[49] Chelliah NM, Padaikathan P, Surappa M. Deformation mechanisms and texture evolution of in-situ magnesium matrix composites containing polymer derived SiCNO dispersoids during hot compression. Mater Sci Eng: A 2018;720:49–59.
[50] Duan RG, Mukherjee AK. Synthesis of SiCNO nanowires through heat-treatment of polymer-functionalized single-walled carbon nanotubes. Adv Mater 2004;16:1106–9.
[51] Wang Y, Fan Y, Zhang L, Zhang W, An L. Polymer-derived SiAlCN ceramics resist oxidation at 1400 C. Scripta Mater 2006;55:295–7.
[52] Wang Y, Fei W, An L. Oxidation/corrosion of polymer-derived SiAlCN ceramics in water vapor. J Am Ceram Soc 2006;89:1079–82.
[53] Dhamne A, Xu W, Fookes BG, Fan Y, Zhang L, Burton S, et al. Polymer–ceramic conversion of liquid polyaluminasilazanes for SiAlCN ceramics. J Am Ceram Soc 2005;88:2415–9.
[54] Wang Y, An L, Fan Y, Zhang L, Burton S, Gan Z. Oxidation of polymer-derived SiAlCN ceramics. J Am Ceram Soc 2005;88:3075–80.
[55] Cao Y, Gao Y, Zhao R, An L. Coupling effect of temperature and stress on the electronic behavior of amorphous SiAlCO. J Am Ceram Soc 2016;99:1881–4.
[56] Cao Y, An L. Anomalous piezo-dielectricity of a polymer-derived amorphous silicoaluminum oxycarbide (SiAlCO). Ceram Int 2018;44:1467–70.
[57] Cao Y, Yang X, Zhao R, Chen Y, Li N, An L. Giant piezoresistivity in polymer-derived amorphous SiAlCO ceramics. J Mater Sci 2016;51:5646–50.
[58] Cao Y, Yang X, An L. Electric conductivity and microstructure evolution of polymer-derived SiAlCO ceramics. Ceram Int 2016;42:4033–8.
[59] Yuan J, Hapis S, Breitzke H, Xu Y, Fasel C, Kleebe H-J, et al. Single-source-precursor synthesis of hafnium-containing ultrahigh-temperature ceramic nano-composites (UHTC-NCs). Inorg Chem 2014;53:10443–55.
[60] Yuan J, Luan X, Riedel R, Ionescu E. Preparation and hydrothermal corrosion behavior of C_f/SiCN and C_f/SiHfBCN ceramic matrix composites. J Eur Ceram Soc 2015;35:3329–37.
[61] Luan X, Yuan J, Wang J, Tian M, Cheng L, Ionescu E, et al. Laser ablation behavior of C_f/SiHfBCN ceramic matrix composites. J Eur Ceram Soc 2016;36:3761–8.
[62] Yuan J, Galetz M, Luan X, Fasel C, Riedel R, Ionescu E. High-temperature oxidation behavior of polymer-derived SiHfBCN ceramic nanocomposites. J Eur Ceram Soc 2016;36:3021–8.
[63] Terauds K, Raj R, Kroll P. Ab inito and FTIR studies of HfSiCNO processed from the polymer route. J Am Ceram Soc 2014;97:742–9.
[64] Terauds K, Raj R. Limits to the stability of the amorphous nature of polymer-derived HfSiCNO compounds. J Am Ceram Soc 2013;96:2117–23.
[65] Terauds K, Marshall DB, Raj R. Oxidation of polymer-derived HfSiCNO up to 1600 °C. J Am Ceram Soc 2013;96:1278–84.
[66] Ionescu E, Papendorf B, Kleebe H-J, Breitzke H, Nonnenmacher K, Buntkowsky G, et al. Phase separation of a hafnium alkoxide-modified polysilazane upon polymer-to-ceramic transformation—a case study. J Eur Ceram Soc 2012;32:1873–81.
[67] Bill J, Aldinger F. Precursor-derived covalent ceramics. Adv Mater 1995;7:775–87.
[68] Okamura K, Shimoo T, Suzuya K, Suzuki K. SiC-based ceramic fibers prepared via organic-to-inorganic conversion process-a review. J Ceram Soc Jpn 2006;114:445–54.
[69] Bernard S, Weinmann M, Gerstel P, Miele P, Aldinger F. Boron-modified polysilazane as a novel single-source precursor for SiBCN ceramic fibers: synthesis, melt-spinning, curing and ceramic conversion. J Mater Chem 2005;15:289–99.
[70] Chen L, Zhang L, Cai Z, Yu Y, Gu H, Zhang L. Effects of oxidation curing and sintering additives on the formation of polymer-derived near-stoichiometric silicon carbide fibers. J Am Ceram Soc 2008;91:428–36.
[71] King D, Apostolov Z, Key T, Carney C, Cinibulk M. Novel processing approach to polymer-derived ceramic matrix composites. Int J Appl Ceram Tec 2018;15:399–408.
[72] Zhao H, Chen L, Luan X, Zhang X, Yun J, Xu T. Synthesis, pyrolysis of a novel liquid SiBCN ceramic precursor and its application in ceramic matrix composites. J Eur Ceram Soc 2017;37:1321–9.
[73] Wang K, Günthner M, Motz G, Bordia RK. High performance environmental barrier coatings, Part II: Active filler loaded SiOC system for superalloys. J Eur Ceram Soc 2011;31:3011–20.
[74] Nguyen MD, Bang JW, Bin AS, Kim S-R, Kim Y, Hwang KH, et al. Novel polymer-derived ceramic environmental barrier coating system for carbon steel in oxidizing environments. J Eur Ceram Soc 2017;37:2001–10.
[75] Wang K, Unger J, Torrey JD, Flinn BD, Bordia RK. Corrosion resistant polymer derived ceramic composite environmental barrier coatings. J Eur Ceram Soc 2014;34:3597–606.
[76] Lewinsohn CA, Colombo P, Reimanis I, Ünal Ö. Stresses occurring during joining of ceramics using preceramic polymers. J Am Ceram Soc 2001;84:2240–4.
[77] Colombo P, Sglavo V, Pippel E, Woltersdorf J. Joining of reaction-bonded silicon carbide using a preceramic polymer. J Mater Sci 1998;33:2405–12.
[78] Vakifahmetoglu C, Zeydanli D, Colombo P. Porous polymer derived ceramics. Mater Sci Eng R-Rep 2016;106:1–30.
[79] Colombo P, Hellmann JR, Shelleman DL. Mechanical properties of silicon oxycarbide ceramic foams. J Am Ceram Soc 2001;84:2245–51.
[80] Takahashi T, Münstedt H, Modesti M, Colombo P. Oxidation resistant ceramic foam from a silicone preceramic polymer/polyurethane blend. J Eur Ceram Soc 2001;21:2821–8.
[81] Zeschky J, Höfner T, Arnold C, Weißmann R, Bahloul-Hourlier D, Scheffler M, et al. Polysilsesquioxane derived ceramic foams with gradient porosity. Acta Mater 2005;53:927–37.
[82] Riedel R, Mera G, Hauser R, Klonczynski A. Silicon-based polymer-derived ceramics: synthesis properties and applications-a review dedicated to Prof. Dr. Fritz Aldinger on the occasion of his 65th birthday. J Ceram Soc Jpn 2006;114:425–44.
[83] Ishikawa T, Kajii S, Matsunaga K, Hogami T, Kohtoku Y, Nagasawa T. A tough, thermally conductive silicon carbide composite with high strength up to 1600 °C

in air. Science 1998;282:1295–7.
[84] Liu X, Yu Z, Ishikawa R, Chen L, Liu X, Yin X, et al. Single-source-precursor derived RGO/CNTs-SiCN ceramic nanocomposite with ultra-high electromagnetic shielding effectiveness. Acta Mater 2017;130:83–93.
[85] Song Y, He L, Zhang X, Liu F, Tian N, Tang Y, et al. Highly efficient electromagnetic wave absorbing metal-free and carbon-rich ceramics derived from hyperbranched polycarbosilazanes. J Phys Chem C 2017;121:24774–85.
[86] Zhao W, Shao G, Jiang M, Zhao B, Wang H, Chen D, et al. Ultralight polymer-derived ceramic aerogels with wide bandwidth and effective electromagnetic absorption properties. J Eur Ceram Soc 2017;37:3973–80.
[87] Yin X, Kong L, Zhang L, Cheng L, Travitzky N, Greil P. Electromagnetic properties of Si–C–N based ceramics and composites. Int Mater Rev 2014;59:326–55.
[88] Liew L-A, Liu Y, Luo R, Cross T, An L, Bright VM, et al. Fabrication of SiCN MEMS by photopolymerization of pre-ceramic polymer. Sensor Actuat A-Phys 2002;95:120–34.
[89] Schulz M. Polymer derived ceramics in MEMS/NEMS–a review on production processes and application. Adv Appl Ceram 2009;108:454–60.
[90] Liew L-A, Saravanan R, Bright VM, Dunn ML, Daily JW, Raj R. Processing and characterization of silicon carbon-nitride ceramics: application of electrical properties towards MEMS thermal actuators. Sensor Actuat A-Phys 2003;103:171–81.
[91] Liu Y, Liew L-A, Luo R, An L, Dunn ML, Bright VM, et al. Application of microforging to SiCN MEMS fabrication. Sensor Actuat A-Phys 2002;95:143–51.
[92] Liew L-A, Bright VM, Raj R. A novel micro glow plug fabricated from polymer-derived ceramics: in situ measurement of high-temperature properties and application to ultrahigh-temperature ignition. Sensor Actuat A-Phys 2003;104:246–62.
[93] Harshe R, Balan C, Riedel R. Amorphous Si(Al)OC ceramic from polysiloxanes: bulk ceramic processing, crystallization behavior and applications. J Eur Ceram Soc 2004;24:3471–82.
[94] Ferraioli L, Ahn D, Saha A, Pavesi L, Raj R. Intensely photoluminescent pseudo-amorphous siliconoxycarbonitride polymer–ceramic hybrids. J Am Ceram Soc 2008;91:2422–4.
[95] Shimokawa Y, Fujiwara A, Ionescu E, Mera G, Honda S, Iwamoto Y, et al. Synthesis and characterization of luminescent properties of ceramics derived from polysilylcarbodiimides. J Ceram Soc Jpn 2014;122:895–901.
[96] Su R, Huang Z, Chen F, Shen Q, Zhang L. Synthesis and luminescent properties of ternary Si–Ge–N nanowires. CrystEngComm 2016;18:8787–93.
[97] Zhang Y, Quaranta A, Soraru GD. Synthesis and luminescent properties of novel Eu^{2+}-doped silicon oxycarbide glasses. Opt Mater 2004;24:601–5.
[98] Vrankovic D, Graczyk-Zajac M, Kalcher C, Rohrer J, Becker M, Stabler C, et al. Highly porous silicon embedded in a ceramic matrix: a stable high-capacity electrode for Li-ion batteries. ACS Nano 2017;11:11409–16.
[99] Reinold LM, Yamada Y, Graczyk-Zajac M, Munakata H, Kanamura K, Riedel R. The influence of the pyrolysis temperature on the electrochemical behavior of carbon-rich SiCN polymer-derived ceramics as anode materials in lithium-ion batteries. J Power Sources 2015;282:409–15.
[100] Kaspar J, Terzioglu C, Ionescu E, Graczyk-Zajac M, Hapis S, Kleebe HJ, et al. Stable SiOC/Sn nanocomposite anodes for lithium-ion batteries with outstanding cycling stability. Adv Funct Mater 2014;24:4097–104.
[101] Fukui H, Ohsuka H, Hino T, Kanamura K. Influence of polystyrene/phenyl substituents in precursors on microstructures of Si-O-C composite anodes for lithium-ion batteries. J Power Sources 2011;196:371–8.
[102] Dahn JR, Wilson AM, Xing W, Zank GA. Electrodes for lithium ion batteries using polysilazanes ceramic with lithium. Google Patents; 1997.
[103] Seifollahi Bazarjani M, Hojamberdiev M, Morita K, Zhu G, Cherkashinin G, Fasel C, et al. Visible light photocatalysis with c-WO_{3-x}/$WO_3 \times H_2O$ nanoheterostructures in situ formed in mesoporous polycarbosilane-siloxane polymer. J Am Chem Soc 2013;135:4467–75.
[104] Cross T, Raj R, Prasad SV, Buchheit TE, Tallant DR. Mechanical and tribological behavior of polymer-derived ceramics constituted from $SiC_xO_yN_z$. J Am Ceram Soc 2006;89:3706–14.
[105] Cross TJ, Raj R, Cross TJ, Prasad SV, Tallant DR. Synthesis and tribological behavior of silicon oxycarbonitride thin films derived from poly (urea) methyl vinyl silazane. Int J Appl Ceram Tec 2006;3:113–26.
[106] Klaffke D, Wäsche R, Janakiraman N, Aldinger F. Tribological characterisation of siliconcarbonitride ceramics derived from preceramic polymers. Wear 2006;260:711–9.
[107] Li Z, Cao Y, He J, Wang Y. Mechanical and tribological performances of C-SiC nanocomposites synthetized from polymer-derived ceramics sintered by spark plasma sintering. Ceram Int 2018;44:14335–41.
[108] Alvi SA, Akhtar F. High temperature tribology of polymer derived ceramic composite coatings. Sci Rep 2018;8:15105.
[109] Vakifahmetoglu C, Buldu M, Karakuscu A, Ponzoni A, Assefa D, Soraru GD. High surface area carbonous components from emulsion derived SiOC and their gas sensing behavior. J Eur Ceram Soc 2015;35:4447–52.
[110] Hu LH, Raj R. Semiconductive behavior of polymer-derived SiCN ceramics for hydrogen sensing. J Am Ceram Soc 2015;98:1052–5.
[111] Karakuscu A, Ponzoni A, Ayana D, Soraru G, Sberveglieri G. High carbon-high porous SiOC glasses for room temperature NO_2 sensing. Proc Eng 2014;87:160–3.
[112] Ren X, Ebadi S, Chen Y, An L, Gong X. High-temperature characterization of SiCN ceramics for wireless passive sensing applications up to 500 °C. In: WAMICON 2011 conference proceedings. IEEE; 2011. p. 1–5.
[113] Gonzalo-Juan I, Detsch R, Mathur S, Ionescu E, Boccaccini A, Riedel R. Synthesis and in vitro activity assessment of novel silicon oxycarbide-based bioactive glasses. Materials 2016;9:959.
[114] Ionescu E, Sen S, Mera G, Navrotsky A. Structure, energetics and bioactivity of silicon oxycarbide-based amorphous ceramics with highly connected networks. J Eur Ceram Soc 2018;38:1311–9.
[115] Gawęda M, Jeleń P, Długoń E, Wajda A, Leśniak M, Simka W, et al. Bioactive layers based on black glasses on titanium substrates. J Am Ceram Soc 2018;101:590–601.
[116] Stabler C, Ionescu E, Graczyk-Zajac M, Gonzalo-Juan I, Riedel R. Silicon oxycarbide glasses and glass-ceramics:"All-Rounder" materials for advanced structural and functional applications. J Am Ceram Soc 2018;101:4817–56.
[117] Bunsell AR, Piant A. A review of the development of three generations of small diameter silicon carbide fibres. J Mater Sci 2006;41:823–39.
[118] Kumar BM, Kim Y-W. Processing of polysiloxane-derived porous ceramics: a review. Sci Technol Adv Mat 2010;11:044303.
[119] Miele P, Bernard S, Cornu D, Toury B. Recent developments in polymer-derived ceramic fibers (PDCFs): preparation, properties and applications-a review. Soft Mater 2007;4:249–86.
[120] Ionescu E, Kleebe H-J, Riedel R. Silicon-containing polymer-derived ceramic nanocomposites (PDC-NCs): preparative approaches and properties. Chem Soc Rev 2012;41:5032–52.
[121] Yu Z, Yang L, Min H, Zhang P, Zhou C, Riedel R. Single-source-precursor synthesis of high temperature stable SiC/C/Fe nanocomposites from a processable hyperbranched polyferrocenylcarbosilane with high ceramic yield. J Mater Chem C 2014;2:1057–67.
[122] Ionescu E, Terzioglu C, Linck C, Kaspar J, Navrotsky A, Riedel R. Thermodynamic control of phase composition and crystallization of metal-modified silicon oxycarbides. J Am Ceram Soc 2013;96:1899–903.
[123] Colombo P. Engineering porosity in polymer-derived ceramics. J Eur Ceram Soc 2008;28:1389–95.
[124] Eckel ZC, Zhou C, Martin JH, Jacobsen AJ, Carter WB, Schaedler TA. Additive manufacturing of polymer-derived ceramics. Science 2016;351:58–62.
[125] Yang W, Gao F, Wang H, Zheng X, Xie Z, An L. Synthesis of ceramic nanocomposite powders with in situ formation of nanowires/nanobelts. J Am Ceram Soc 2008;91:1312–5.
[126] Brigo L, Schmidt JEM, Gandin A, Michieli N, Colombo P, Brusatin G. 3D nanofabrication of SiOC ceramic structures. Adv Sci 2018. 1800937.
[127] Lu K. Porous and high surface area silicon oxycarbide-based materials-a review. Mater Sci Eng R-Rep 2015;97:23–49.
[128] Lei Y-p, Song Y-c, Deng C. Novel processable precursor for BN by the polymer-derived ceramics route. Ceram Int 2011;37:3005–9.
[129] Cornu D, Bernard S, Duperrier S, Toury B, Miele P. Alkylaminoborazine-based precursors for the preparation of boron nitride fibers by the polymer-derived ceramics (PDCs) route. J Eur Ceram Soc 2005;25:111–21.
[130] Lei Y, Wang Y, Xue J, Song Y. Influence of pyrolysis conditions on fabrication of polymer-derived BN fiber for wave transparent application. Compos Part B Eng 2013;51:254–9.

[131] Salles V, Bernard S, Brioude A, Cornu D, Miele P. A new class of boron nitride fibers with tunable properties by combining an electrospinning process and the polymer-derived ceramics route. Nanoscale 2010;2:215–7.
[132] Gervais C, Maquet J, Babonneau F, Duriez C, Framery E, Vaultier M, et al. Chemically derived BN ceramics: extensive ^{11}B and ^{15}N solid-state NMR study of a preceramic polyborazilene. Chem Mater 2001;13:1700–7.
[133] Riedel R, Bill J, Passing G. A novel carbon material derived from pyridine-borane. Adv Mater 1991;3:551–2.
[134] Bhat S, Lauterbach S, Dzivenko D, Lathe C, Bayarjargal L, Schwarz M, et al. High-pressure high-temperature behavior of polymer derived amorphous BCN. J Phys Conf Ser: IOP Publishing 2014:182004.
[135] Bernard S, Miele P. Polymer-derived boron nitride: a review on the chemistry, shaping and ceramic conversion of borazine derivatives. Materials 2014;7:7436–59.
[136] Takahiro G, Hiroshi Y, Takaaki H, Kyoko BK, Yoshimoto A. Preparation of polyzirconoxane from zirconium oxychloride octahydrate and ethylene glycol as a precursor for zirconia ceramics. Appl Organomet Chem 2000;14:119–26.
[137] Li X, Hector AL, Owen JR, Shah SIU. Evaluation of nanocrystalline Sn_3N_4 derived from ammonolysis of $Sn(NEt_2)_4$ as a negative electrode material for Li-ion and Na-ion batteries. J Mater Chem A 2016;4:5081–7.
[138] Baxter DV, Chisholm MH, Gama GJ, DiStasi VF, Hector AL, Parkin IP. Molecular routes to metal carbides, nitrides, and oxides. 2. Studies of the ammonolysis of metal dialkylamides and hexamethyldisilylamides. Chem Mater 1996;8:1222–8.
[139] Kurokawa Y, Ishizaka T, Suzuki M. Preparation of refractory nitride fibers by thermal decomposition of transition metal (Ti, Nb) alkoxide-cellulose precursor gel fibers in NH_3 atmosphere. J Mater Sci 2001;36:301–6.
[140] Thorne K, Ting S, Chu C, Mackenzie J, Getman T, Hawthorne M. Synthesis of TiC via polymeric titanates: the preparation of fibres and thin films. J Mater Sci 1992;27:4406–14.
[141] Lang H, Seyferth D. Pyrolysis of metallocene complexes $(\eta C_5H_4R)_2MR$: An organometallic route to metal carbide (MC) materials (M= Ti, Zr, Hf). Appl Organomet Chem 1990;4:599–606.
[142] Preiss H, Schierhorn E, Brzezinka K-W. Synthesis of polymeric titanium and zirconium precursors and preparation of carbide fibres and films. J Mater Sci 1998;33:4697–706.
[143] Tao X, Qiu W, Li H, Zhao T. Synthesis of nanosized zirconium carbide from preceramic polymers by the facile one-pot reaction. Polym Adv Technol 2010;21:300–4.
[144] Tao X, Xiang Z, Zhou S, Zhu Y, Qiu W, Zhao T. Synthesis and characterization of a boron-containing precursor for ZrB2 ceramic; 2016.
[145] Tao X, Zhou S, Xiang Z, Ma J, Hou R, Zhu Y, et al. Fabrication of continuous ZrB_2 nanofibers derived from boron-containing polymeric precursors. J Alloys Compd 2017;697:318–25.
[146] Wang H, Chen X, Gao B, Wang J, Wang Y, Chen S, et al. Synthesis and characterization of a novel precursor-derived ZrC/ZrB_2 ultra-high-temperature ceramic composite. Appl Organomet Chem 2013;27:79–84.
[147] Inzenhofer K, Schmalz T, Wrackmeyer B, Motz G. The preparation of HfC/C ceramics via molecular design. Dalton T 2011;40:4741–5.
[148] Sun Y, Yang C, Lu Y, Chen F, Han W, Qiu W, et al. Transformation of metallic polymer precursor into nanosized HfTaC2 ceramics. Ceram Int 2019.
[149] Wynne KJ, Rice RW. Ceramics via polymer pyrolysisdagger. Annu Rev Mater Sci 1984;14:297–334.
[150] Laine RM, Babonneau F. Preceramic polymer routes to silicon carbide. Chem Mater 1993;5:260–79.
[151] Birot M, Pillot J-P, Dunogues J. Comprehensive chemistry of polycarbosilanes, polysilazanes, and polycarbosilazanes as precursors of ceramics. Chem Rev 1995;95:1443–77.
[152] Jaschke B, Klingebiel U, Riedel R, Na Doslik, Gadow R. Cyclosilazanes and borazines: polymer precursors to silicon-and boron-containing ceramics. Appl Organomet Chem 2000;14:671–85.
[153] Kroke E, Li Y-L, Konetschny C, Lecomte E, Fasel C, Riedel R. Silazane derived ceramics and related materials. Mater Sci Eng R-Rep 2000;26:97–199.
[154] Bernard S, Miele P. Ordered mesoporous polymer-derived ceramics and their processing into hierarchically porous boron nitride and silicoboron carbonitride monoliths. New J Chem 2014;38:1923–31.
[155] Hector AL. Synthesis and processing of silicon nitride and related materials using preceramic polymer and non-oxide sol-gel approaches. Coord Chem Rev 2016;323:120–37.
[156] Viard A, Fonblanc D, Lopez-Ferber D, Schmidt M, Lale A, Durif C, et al. Polymer derived Si-B-C-N ceramics: 30 years of research. Adv Eng Mater 2018;20:1800360.
[157] Francis A. Progress in polymer-derived functional silicon-based ceramic composites for biomedical and engineering applications. Mater Res Exp 2018;5:062003.
[158] Ionescu E, Mera G, Riedel R. Polymer-derived ceramics (PDCs): Materials design towards applications at ultrahigh-temperatures and in extreme environments. Nanotechnol: Concepts, Methodol, Tools, Appl: IGI Global 2014:1108–39.
[159] Riedel R, Ionescu E, Chen I-W. Modern trends in advanced ceramics. Ceram Sci Technol 2008;1:3–38.
[160] Ionescu E. Polymer-derived ceramics. Ceram Sci Technol 2013:457–500.
[161] Bernardo E, Fiocco L, Parcianello G, Storti E, Colombo P. Advanced ceramics from preceramic polymers modified at the nano-scale: a review. Materials 2014;7:1927–56.
[162] Ionescu E, Bernard S, Lucas R, Kroll P, Ushakov S, Navrotsky A, et al. Polymer-derived ultra-high temperature ceramics (UHTCs) and related materials. Adv Eng Mater 2019.
[163] Trassl S, Kleebe HJ, Störmer H, Motz G, Rössler E, Ziegler G. Characterization of the free-carbon phase in Si-C-N ceramics: Part II, comparison of different polysilazane precursors. J Am Ceram Soc 2002;85:1268–74.
[164] Chollon G, Pailler R, Canet R, Delhaes P. Correlation between microstructure and electrical properties of SiC-based fibres derived from organosilicon precursors. J Eur Ceram Soc 1998;18:725–33.
[165] Kleebe H-J, Gregori G, Babonneau F, Blum YD, MacQueen DB, Masse S. Evolution of C-rich SiOC ceramics: Part I. Characterization by integral spectroscopic techniques: Solid-state NMR and Raman spectroscopy: dedicated to Professor Dr. Fritz Aldinger on the occasion of his 65th birthday. Z Metallk 2006;97:699–709.
[166] Gregori G, Kleebe H-J, Blum YD, Babonneau F. Evolution of C-rich SiOC ceramics: Part II. Characterization by high lateral resolution techniques: electron energy-loss spectroscopy, high-resolution TEM and energy-filtered TEM: dedicated to Professor Dr. Fritz Aldinger on the occasion of his 65th birthday. Z Metallk 2006;97:710–20.
[167] Blum YD, MacQueen DB, Kleebe H-J. Synthesis and characterization of carbon-enriched silicon oxycarbides. J Eur Ceram Soc 2005;25:143–9.
[168] Oberlin A. High-resolution TEM studies of carbonization and graphitization. Chem Phys Carbon 1989;22.
[169] Monthioux M, Delverdier O. Thermal behavior of (organosilicon) polymer-derived ceramics. V: Main facts and trends. J Eur Ceram Soc 1996;16:721–37.
[170] Burns GT, Angelotti TP, Hanneman LF, Chandra G, Moore JA. Alkyl-and arylsilsesquiazanes: effect of the R group on polymer degradation and ceramic char composition. J Mater Sci 1987;22:2609–14.
[171] Schiavon MA, Soraru GD, Yoshida IVP. Synthesis of a polycyclic silazane network and its evolution to silicon carbonitride glass. J Non-Cryst Solids 2002;304:76–83.
[172] Riedel R, Passing G. Synthesis of dense silicon-based ceramics at low temperatures. Nature 1992;355:714.
[173] Laffon C, Flank A, Lagarde P, Laridjani M, Hagege R, Olry P, et al. Study of Nicalon-based ceramic fibres and powders by EXAFS spectrometry, X-ray diffractometry and some additional methods. J Mater Sci 1989;24:1503–12.
[174] Mutin PH. Control of the composition and structure of silicon oxycarbide and oxynitride glasses derived from polysiloxane precursors. J Sol-Gel Sci Technol 1999;14:27–38.
[175] Takeda M, Saeki A, Ji Sakamoto, Imai Y, Ichikawa H. Effect of hydrogen atmosphere on pyrolysis of cured polycarbosilane fibers. J Am Ceram Soc 2000;83:1063–9.

[176] Mera G, Riedel R, Poli F, Müller K. Carbon-rich SiCN ceramics derived from phenyl-containing poly (silylcarbodiimides). J Eur Ceram Soc 2009;29:2873–83.
[177] Burns GT, Taylor RB, Xu Y, Zangvil A, Zank GA. High-temperature chemistry of the conversion of siloxanes to silicon carbide. Chem Mater. 1992;4:1313–23.
[178] Turquat C, Kleebe HJ, Gregori G, Walter S, Sorarù GD. Transmission electron microscopy and electron energy-loss spectroscopy study of nonstoichiometric silicon-carbon-oxygen glasses. J Am Ceram Soc 2001;84:2189–96.
[179] Kleebe H-J, Blum YD. SiOC ceramic with high excess free carbon. J Eur Ceram Soc 2008;28:1037–42.
[180] Hurwitz F, Heimann P, Farmer S, Hembree D. Characterization of the pyrolytic conversion of polysilsesquioxanes to silicon oxycarbides. J Mater Sci 1993;28:6622–30.
[181] Bouillon E, Pailler R, Naslain R, Bacque E, Pillot J, Birot M, et al. New poly (carbosilane) models. 5. Pyrolysis of a series of functional poly (carbosilanes). Chem Mater 1991;3:356–67.
[182] Narisawa M, Funabiki F, Iwase A, Wakai F, Hosono H. Effects of atmospheric composition on the molecular structure of synthesized silicon oxycarbides. J Am Ceram Soc 2015;98:3373–80.
[183] Galusek D, Reschke S, Riedel R, Dreßler W, Šajgalík P, Lenčéš Z, et al. In-situ carbon content adjustment in polysilazane derived amorphous SiCN bulk ceramics. J Eur Ceram Soc 1999;19:1911–21.
[184] Sorarù GD, Modena S, Guadagnino E, Colombo P, Egan J, Pantano C. Chemical durability of silicon oxycarbide glasses. J Am Ceram Soc 2002;85:1529–36.
[185] Hörz M, Zern A, Berger F, Haug J, Müller K, Aldinger F, et al. Novel polysilazanes as precursors for silicon nitride/silicon carbide composites without “free” carbon. J Eur Ceram Soc 2005;25:99–110.
[186] Dibandjo P, Dirè S, Babonneau F, Soraru GD. New insights into the nanostructure of high-C SiOC glasses obtained via polymer pyrolysis. Glass Technol-Part A 2008;49:175–8.
[187] Hurwitz FI, Heiman P, Kacik T. Redistribution reactions in Blackglas™ during pyrolysis and their effect on oxidative stability. In: 19th annual conference on composites, advanced ceramics, materials, and structures-A. John Wiley & Sons; 2009. p. 217.
[188] Le Coustumer P, Monthioux M, Oberlin A. Understanding Nicalon® fibre. J Eur Ceram Soc 1993;11:95–103.
[189] Delverdier O, Monthioux M, Mocaer D, Pailler R. Thermal behavior of polymer-derived ceramics. I. Si-C and Si-CO systems from both commercial and new polycarbosilane (PCS) precursors. J Eur Ceram Soc 1993;12:27–41.
[190] Haluschka C, Engel C, Riedel R. Electrical properties of ternary Si-C-N ceramics. MRS Online Proceed Libra Arch 1996;435.
[191] Trassl S, Puchinger M, Rössler E, Ziegler G. Electrical properties of amorphous $SiC_xN_yH_z$-ceramics derived from polyvinylsilazane. J Eur Ceram Soc 2003;23:781–9.
[192] Wang Y, Jiang T, Zhang L, An L. Electron transport in polymer-derived amorphous silicon oxycarbonitride ceramics. J Am Ceram Soc 2009;92:1603–6.
[193] Li X, Wang Y. Complex impedance study on polymer-derived amorphous silicon carbonitride. Ceram Int 2017;43:13560–4.
[194] Kim KJ, Eom J-H, Kim Y-W, Seo W-S. Electrical conductivity of dense, bulk silicon-oxycarbide ceramics. J Eur Ceram Soc 2015;35:1355–60.
[195] Wang K, Ma B, Li X, Wang Y, An L. Effect of pyrolysis temperature on the structure and conduction of polymer-derived SiC. J Am Ceram Soc 2014;97:2135–8.
[196] Duan W, Yin X, Li Q, Schlier L, Greil P, Travitzky N. A review of absorption properties in silicon-based polymer derived ceramics. J Eur Ceram Soc 2016;36:3681–9.
[197] Li Q, Yin X, Duan W, Kong L, Hao B, Ye F. Electrical, dielectric and microwave-absorption properties of polymer derived SiC ceramics in X band. J Alloys Compd 2013;565:66–72.
[198] Li Q, Yin X, Duan W, Hao B, Kong L, Liu X. Dielectric and microwave absorption properties of polymer derived SiCN ceramics annealed in N_2 atmosphere. J Eur Ceram Soc 2014;34:589–98.
[199] Graczyk-Zajac M, Mera G, Kaspar J, Riedel R. Electrochemical studies of carbon-rich polymer-derived SiCN ceramics as anode materials for lithium-ion batteries. J Eur Ceram Soc 2010;30:3235–43.
[200] Kaspar J, Mera G, Nowak AP, Graczyk-Zajac M, Riedel R. Electrochemical study of lithium insertion into carbon-rich polymer-derived silicon carbonitride ceramics. Electrochim Acta 2010;56:174–82.
[201] Riedel R, Toma L, Janssen E, Nuffer J, Melz T, Hanselka H. Piezoresistive effect in SiOC ceramics for integrated pressure sensors. J Am Ceram Soc 2010;93:920–4.
[202] Zhang L, Wang Y, Wei Y, Xu W, Fang D, Zhai L, et al. A silicon carbonitride ceramic with anomalously high piezoresistivity. J Am Ceram Soc 2008;91:1346–9.
[203] Wang Y, Zhang L, Fan Y, Jiang D, An L. Stress-dependent piezoresistivity of tunneling-percolation systems. J Mater Sci 2009;44:2814–9.
[204] Biasetto L, Pena-Alonso R, Soraru G, Colombo P. Etching of SiOC ceramic foams. Adv Appl Ceram 2008;107:106–10.
[205] Mazo MA, Tamayo A, Rubio J. Advanced silicon oxycarbide-carbon composites for high temperature resistant friction systems. J Eur Ceram Soc 2016;36:2443–52.
[206] Papendorf B, Ionescu E, Kleebe HJ, Linck C, Guillon O, Nonnenmacher K, et al. High-temperature creep behavior of dense SiOC-based ceramic nanocomposites: microstructural and phase composition effects. J Am Ceram Soc 2013;96:272–80.
[207] Ionescu E, Balan C, Kleebe HJ, Müller MM, Guillon O, Schliephake D, et al. High-temperature creep behavior of SiOC glass-ceramics: influence of network carbon versus segregated carbon. J Am Ceram Soc 2014;97:3935–42.
[208] Stabler C, Roth F, Narisawa M, Schliephake D, Heilmaier M, Lauterbach S, et al. High-temperature creep behavior of a SiOC glass ceramic free of segregated carbon. J Eur Ceram Soc 2016;36:3747–53.
[209] Scarmi A, Sorarù GD, Raj R. The role of carbon in unexpected visco (an) elastic behavior of amorphous silicon oxycarbide above 1273 K. J Non-Cryst Solids 2005;351:2238–43.
[210] Viard A, Fonblanc D, Schmidt M, Lale A, Salameh C, Soleilhavoup A, et al. Molecular chemistry and engineering of boron-modified polyorganosilazanes as new processable and functional SiBCN precursors. Chem Eur J 2017;23:9076–90.
[211] Schuhmacher J, Weinmann M, Bill J, Aldinger F, Müller K. Solid-state NMR studies of the preparation of Si-C-N ceramics from polysilylcarbodiimide polymers. Chem Mater 1998;10:3913–22.
[212] Flores O, Bordia RK, Nestler D, Krenkel W, Motz G. Ceramic fibers based on SiC and SiCN systems: current research, development, and commercial status. Adv Eng Mater 2014;16:621–36.
[213] Guo A, Roso M, Modesti M, Liu J, Colombo P. Preceramic polymer-derived SiOC fibers by electrospinning. J Appl Polym Sci 2014;131.
[214] Barroso G, Li Q, Bordia RK, Motz G. Polymeric and ceramic silicon-based coatings-a review. J Mater Chem A 2018.
[215] Hernández-Rodríguez P, López-Honorato E. Polymer derived SiC environmental barrier coatings with superwetting properties. Ceram Int 2017;43:11289–95.
[216] Günthner M, Wang K, Bordia RK, Motz G. Conversion behaviour and resulting mechanical properties of polysilazane-based coatings. J Eur Ceram Soc 2012;32:1883–92.
[217] Liu J, Zhang L, Liu Q, Cheng L, Wang Y. Polymer-derived SiOC-barium-strontium aluminosilicate coatings as an environmental barrier for C/SiC composites. J Am Ceram Soc 2010;93:4148–52.
[218] Zhu Y, Huang Z, Dong S, Yuan M, Jiang D. Manufacturing 2D carbon-fiber-reinforced SiC matrix composites by slurry infiltration and PIP process. Ceram Int 2008;34:1201–5.
[219] Sato K, Tezuka A, Funayama O, Isoda T, Terada Y, Kato S, et al. Fabrication and pressure testing of a gas-turbine component manufactured by a preceramic-polymer-impregnation method. Compos Sci Technol 1999;59:853–9.
[220] Interrante L, Jacobs J, Sherwood W, Whitmarsh C. Fabrication and properties of fiber-and particulate-reinforced SiC matrix composites obtained with (A) HPCS as the matrix source. Key Eng Mater: Trans Tech Publ; 1997. p. 271–8.
[221] Yoon BH, Lee EJ, Kim HE, Koh YH. Highly aligned porous silicon carbide ceramics by freezing polycarbosilane/camphene solution. J Am Ceram Soc 2007;90:1753–9.
[222] Yoon BH, Park CS, Kim HE, Koh YH. In situ synthesis of porous silicon carbide (SiC) ceramics decorated with SiC nanowires. J Am Ceram Soc 2007;90:3759–66.
[223] Zhang H, Nunes PDA, Wilhelm M, Rezwan K. Hierarchically ordered micro/meso/macroporous polymer-derived ceramic monoliths fabricated by freeze-casting. J Eur Ceram Soc 2016;36:51–8.

[224] Hanemann T, Ade M, Börner M, Motz G, Schulz M, Haußelt J. Microstructuring of preceramic polymers. Adv Eng Mater 2002;4:869–73.
[225] Lee H-J, Yoon T-H, Kim D-P. Fabrication of microfluidic channels derived from a UV/thermally cured preceramic polymer via a soft lithographic technique. Microelectron Eng 2007;84:2892–5.
[226] Martínez-Crespiera S, Ionescu E, Schlosser M, Flittner K, Mistura G, Riedel R, et al. Fabrication of silicon oxycarbide-based microcomponents via photolithographic and soft lithography approaches. Sensor Actuat A-Phys 2011;169:242–9.
[227] Yang H, Deschatelets P, Brittain ST, Whitesides GM. Fabrication of high performance ceramic microstructures from a polymeric precursor using soft lithography. Adv Mater 2001;13:54–8.
[228] Kaur S, Riedel R, Ionescu E. Pressureless fabrication of dense monolithic SiC ceramics from a polycarbosilane. J Eur Ceram Soc 2014;34:3571–8.
[229] Liu X, Yu Z, Ishikawa R, Chen L, Yin X, Ikuhara Y, et al. Single-source-precursor synthesis and electromagnetic properties of novel RGO–SiCN ceramic nanocomposites. J Mater Chem C 2017;5:7950–60.
[230] Toma L, Kleebe HJ, Müller MM, Janssen E, Riedel R, Melz T, et al. Correlation between intrinsic microstructure and piezoresistivity in a SiOC polymer-derived ceramic. J Am Ceram Soc 2012;95:1056–61.
[231] Bechelany MC, Proust V, Gervais C, Ghisleni R, Bernard S, Miele P. In situ controlled growth of titanium nitride in amorphous silicon nitride: a general route toward bulk nitride nanocomposites with very high hardness. Adv Mater 2014;26:6548–53.
[232] Baldwin LA, Rueschhoff LM, Deneault JR, Cissel KS, Nikolaev P, Cinibulk MK, et al. Synthesis of a two-component carbosilane system for the advanced manufacturing of polymer-derived ceramics. Chem Mater 2018;30:7527–34.
[233] Pierin G, Grotta C, Colombo P, Mattevi C. Direct Ink Writing of micrometric SiOC ceramic structures using a preceramic polymer. J Eur Ceram Soc 2016;36:1589–94.
[234] Jana P, Santoliquido O, Ortona A, Colombo P, Sorarù GD. Polymer-derived SiCN cellular structures from replica of 3D printed lattices. J Am Ceram Soc 2018;101:2732–8.
[235] Santoliquido O, Colombo P, Ortona A. Additive manufacturing of ceramic components by digital light processing: a comparison between the “bottom-up” and the “top-down” approaches. J Eur Ceram Soc 2019;39:2140–8.
[236] Colombo P, Bernardo E, Parcianello G. Multifunctional advanced ceramics from preceramic polymers and nano-sized active fillers. J Eur Ceram Soc 2013;33:453–69.
[237] Konegger T, Liersch A, Gierl C, Scheffler M. Bulk ceramic composites derived from a preceramic polysilazane with alumina and zirconia fillers. Adv Eng Mater 2013;15:394–406.
[238] Rocha RMd, Greil P, Bressiani JC. Bressiani AHdA. Complex-shaped ceramic composites obtained by machining compact polymer-filler mixtures. Mat Res 2005;8:191–6.
[239] Schmidt J, Altun AA, Schwentenwein M, Colombo P. Complex mullite structures fabricated via digital light processing of a preceramic polysiloxane with active alumina fillers. J Eur Ceram Soc 2019;39:1336–43.
[240] Evans J. Seventy ways to make ceramics. J Eur Ceram Soc 2008;28:1421–32.
[241] Ki Kakimoto, Wakai F, Bill J, Aldinger F. Synthesis of Si-C-O bulk ceramics with various chemical compositions from polycarbosilane. J Am Ceram Soc 1999;82:2337–41.
[242] Su D, Li Y-L, An H-J, Liu X, Hou F, Li J-Y, et al. Pyrolytic transformation of liquid precursors to shaped bulk ceramics. J Eur Ceram Soc 2010;30:1503–11.
[243] Choong Kwet Yive N, Corriu R, Leclercq D, Mutin P, Vioux A. Silicon carbonitride from polymeric precursors: thermal cross-linking and pyrolysis of oligosilazane model compounds. Chem Mater 1992;4:141–6.
[244] Lavedrine A, Bahloul D, Goursat P, Yive NCK, Corriu R, Leclerq D, et al. Pyrolysis of polyvinylsilazane precursors to silicon carbonitride. J Eur Ceram Soc 1991;8:221–7.
[245] Wen Q, Xu Y, Xu B, Fasel C, Guillon O, Buntkowsky G, et al. Single-source-precursor synthesis of dense SiC/HfC_xN_{1-x}-based ultrahigh-temperature ceramic nanocomposites. Nanoscale 2014;6:13678–89.
[246] Kaur S, Cherkashinin G, Fasel C, Kleebe H-J, Ionescu E, Riedel R. Single-source-precursor synthesis of novel V_8C_7/SiC(O)-based ceramic nanocomposites. J Eur Ceram Soc 2016;36:3553–63.
[247] Wang C, Wang J, Park C, Kim Y-W. Cross-linking behavior of a polysiloxane in preceramic foam processing. J Mater Sci 2004;39:4913–5.
[248] Yajima S, Hasegawa Y, Hayashi J, Iimura M. Synthesis of continuous silicon carbide fibre with high tensile strength and high Young's modulus. J Mater Sci 1978;13:2569–76.
[249] Yajima S, Hasegawa Y, Okamura K, Matsuzawa T. Development of high tensile strength silicon carbide fibre using an organosilicon polymer precursor. Nature 1978;273:525.
[250] Hasegawa Y, Iimura M, Yajima S. Synthesis of continuous silicon carbide fibre. J Mater Sci 1980;15:720–8.
[251] Hasegawa Y. Synthesis of continuous silicon carbide fibre. J Mater Sci 1989;24:1177–90.
[252] Ichikawa H, Machino F, Mitsuno S, Ishikawa T, Okamura K, Hasegawa Y. Synthesis of continuous silicon carbide fibre. J Mater Sci 1986;21:4352–8.
[253] Ichikawa H. Polymer-derived ceramic fibers. Annu Rev Mater Res 2016;46:335–56.
[254] Su Z, Zhang L, Li Y, Li S, Chen L. Rapid preparation of SiC fibers using a curing route of electron irradiation in a low oxygen concentration atmosphere. J Am Ceram Soc 2015;98:2014–7.
[255] Cramer NB, Reddy SK, Lu H, Cross T, Raj R, Bowman CN. Thiol-ene photopolymerization of polymer-derived ceramic precursors. J Polym Sci, Part A: Polym Chem 2004;42:1752–7.
[256] He W, Chen L, Peng F. Coating formed by SiBCN single source precursor via UV-photopolymerization. Mater Lett 2017;206:121–3.
[257] Pham TA, Kim P, Kwak M, Suh KY, Kim D-P. Inorganic polymer photoresist for direct ceramic patterning by photolithography. Chem Commun 2007:4021–3.
[258] Schulz M, Börner M, Göttert J, Hanemann T, Haußelt J, Motz G. Cross linking behavior of preceramic polymers effected by UV-and synchrotron radiation. Adv Eng Mater 2004;6:676–80.
[259] Hasegawa Y. Si-C fiber prepared from polycarbosilane cured without oxygen. J Inorg Organomet Polym 1992;2:161–9.
[260] Rabe JA, Lipowitz J, Lu PP. Curing preceramic polymers by exposure to nitrogen dioxide. Google Patents; 1991.
[261] Hasegawa Y. New curing method for polycarbosilane with unsaturated hydrocarbons and application to thermally stable SiC fibre. Compos Sci Technol 1994;51:161–6.
[262] Hayashida A, Takamizawa M, Takeda Y. Preparation of hollow ceramic fibers. Google Patents; 1990.
[263] Lipowitz J. Infusible preceramic polymers via plasma treatment. Google Patents; 1988.
[264] Whinnery LL, Nichols MC, Wheeler DR, Loy DA. Process for preparing silicon carbide foam. Google Patents; 1997.
[265] Perale G, Giordano C, Daniele F, Masi M, Colombo P, Gottardo L, et al. A novel process for the manufacture of ceramic microelectrodes for biomedical applications. Int J Appl Ceram Tec 2008;5:37–43.
[266] Zanchetta E, Cattaldo M, Franchin G, Schwentenwein M, Homa J, Brusatin G, et al. Stereolithography of SiOC ceramic microcomponents. Adv Mater 2016;28:370–6.
[267] Hundley JM, Eckel ZC, Schueller E, Cante K, Biesboer SM, Yahata BD, et al. Geometric characterization of additively manufactured polymer derived ceramics. Addit Manuf 2017;18:95–102.
[268] Friedel T, Travitzky N, Niebling F, Scheffler M, Greil P. Fabrication of polymer derived ceramic parts by selective laser curing. J Eur Ceram Soc 2005;25:193–7.
[269] Zocca A, Gomes CM, Staude A, Bernardo E, Günster J, Colombo P. SiOC ceramics with ordered porosity by 3D-printing of a preceramic polymer. J Mater Res 2013;28:2243–52.
[270] Zocca A, Colombo P, Gomes CM, Günster J. Additive manufacturing of ceramics: issues, potentialities, and opportunities. J Am Ceram Soc 2015;98:1983–2001.
[271] Colombo P, Schmidt J, Franchin G, Zocca A, Günster J. Additive manufacturing techniques for fabricating complex ceramic components from preceramic polymers. Am Ceram Soc Bull 2017;96:16–23.
[272] Tian X, Zhang W, Li D, Heinrich JG. Reaction-bonded SiC derived from resin precursors by stereolithography. Ceram Int 2012;38:589–97.

[273] de Hazan Y, Penner D. SiC and SiOC ceramic articles produced by stereolithography of acrylate modified polycarbosilane systems. J Eur Ceram Soc 2017;37:5205–12.
[274] Li S, Duan W, Zhao T, Han W, Wang L, Dou R, et al. The fabrication of SiBCN ceramic components from preceramic polymers by digital light processing (DLP) 3D printing technology. J Eur Ceram Soc 2018;38:4597–603.
[275] Brinckmann SA, Patra N, Yao J, Ware TH, Frick CP, Fertig III RS. Stereolithography of SiOC polymer-derived ceramics filled with SiC micronwhiskers. Adv Eng Mater 2018;20:1800593.
[276] Bouyer E, Schiller G, Müller M, Henne R. Thermal plasma chemical vapor deposition of Si-based ceramic coatings from liquid precursors. Plasma Chem Plasma Process 2001;21:523–46.
[277] Mukherjee J, Ranjan A, Saxena A, Das PK, Banerjee R. Liquid polycarbosilane derived SiC coating on silicon (1 1 1) wafer for enhanced mechanical properties. Appl Surf Sci 2013;270:219–24.
[278] Krüger U, Ullrich R. Producing a ceramic layer by spraying polymer ceramic precursor particles onto a surface comprises using a cold gas spray nozzle. German: Siemens AG; 2006.
[279] Chandra G, Martin TE. Rapid thermal process for obtaining silica coatings. Midland, Mich.: Dow Corning Corporation; 1991.
[280] Colombo P, Martucci A, Fogato O, Villoresi P. Silicon carbide films by laser pyrolysis of polycarbosilane. J Am Ceram Soc 2001;84:224–6.
[281] Müller A, Herlin-Boime N, Ténégal F, Armand X, Berger F, Flank AM, et al. Comparison of Si/C/N pre-ceramics obtained by laser pyrolysis or furnace thermolysis. J Eur Ceram Soc 2003;23:37–46.
[282] Wilden J, Fischer G. Laser synthesis of nanostructured ceramics from liquid precursors. Appl Surf Sci 2007;254:1067–72.
[283] Liu J, Qiao Y, Zhang P, Xue Y, Cai Z. Synthesis of SiC ceramics from polysilazane by laser pyrolysis. Surf Coat Technol 2017;321:491–5.
[284] Tangermann-Gerk K, Barroso G, Weisenseel B, Greil P, Fey T, Schmidt M, et al. Laser pyrolysis of an organosilazane-based glass/ZrO_2 composite coating system. Mater Desi 2016;109:644–51.
[285] Wilden J, Bergmann JP, Schlichting S, Dolles M. Direct laser pyrolysis of nanostructured micro components. In: International congress on applications of lasers & electro-optics: LIA; 2006. p. M1103.
[286] Ma R, Erb D, Lu K. Flash pyrolysis of polymer-derived SiOC ceramics. J Eur Ceram Soc 2018;38:4906–14.
[287] Danko GA, Silberglitt R, Colombo P, Pippel E, Woltersdorf J. Comparison of microwave hybrid and conventional heating of preceramic polymers to form silicon carbide and silicon oxycarbide ceramics. J Am Ceram Soc 2000;83:1617–25.
[288] Zunjarrao SC, Dyjak P, Rahman A, Metzger JD, Singh RP. Microwave processing of actively seeded precursor for fabrication of polymer derived ceramics. J Am Ceram Soc 2016;99:2260–6.
[289] Pivin JC, Colombo P, Tonidandel M. Ion irradiation of preceramic polymer thin films. J Am Ceram Soc 1996;79:1967–70.
[290] Pivin JC, Colombo P, Sorarù GD. Comparison of ion irradiation effects in silicon-based preceramic thin films. J Am Ceram Soc 2000;83:713–20.
[291] Pivin J, Colombo P. Ceramic coatings by ion irradiation of polycarbosilanes and polysiloxanes: Part II Hardness and thermochemical stability. J Mater Sci 1997;32:6175–82.
[292] Pivin J, Colombo P. Ceramic coatings by ion irradiation of polycarbosilanes and polysiloxanes: Part I Conversion mechanism. J Mater Sci 1997;32:6163–73.
[293] Tsukuda S, Seki S, Tagawa S, Sugimoto M, Idesaki A, Tanaka S, et al. Fabrication of nanowires using high-energy ion beams. J Phys Chem B 2004;108:3407–9.
[294] Srivastava S, Avasthi D, Pivin J. Mechanism of H release from Si-based polymers under ion irradiation. Nucl Instrum Methods Phys Res, Sect B 2002;191:718–22.
[295] Pivin J, Colombo P, Sendova-Vassileva M, Salomon J, Sagon G, Quaranta A. Ion-induced conversion of polysiloxanes and polycarbosilanes into ceramics: Mechanisms and properties. Nucl Instrum Methods Phys Res, Sect B 1998;141:652–62.
[296] Kumar A, Singh F, Pivin J, Avasthi D. Photoluminescence studies of carbon clusters formed by irradiation of Si-based polymer. Radiat Measur 2005;40:785–8.
[297] Narisawa M, Watase S, Matsukawa K, Dohmaru T, Okamura K. White Si-O-C(-H) particles with photoluminescence synthesized by decarbonization reaction on polymer precursor in a hydrogen atmosphere. Bull Chem Soc Jpn 2012;85:724–6.
[298] Dong S, Chollon G, Labrugere C, Lahaye M, Guette A, Bruneel J, et al. Characterization of nearly stoichiometric SiC ceramic fibres. J Mater Sci 2001;36:2371–81.
[299] Liang T, Li Y-L, Su D, Du H-B. Silicon oxycarbide ceramics with reduced carbon by pyrolysis of polysiloxanes in water vapor. J Eur Ceram Soc 2010;30:2677–82.
[300] Choong Kwet Yive N, Corriu R, Leclercq D, Mutin P, Vioux A. Thermogravimetric analysis/mass spectrometry investigation of the thermal conversion of organosilicon precursors into ceramics under argon and ammonia. 2. Poly (silazanes). Chem Mater 1992;4:1263–71.
[301] Breval E, Hammond M, Pantano CG. Nanostructural characterization of silicon oxycarbide glasses and glass-ceramics. J Am Ceram Soc 1994;77:3012–8.
[302] Esfehanian M, Oberacker R, Fett T, Hoffmann MJ. Development of dense filler-free polymer-derived SiOC ceramics by field-assisted sintering. J Am Ceram Soc 2008;91:3803–5.
[303] Kleebe HJ, Suttor D, Müller H, Ziegler G. Decomposition-crystallization of polymer-derived Si-C-N ceramics. J Am Ceram Soc 1998;81:2971–7.
[304] Kumar R, Cai Y, Gerstel P, Rixecker G, Aldinger F. Processing, crystallization and characterization of polymer derived nano-crystalline Si-B-C-N ceramics. J Mater Sci 2006;41:7088–95.
[305] Zemanová M, Lecomte E, Šajgalík P, Riedel R. Polysilazane derived micro/nano Si_3N_4/SiC composites. J Eur Ceram Soc 2002;22:2963–8.
[306] Gasch MJ, Wan J, Mukherjee A. Preparation of a Si_3N_4/SiC nanocomposite by high-pressure sintering of polymer precursor derived powders. Scripta Mater 2001;45:1063–8.
[307] Xu T, Ma Q, Chen Z. High-temperature behavior of silicon oxycarbide glasses in air environment. Ceram Int 2011;37:2555–9.
[308] Bouillon E, Langlais F, Pailler R, Naslain R, Cruege F, Huong P, et al. Conversion mechanisms of a polycarbosilane precursor into an SiC-based ceramic material. J Mater Sci 1991;26:1333–45.
[309] Ionescu E, Papendorf B, Kleebe HJ, Riedel R. Polymer-derived silicon oxycarbide/hafnia ceramic nanocomposites. Part II: stability toward decomposition and microstructure evolution at T≫ 1000 °C. J Am Ceram Soc 2010;93:1783–9.
[310] Wen Q, Yu Z, Xu Y, Lu Y, Fasel C, Morita K, et al. SiC/$Hf_yTa_{1-y}CxN_{1-x}$/C ceramic nanocomposites with $Hf_yTa_{1-y}C_xN_{1-x}$-carbon core-shell nanostructure and the influence of the carbon-shell thickness on electrical properties. J Mater Chem C 2018;6:855–64.
[311] Ishihara S, Gu H, Bill J, Aldinger F, Wakai F. Densification of precursor-derived Si-C-N ceramics by high-pressure hot isostatic pressing. J Am Ceram Soc 2002;85:1706–12.
[312] Stabler C, Schliephake D, Heilmaier M, Rouxel T, Kleebe HJ, Narisawa M, et al. Influence of SiC/silica and carbon/silica interfaces on the high-temperature creep of silicon oxycarbide-based glass ceramics: a case study. Adv Eng Mater 2018.
[313] Stabler C, Reitz A, Stein P, Albert B, Riedel R, Ionescu E. Thermal properties of SiOC glasses and glass ceramics at elevated temperatures. Materials 2018;11:279.
[314] Wan J, Gasch MJ, Mukherjee AK. Silicon nitride–silicon carbide nancocomposites fabricated by electric-field-assisted sintering. J Am Ceram Soc 2003;86:526–8.
[315] Pizon D, Charpentier L, Lucas R, Foucaud S, Maitre A, Balat-Pichelin M. Oxidation behavior of spark plasma sintered ZrC–SiC composites obtained from the polymer-derived ceramics route. Ceram Int 2014;40:5025–31.
[316] Bechelany MC, Salameh C, Viard A, Guichaoua L, Rossignol F, Chartier T, et al. Preparation of polymer-derived Si-B-C-N monoliths by spark plasma sintering technique. J Eur Ceram Soc 2015;35:1361–74.
[317] Lucas R, Davis CE, Clegg WJ, Pizon D, Babonneau F, Foucaud S, et al. Elaboration of ZrC-SiC composites by spark plasma sintering using polymer-derived ceramics. Ceram Int 2014;40:15703–9.
[318] Yang W, Fan Z, Wang H, Xie Z, Miao H, An L. Fabrication of Si_3N_4/SiC nanocomposites by spark plasma sintering of amorphous SiCN powders derived from a polymeric precursor. J Ceram Process Res 2006;7:307.
[319] Mazo MA, Palencia C, Nistal A, Rubio F, Rubio J, Oteo JL. Dense bulk silicon oxycarbide glasses obtained by spark plasma sintering. J Eur Ceram Soc 2012;32:3369–78.

[320] Chen S, Gou Y, Wang H, Wang J. Fabrication and characterization of precursor-derived non-oxide ZrC-SiC multiphase ultrahigh temperature ceramics. J Eur Ceram Soc 2016;36:3843–50.
[321] Rahman A, Singh A, Harimkar SP, Singh RP. Mechanical characterization of fine grained silicon carbide consolidated using polymer pyrolysis and spark plasma sintering. Ceram Int 2014;40:12081–91.
[322] Duan RG, Garay JE, Kuntz JD, Mukherjee AK. Electrically conductive in situ formed nano-Si_3N_4/SiC/TiC_xN_{1-x} ceramic composite consolidated by pulse electric current sintering (PECS). J Am Ceram Soc 2005;88:66–70.
[323] Yuan J, Li D, Johanns KE, Fasel C, Durst K, Kleebe H-J, et al. Preparation of dense SiHf (B) CN-based ceramic nanocomposites via rapid spark plasma sintering. J Eur Ceram Soc 2017;37:5157–65.
[324] Dzivenko DA, Zerr A, Bulatov VK, Miehe G, Li J, Thybusch B, et al. High-pressure multianvil synthesis and structure refinement of oxygen-bearing cubic zirconium (IV) nitride. Adv Mater 2007;19:1869–73.
[325] Schwarz M, Miehe G, Zerr A, Kroke E, Poe BT, Fuess H, et al. Spinel-Si_3N_4: Multi-anvil press synthesis and structural refinement. Adv Mater 2000;12:883–7.
[326] Zerr A, Miehe G, Serghiou G, Schwarz M, Kroke E, Riedel R, et al. Synthesis of cubic silicon nitride. Nature 1999;400:340.
[327] Riedel R, Wiehl L, Zerr A, Zinin P, Kroll P. Superhard materials. Handbook of solid state chemistry; 2017. p. 175–200.
[328] Yeon S-H, Reddington P, Gogotsi Y, Fischer JE, Vakifahmetoglu C, Colombo P. Carbide-derived-carbons with hierarchical porosity from a preceramic polymer. Carbon 2010;48:201–10.
[329] Vakifahmetoglu C, Presser V, Yeon S-H, Colombo P, Gogotsi Y. Enhanced hydrogen and methane gas storage of silicon oxycarbide derived carbon. Microporous Mesoporous Mater 2011;144:105–12.
[330] Presser V, Yeon SH, Vakifahmetoglu C, Howell CA, Sandeman SR, Colombo P, et al. Hierarchical porous carbide-derived carbons for the removal of cytokines from blood plasma. Adv Healthc Mater 2012;1:796–800.
[331] Wang J, Oschatz M, Biemelt T, Borchardt L, Senkovska I, Lohe MR, et al. Synthesis, characterization, and hydrogen storage capacities of hierarchical porous carbide derived carbon monolith. J Mater Chem 2012;22:23893–9.
[332] Oschatz M, Kockrick E, Rose M, Borchardt L, Klein N, Senkovska I, et al. A cubic ordered, mesoporous carbide-derived carbon for gas and energy storage applications. Carbon 2010;48:3987–92.
[333] Oschatz M, Nickel W, Thommes M, Cychosz K, Leistner M, Adam M, et al. Evolution of porosity in carbide-derived carbon aerogels. J Mater Chem A 2014;2:18472–9.
[334] Peña-Alonso R, Sorarù GD, Raj R. Preparation of ultrathin-walled carbon-based nanoporous structures by etching pseudo-amorphous silicon oxycarbide ceramics. J Am Ceram Soc 2006;89:2473–80.
[335] Wilson A, Zank G, Eguchi K, Xing W, Yates B, Dahn J. Pore creation in silicon oxycarbides by rinsing in dilute hydrofluoric acid. Chem Mater 1997;9:2139–44.
[336] Bill J, Kamphowe TW, Müller A, Wichmann T, Zern A, Jalowieki A, et al. Precursor-derived Si-(B-)C-N ceramics: thermolysis, amorphous state and crystallization. Appl Organomet Chem 2001;15:777–93.
[337] Saha A, Raj R, Williamson D, Kleebe HJ. Characterization of nanodomains in polymer-derived SiCN ceramics employing multiple techniques. J Am Ceram Soc 2005;88:232–4.
[338] Saha A, Raj R, Williamson DL. A model for the nanodomains in polymer-derived SiCO. J Am Ceram Soc 2006;89:2188–95.
[339] Mera G, Tamayo A, Nguyen H, Sen S, Riedel R. Nanodomain structure of carbon-rich silicon carbonitride polymer-derived ceramics. J Am Ceram Soc 2010;93:1169–75.
[340] Liao N, Xue W, Zhou H, Zhang M. Numerical investigation into the nanostructure and mechanical properties of amorphous SiBCN ceramics. RSC Adv 2013;3:14458–65.
[341] Tomar V, Gan M, Kim HS. Atomistic analyses of the effect of temperature and morphology on mechanical strength of Si-C-N and Si-C-O nanocomposites. J Eur Ceram Soc 2010;30:2223–37.
[342] Liao N, Xue W, Zhang M. Effect of carbon content on structural and mechanical properties of SiCN by atomistic simulations. J Eur Ceram Soc 2012;32:1275–81.
[343] Kroll P. Searching insight into the atomistic structure of SiCO ceramics. J Mater Chem 2010;20:10528–34.
[344] Amkreutz M, Frauenheim T. Understanding precursor-derived amorphous Si-CN ceramics on the atomic scale. Phys Rev B 2002;65:134113.
[345] Resta N, Kohler C, Trebin HR. Molecular dynamics simulations of amorphous Si-C-N ceramics: composition dependence of the atomic structure. J Am Ceram Soc 2003;86:1409–14.
[346] Matsunaga K, Iwamoto Y. Molecular dynamics study of atomic structure and diffusion behavior in amorphous silicon nitride containing boron. J Am Ceram Soc 2001;84:2213–9.
[347] Kleebe HJ, Turquat C, Sorarù GD. Phase separation in an SiCO glass studied by transmission electron microscopy and electron energy-loss spectroscopy. J Am Ceram Soc 2001;84:1073–80.
[348] Widgeon S, Sen S, Mera G, Ionescu E, Riedel R, Navrotsky A. ^{29}Si and ^{13}C solid-state NMR spectroscopic study of nanometer-scale structure and mass fractal characteristics of amorphous polymer derived silicon oxycarbide ceramics. Chem Mater 2010;22:6221–8.
[349] Sen S, Stebbins J. Phase separation, clustering, and fractal characteristics in glass: a magic-angle-spinning NMR spin-lattice relaxation study. Phys Rev B 1994;50:822.
[350] Schuhmacher J, Weinmann M, Bill J, Aldinger F, Müller K. Solid-state NMR studies of the preparation of Si-CN ceramics from polysilylcarbodiimide polymers. Chem Mater 1998;10:3913–22.
[351] Gabriel AO, Riedel R, Dressler W, Reichert S, Gervais C, Maquet J, et al. Thermal decomposition of poly (methylsilsesquicarbodiimide) to amorphous Si-C-N ceramics. Chem Mater 1999;11:412–20.
[352] Iwamoto Y, Völger W, Kroke E, Riedel R, Saitou T, Matsunaga K. Crystallization behavior of amorphous silicon carbonitride ceramics derived from organometallic precursors. J Am Ceram Soc 2001;84:2170–8.
[353] Michelle Morcos R, Mera G, Navrotsky A, Varga T, Riedel R, Poli F, et al. Enthalpy of formation of carbon-rich polymer-derived amorphous SiCN ceramics. J Am Ceram Soc 2008;91:3349–54.
[354] Widgeon S, Mera G, Gao Y, Stoyanov E, Sen S, Navrotsky A, et al. Nanostructure and energetics of carbon-rich SiCN ceramics derived from polysilylcarbodiimides: role of the nanodomain interfaces. Chem Mater 2012;24:1181–91.
[355] Chen Y, Yang X, Cao Y, Gan Z, An L. Quantitative study on structural evolutions and associated energetics in polysilazane-derived amorphous silicon carbonitride ceramics. Acta Mater 2014;72:22–31.
[356] Seitz J, Bill J, Egger N, Aldinger F. Structural investigations of Si/C/N-ceramics from polysilazane precursors by nuclear magnetic resonance. J Eur Ceram Soc 1996;16:885–91.
[357] Traßl S, Suttor D, Motz G, Rössler E, Ziegler G. Structural characterisation of silicon carbonitride ceramics derived from polymeric precursors. J Eur Ceram Soc 2000;20:215–25.
[358] Zhou C, Gao X, Xu Y, Buntkowsky G, Ikuhara Y, Riedel R, et al. Synthesis and high-temperature evolution of single-phase amorphous Si-Hf-N ceramics. J Eur Ceram Soc 2015;35:2007–15.
[359] Widgeon S, Mera G, Gao Y, Sen S, Navrotsky A, Riedel R. Effect of precursor on speciation and nanostructure of SiBCN polymer-derived ceramics. J Am Ceram Soc 2013;96:1651–9.
[360] Sarkar S, Gan Z, An L, Zhai L. Structural evolution of polymer-derived amorphous SiBCN ceramics at high temperature. J Phys Chem C 2011;115:24993–5000.
[361] Martínez-Crespiera S, Ionescu E, Kleebe H-J, Riedel R. Pressureless synthesis of fully dense and crack-free SiOC bulk ceramics via photo-crosslinking and pyrolysis of a polysiloxane. J Eur Ceram Soc 2011;31:913–9.
[362] Prasad RM, Mera G, Morita K, Müller M, Kleebe H-J, Gurlo A, et al. Thermal decomposition of carbon-rich polymer-derived silicon carbonitrides leading to ceramics with high specific surface area and tunable micro-and mesoporosity. J Eur Ceram Soc 2012;32:477–84.
[363] Störmer H, Kleebe H-J, Ziegler G. Metastable SiCN glass matrices studied by energy-filtered electron diffraction pattern analysis. J Non-Cryst Solids 2007;353:2867–77.

[364] Janakiraman N, Aldinger F. Fabrication and characterization of fully dense Si-C-N ceramics from a poly (ureamethylvinyl) silazane precursor. J Eur Ceram Soc 2009;29:163–73.
[365] Kleebe HJ, Störmer H, Trassl S, Ziegler G. Thermal stability of SiCN ceramics studied by spectroscopy and electron microscopy. Appl Organomet Chem 2001;15:858–66.
[366] Plachký T, Lenčéš Z, Hric Ľ, Šajgalík P, Baláž P, Riedel R, et al. Processing and mechanical properties of Si_3N_4 composites employing polymer-derived SiAlOC as sintering aid. J Eur Ceram Soc 2010;30:759–67.
[367] Kim KJ, Eom J-H, Koh TY, Kim Y-W, Seo W-S. Effects of carbon addition on the electrical properties of bulk silicon-oxycarbide ceramics. J Eur Ceram Soc 2016;36:2705–11.
[368] Wen Q, Feng Y, Yu Z, Peng DL, Nicoloso N, Ionescu E, et al. Microwave absorption of SiC/HfC_xN_{1-x}/C ceramic nanocomposites with HfC_xN_{1-x}-carbon core-shell particles. J Am Ceram Soc 2016;99:2655–63.
[369] Wen Q, Yu Z, Lonescu E, Riedel R. Single-source-precursor synthesis and high-temperature evolution of a boron-containing SiC/HfC ceramic nanocomposite. Unpublished work.
[370] Meng L, Zhang X, Tang Y, Su K, Kong J. Hierarchically porous silicon-carbon-nitrogen hybrid materials towards highly efficient and selective adsorption of organic dyes. Sci Rep 2015;5:7910.
[371] Roth F, Waleska P, Hess C, Ionescu E, Nicoloso N. UV Raman spectroscopy of segregated carbon in silicon oxycarbides. J Ceram Soc Jpn 2016;124:1042–5.
[372] Nyczyk-Malinowska A, Wójcik-Bania M, Gumuła T, Hasik M, Cypryk M, Olejniczak Z. New precursors to SiCO ceramics derived from linear poly (vinylsiloxanes) of regular chain composition. J Eur Ceram Soc 2014;34:889–902.
[373] Trassl S, Motz G, Rössler E, Ziegler G. Characterisation of the free-carbon phase in precursor-derived SiCN ceramics. J Non-Cryst Solids 2001;293:261–7.
[374] Jiang T, Wang Y, Wang Y, Orlovskaya N, An L. Quantitative raman analysis of free carbon in polymer-derived ceramics. J Am Ceram Soc 2009;92:2455–8.
[375] Wang Y, Zhang L, Xu W, Jiang T, Fan Y, Jiang D, et al. Effect of thermal initiator concentration on the electrical behavior of polymer-derived amorphous silicon carbonitrides. J Am Ceram Soc 2008;91:3971–5.
[376] Segatelli MG, Pires ATN, Yoshida IVP. Synthesis and structural characterization of carbon-rich SiC_xO_y derived from a Ni-containing hybrid polymer. J Eur Ceram Soc 2008;28:2247–57.
[377] Sasaki Y, Nishina Y, Sato M, Okamura K. Raman study of SiC fibres made from polycarbosilane. J Mater Sci 1987;22:443–8.
[378] Tuinstra F, Koenig JL. Raman spectrum of graphite. J Chem Phys 1970;53:1126–30.
[379] Lespade P, Al-Jishi R, Dresselhaus M. Model for Raman scattering from incompletely graphitized carbons. Carbon 1982;20:427–31.
[380] Yarbrough WA, Messier R. Current issues and problems in the chemical vapor deposition of diamond. Science 1990;247:688–96.
[381] Nemanich RJ, Solin S. First-and second-order Raman scattering from finite-size crystals of graphite. Phys Rev B 1979;20:392.
[382] Nathan MI, Smith Jr JE, Tu K. Raman spectra of glassy carbon. J Appl Phys 1974;45:2370-.
[383] Trassl S, Motz G, Rössler E, Ziegler G. Characterization of the free-carbon phase in precursor-derived Si-C-N ceramics: I. Spectroscopic methods. J Am Ceram Soc 2002;85:239–44.
[384] Nistor LC, Van Landuyt J, Ralchenko V, Kononenko T, Obraztsova ED, Strelnitsky V. Direct observation of laser-induced crystallization of aC: H films. Appl Phys A 1994;58:137–44.
[385] Lipowitz J, Freeman H, Goldberg H, Chen R, Prack E. Structure and properties of ceramic fibers prepared from polymeric precursors. MRS Online Proceed Libra Arch 1986;73.
[386] Sasaki Y, Sato M, Okamura K, Nishina Y. Raman scattering of inorganic fibers. Sci Rep Res Inst, Tohoku Univ Ser A, Phys, Chem Metall 1985;32:111–5.
[387] Sadezky A, Muckenhuber H, Grothe H, Niessner R, Pöschl U. Raman microspectroscopy of soot and related carbonaceous materials: spectral analysis and structural information. Carbon 2005;43:1731–42.
[388] Thomsen C, Reich S. Double resonant Raman scattering in graphite. Phys Rev Lett 2000;85:5214.
[389] Zickler GA, Smarsly B, Gierlinger N, Peterlik H, Paris O. A reconsideration of the relationship between the crystallite size La of carbons determined by X-ray diffraction and Raman spectroscopy. Carbon 2006;44:3239–46.
[390] Saito R, Jorio A, Souza Filho A, Dresselhaus G, Dresselhaus M, Pimenta M. Probing phonon dispersion relations of graphite by double resonance Raman scattering. Phys Rev Lett 2001;88:027401.
[391] Pimenta M, Dresselhaus G, Dresselhaus MS, Cancado L, Jorio A, Saito R. Studying disorder in graphite-based systems by Raman spectroscopy. Phys Chem Chem Phys 2007;9:1276–90.
[392] Matthews M, Pimenta M, Dresselhaus G, Dresselhaus M, Endo M. Origin of dispersive effects of the Raman D band in carbon materials. Phys Rev B 1999;59:R6585.
[393] Pócsik I, Hundhausen M, Koós M, Ley L. Origin of the D peak in the Raman spectrum of microcrystalline graphite. J Non-Cryst Solids 1998;227:1083–6.
[394] Ferrari AC. Raman spectroscopy of graphene and graphite: disorder, electron–phonon coupling, doping and nonadiabatic effects. Solid State Commun 2007;143:47–57.
[395] Knight DS, White WB. Characterization of diamond films by Raman spectroscopy. J Mater Res 1989;4:385–93.
[396] Ferrari AC, Robertson J. Interpretation of Raman spectra of disordered and amorphous carbon. Phys Rev B 2000;61:14095.
[397] Cançado L, Takai K, Enoki T, Endo M, Kim Y, Mizusaki H, et al. General equation for the determination of the crystallite size L a of nanographite by Raman spectroscopy. Appl Phys Lett 2006;88:163106.
[398] Bai H, Wen G, Huang X, Han Z, Zhong B, Hu Z, et al. Synthesis and structural characterization of SiBOC ceramic fibers derived from single-source polyborosiloxane. J Eur Ceram Soc 2011;31:931–40.
[399] Yan M, Song W, Zhao-hui C. Raman spectroscopy studies of the high-temperature evolution of the free carbon phase in polycarbosilane derived SiC ceramics. Ceram Int 2010;36:2455–9.
[400] Li X, Wang K, Ma B, Hong H, Zhang M, Liu J, et al. Effect of acrylic acid additive on electric conductivity of polymer-derived amorphous silicon carbonitride. Ceram Int 2015;41:7971–6.
[401] Kousaalya AB, Kumar R, Packirisamy S. Characterization of free carbon in the as-thermolyzed Si-BCN ceramic from a polyorganoborosilazane precursor. J Adv Ceram 2013;2:325–32.
[402] Wang K, Ma B, Li X, Wang Y, An L. Structural evolutions in polymer-derived carbon-rich amorphous silicon carbide. J Phys Chem A 2015;119:552–8.
[403] Lucchese MM, Stavale F, Ferreira EM, Vilani C, Moutinho M, Capaz RB, et al. Quantifying ion-induced defects and Raman relaxation length in graphene. Carbon 2010;48:1592–7.
[404] Cuesta A, Dhamelincourt P, Laureyns J, Martinez-Alonso A, Tascón JD. Raman microprobe studies on carbon materials. Carbon 1994;32:1523–32.
[405] Li W, Li D, Gao X, Gurlo A, Zander S, Jones P, et al. A study on the thermal conversion of scheelite-type ABO_4 into perovskite-type AB (O, N_j3. Dalton T 2015;44:8238–46.
[406] Dasgupta K, Sathiyamoorthy D. Disordered carbon-its preparation, structure, and characterisation. Mater Sci Technol 2003;19:995–1002.
[407] Johnson CA, Patrick JW, Thomas KM. Characterization of coal chars by Raman spectroscopy, X-ray diffraction and reflectance measurements. Fuel 1986;65:1284–90.
[408] Manivannan A, Chirila M, Giles N, Seehra M. Microstructure, dangling bonds and impurities in activated carbons. Carbon 1999;37:1741–7.
[409] Kercher AK, Nagle DC. Microstructural evolution during charcoal carbonization by X-ray diffraction analysis. Carbon 2003;41:15–27.
[410] Soraru G, Babonneau F, Mackenzie J. Structural evolutions from polycarbosilane to SiC ceramic. J Mater Sci 1990;25:3886–93.
[411] Brodie N, Majoral JP, Disson JP. An NMR study of the step by step pyrolysis of a polysilazane precursor of silicon nitride. Inorg Chem 1993;32:4646–9.
[412] Bill J, Seitz J, Thurn G, Dürr J, Canel J, Janos B, et al. Structure analysis and properties of Si–C–N ceramics derived from polysilazanes. Phys Status Solidi a 1998;166:269–96.
[413] Sehlleier YH, Verhoeven A, Jansen M. NMR studies of short and intermediate range ordering of amorphous Si-B-N-C-H pre-ceramic at the pyrolysis stage of 600 °C. J Mater Chem 2007;17:4316–9.

[414] Gammon W, Malyarenko D, Kraft O, Hoatson G, Reilly A, Holloway B. Hard and elastic amorphous carbon nitride thin films studied by ^{13}C nuclear magnetic resonance spectroscopy. Phys Rev B 2002;66:153402.
[415] Binner J, Zhang Y. Characterization of silicon carbide and silicon powders by XPS and zeta potential measurement. J Mater Sci Lett 2001;20:123–6.
[416] Majumdar A, Das G, Patel N, Mishra P, Ghose D, Hippler R. Microstructural and chemical evolution of–CH_3-incorporated (low-k) SiCO (H) films prepared by dielectric barrier discharge plasma. J Electrochem Soc 2008;155:D22–6.
[417] Zhao W, Shao G, Han S, Cai C, Liu X, Sun M, et al. Facile preparation of ultralight polymer-derived SiOCN ceramic aerogels with hierarchical pore structure. J Am Ceram Soc 2019;102:2316–24.
[418] Han M, Yin X, Duan W, Ren S, Zhang L, Cheng L. Hierarchical graphene/SiC nanowire networks in polymer-derived ceramics with enhanced electromagnetic wave absorbing capability. J Eur Ceram Soc 2016;36:2695–703.
[419] Li YL, Kroke E, Riedel R, Fasel C, Gervais C, Babonneau F. Thermal cross-linking and pyrolytic conversion of poly (ureamethylvinyl) silazanes to silicon-based ceramics. Appl Organomet Chem 2001;15:820–32.
[420] Babonneau F, Thorne K, Mackenzie J. Dimethyldiethoxysilane/tetraethoxysilane copolymers: precursors for the silicon-carbon-oxygen system. Chem Mater 1989;1:554–8.
[421] Belot V, Corriu R, Leclercq D, Mutin P, Vioux A. Thermal redistribution reactions in crosslinked polysiloxanes. J Polym Sci, Part A: Polym Chem 1992;30:613–23.
[422] Maniette Y, Oberlin A. TEM characterization of some crude or air heat-treated SiC Nicalon fibres. J Mater Sci 1989;24:3361–70.
[423] Cordelair J, Greil P. Electrical conductivity measurements as a microprobe for structure transitions in polysiloxane derived Si-O-C ceramics. J Eur Ceram Soc 2000;20:1947–57.
[424] Li H, Zhang L, Cheng L, Wang Y, Yu Z, Huang M, et al. Polymer-ceramic conversion of a highly branched liquid polycarbosilane for SiC-based ceramics. J Mater Sci 2008;43:2806–11.
[425] Hojamberdiev M, Prasad RM, Morita K, Zhu Y, Schiavon MA, Gurlo A, et al. Template-free synthesis of polymer-derived mesoporous SiOC/TiO_2 and SiOC/N-doped TiO_2 ceramic composites for application in the removal of organic dyes from contaminated water. Appl Catal B: Environ 2012;115:303–13.
[426] Grierson DS, Sumant A, Konicek A, Friedmann T, Sullivan J, Carpick RW. Thermal stability and rehybridization of carbon bonding in tetrahedral amorphous carbon. J Appl Phys 2010;107:033523.
[427] Ferrari A, Robertson J. Resonant Raman spectroscopy of disordered, amorphous, and diamondlike carbon. Phys Rev B 2001;64:075414.
[428] Varga T, Navrotsky A, Moats JL, Morcos RM, Poli F, Müller K, et al. Thermodynamically stable $Si_xO_yC_z$ polymer-like amorphous ceramics. J Am Ceram Soc 2007;90:3213–9.
[429] Morcos RM, Navrotsky A, Varga T, Ahn D, Saha A, Poli F, et al. Thermodynamically stable $Si_wC_xN_yO_z$ polymer-like, amorphous ceramics made from organic precursors. J Am Ceram Soc 2008;91:2391–3.
[430] Gao Y, Widgeon SJ, Tran TB, Tavakoli AH, Mera G, Sen S, et al. Effect of demixing and coarsening on the energetics of poly(boro)silazane-derived amorphous Si-(B-)C-N ceramics. Scripta Mater 2013;69:347–50.
[431] Tavakoli AH, Golczewski JA, Bill J, Navrotsky A. Effect of boron on the thermodynamic stability of amorphous polymer-derived Si(B)CN ceramics. Acta Mater 2012;60:4514–22.
[432] Morcos RM, Navrotsky A, Varga T, Blum Y, Ahn D, Poli F, et al. Energetics of $Si_xO_yC_z$ polymer-derived ceramics prepared under varying conditions. J Am Ceram Soc 2008;91:2969–74.
[433] Shah SR, Raj R. Mechanical properties of a fully dense polymer derived ceramic made by a novel pressure casting process. Acta Mater 2002;50:4093–103.
[434] Saha A, Raj R. Crystallization maps for SiCO amorphous ceramics. J Am Ceram Soc 2007;90:578–83.
[435] Friess M, Bill J, Golczewski J, Zimmermann A, Aldinger F, Riedel R, et al. Crystallization of polymer-derived silicon carbonitride at 1873 K under nitrogen overpressure. J Am Ceram Soc 2002;85:2587–9.
[436] Schmidt H, Borchardt G, Müller A, Bill J. Formation kinetics of crystalline Si_3N_4/SiC composites from amorphous Si-C-N ceramics. J Non-Cryst Solids 2004;341:133–40.
[437] Laine RM, Babonneau F, Blowhowiak KY, Kennish RA, Rahn JA, Exarhos GJ, et al. The evolutionary process during pyrolytic transformation of poly (n-methylsilazane) from a preceramic polymer into an amorphous silicon nitride/carbon composite. J Am Ceram Soc 1995;78:137–45.
[438] Colombo P, Paulson TE, Pantano CG. Synthesis of silicon carbide thin films with polycarbosilane (PCS). J Am Ceram Soc 1997;80:2333–40.
[439] Kurtenbach D, Martin H-P, Müller E, Roewer G, Hoell A. Crystallization of polymer derived silicon carbide materials. J Eur Ceram Soc 1998;18:1885–91.
[440] Liu X, Li YL, Hou F. Fabrication of SiOC ceramic microparts and patterned structures from polysiloxanes via liquid cast and pyrolysis. J Am Ceram Soc 2009;92:49–53.
[441] Renlund GM, Prochazka S, Doremus RH. Silicon oxycarbide glasses: Part II. Structure and properties. J Mater Res 1991;6:2723–34.
[442] Bois L, Maquet J, Babonneau F, Bahloul D. Structural characterization of sol-gel derived oxycarbide glasses. 2. Study of the thermal stability of the silicon oxycarbide phase. Chem Mater 1995;7:975–81.
[443] Ainslie N, Morelock C, Turnbull D. Devitrification kinetics of fused silica. NY: General Electric Research Lab Schenectady; 1972.
[444] Modena S, Soraru GD, Blum Y, Raj R. Passive oxidation of an effluent system: the case of polymer-derived SiCO. J Am Ceram Soc 2005;88:339–45.
[445] Turnbull D, Fisher JC. Rate of nucleation in condensed systems. J Chem Phys 1949;17:71–3.
[446] Elmer TH, Meissner HE. Increase of annealing point of 96% SiO_2 glass on incorporation of carbon. J Am Ceram Soc 1976;59:206–9.
[447] Pantano CG, Singh AK, Zhang H. Silicon oxycarbide glasses. J Sol-Gel Sci Technol 1999;14:7–25.
[448] Raj R, Riedel R, Soraru GD. Introduction to the special topical issue on ultrahigh-temperature polymer-derived ceramics. J Am Ceram Soc 2001;84:2158–9.
[449] Riedel R, Kroke E, Greiner A, Gabriel AO, Ruwisch L, Nicolich J, et al. Inorganic solid-state chemistry with main group element carbodiimides. Chem Mater 1998;10:2964–79.
[450] Motz G, Bordia RK. Processing, structure and properties of ceramic fibers. Handbook of textile fibre structure. Elsevier; 2009. p. 378–424.
[451] Tanaka T, Shibayama S, Takeda M, Yokoyama A. Recent progress of Hi-Nicalon type S development. In: 27th Annual Cocoa Beach Conference on Advanced Ceramics and Composites: B: Ceramic Engineering and Science Proceedings: Wiley Online Library; 2003. p. 217–23.
[452] Chollon G, Pailler R, Naslain R, Laanani F, Monthioux M, Olry P. Thermal stability of a PCS-derived SiC fibre with a low oxygen content (Hi-Nicalon). J Mater Sci 1997;32:327–47.
[453] Sorarù GD, Kundanati L, Santhosh B, Pugno N. Influence of free carbon on the Young's modulus and hardness of polymer-derived silicon oxycarbide glasses. J Am Ceram Soc 2019;102:907–13.
[454] Rouxel T, Massouras G, Sorarù G-D. High temperature behavior of a gel-derived SiOC glass: elasticity and viscosity. J Sol-Gel Sci Technol 1999;14:87–94.
[455] Sorarù GD, Dallapiccola E, D'Andrea G. Mechanical characterization of sol-gel-derived silicon oxycarbide glasses. J Am Ceram Soc 1996;79:2074–80.
[456] Moysan C, Riedel R, Harshe R, Rouxel T, Augereau F. Mechanical characterization of a polysiloxane-derived SiOC glass. J Eur Ceram Soc 2007;27:397–403.
[457] Rouxel T, Soraru GD, Vicens J. Creep viscosity and stress relaxation of gel-derived silicon oxycarbide glasses. J Am Ceram Soc 2001;84:1052–8.
[458] Galusek D, Riley FL, Riedel R. Nanoindentation of a polymer-derived amorphous silicon carbonitride ceramic. J Am Ceram Soc 2001;84:1164–6.
[459] Janakiraman N, Burghard Z, Aldinger F. Fracture toughness evaluation of precursor-derived Si-C-N ceramics using the crack opening displacement approach. J Non-Cryst Solids 2009;355:2102–13.
[460] Janakiraman N, Aldinger F. Fracture in precursor-derived Si-C-N ceramics-analysis of crack roughness and damage mechanisms. J Non-Cryst Solids 2009;355:2114–21.
[461] Janakiraman N, Aldinger F. Indentation analysis of elastic and plastic deformation of precursor-derived Si-C-N ceramics. J Eur Ceram Soc 2010;30:775–85.
[462] Janakiraman N, Aldinger F. Yielding, strain hardening, and creep under nanoindentation of precursor-derived Si–C–N ceramics. J Am Ceram Soc 2010;93:821–9.
[463] Klausmann A, Morita K, Johanns KE, Fasel C, Durst K, Mera G, et al. Synthesis and high-temperature evolution of polysilylcarbodiimide-derived SiCN ceramic coatings. J Eur Ceram Soc 2015;35:3771–80.

[464] An L, Riedel R, Konetschny C, Kleebe HJ, Raj R. Newtonian viscosity of amorphous silicon carbonitride at high temperature. J Am Ceram Soc 1998;81:1349–52.
[465] Riedel R, Ruswisch LM, An L, Raj R. Amorphous silicoboron carbonitride ceramic with very high viscosity at temperatures above 1500 °C. J Am Ceram Soc 1998;81:3341–4.
[466] Wan J, Duan RG, Gasch MJ, Mukherjee AK. Highly creep-resistant silicon nitride/silicon carbide nano–nano composites. J Am Ceram Soc 2006;89:274–80.
[467] Kousaalya AB, Kumar R, Sridhar B. Thermal conductivity of precursor derived Si-B-C-N ceramic foams using Metroxylon sagu as sacrificial template. Ceram Int 2015;41:1163–70.
[468] Hwang Y, Ahn K, Kim J. Silicon carbonitride covered SiC composites for enhanced thermal conductivity and electrical insulation. Appl Therm Eng 2014;70:600–8.
[469] Barroso GS, Krenkel W, Motz G. Low thermal conductivity coating system for application up to 1000 °C by simple PDC processing with active and passive fillers. J Eur Ceram Soc 2015;35:3339–48.
[470] Nishimura T, Haug R, Bill J, Thurn G, Aldinger F. Mechanical and thermal properties of Si–C–N material from polyvinylsilazane. J Mater Sci 1998;33:5237–41.
[471] Bergero L, Sglavo VM, Soraru GD. Processing and thermal shock resistance of a polymer-derived $MoSi_2$/SiCO ceramic composite. J Am Ceram Soc 2005;88:3222–5.
[472] Eom J-H, Kim Y-W, Kim KJ, Seo W-S. Improved electrical and thermal conductivities of polysiloxane-derived silicon oxycarbide ceramics by barium addition. J Eur Ceram Soc 2018;38:487–93.
[473] Qiu L, Li Y, Zheng X, Zhu J, Tang D, Wu J, et al. Thermal-conductivity studies of macro-porous polymer-derived SiOC ceramics. Int J Thermophys 2014;35:76–89.
[474] Yang J, Sprengard J, Ju L, Hao A, Saei M, Liang R, et al. Three-dimensional-linked carbon fiber-carbon nanotube hybrid structure for enhancing thermal conductivity of silicon carbonitride matrix composites. Carbon 2016;108:38–46.
[475] Gurlo A, Ionescu E, Riedel R, Clarke DR. The thermal conductivity of polymer-derived amorphous Si-O-C compounds and nano-composites. J Am Ceram Soc 2016;99:281–5.
[476] Mazo MA, Tamayo A, Caballero AC, Rubio J. Electrical and thermal response of silicon oxycarbide materials obtained by spark plasma sintering. J Eur Ceram Soc 2017;37:2011–20.
[477] Zhou Y, Hirao K, Watari K, Yamauchi Y, Kanzaki S. Thermal conductivity of silicon carbide densified with rare-earth oxide additives. J Eur Ceram Soc 2004;24:265–70.
[478] Snead L, Zinkle S. Structural relaxation in amorphous silicon carbide. Nucl Instrum Methods Phys Res, Sect B 2002;191:497–503.
[479] Bullen AJ, O'Hara KE, Cahill DG, Monteiro O, von Keudell A. Thermal conductivity of amorphous carbon thin films. J Appl Phys 2000;88:6317–20.
[480] Rahman A, Zunjarrao SC, Singh RP. Effect of degree of crystallinity on elastic properties of silicon carbide fabricated using polymer pyrolysis. J Eur Ceram Soc 2016;36:3285–92.
[481] Lee S, Fourcade J, Latta R, Solomon A. Polymer impregnation and pyrolysis process development for improving thermal conductivity of SiC_p/SiC-PIP matrix fabrication. Fusion Eng Des 2008;83:713–9.
[482] Lee J-S, Yano T. Fabrication of short-fiber-reinforced SiC composites by polycarbosilane infiltration. J Eur Ceram Soc 2004;24:25–31.
[483] Piat R, Schnack E. Identification of coefficients of thermal expansion of pyrolytic carbon with different texture degrees. Key Eng Mater: Trans Tech Publ; 2003. p. 333–8.
[484] Li Z, Bradt R. Thermal expansion of the cubic (3C) polytype of SiC. J Mater Sci 1986;21:4366–8.
[485] Reitz E, Schell KG, Bucharsky EC, Oberacker R, Hoffmann MJ. Precursor derived SiOC/$MoSi_2$-composites for diesel glow plugs: preparation and high temperature properties. J Ceram Soc Jpn 2016;124:1017–22.
[486] Fedorova A, Scheffler M. Polymer derived ceramics with negative thermal expansion fillers: zirconium tungstate. Adv Eng Mater 2019.
[487] Fedorova A, Michelsen L, Scheffler M. Polymer-derived ceramic tapes with small and negative thermal expansion coefficients. J Eur Ceram Soc 2018;38:719–25.
[488] Colombo P, Hellmann JR, Shelleman DL. Thermal shock behavior of silicon oxycarbide foams. J Am Ceram Soc 2002;85:2306–12.
[489] Wen Q, Luan X, Wang L, Xu X, Ionescu E, Riedel R. Laser ablation behavior of SiHfC-based ceramics prepared from a single-source precursor: Effects of Hf-incorporation into SiC. J Eur Ceram Soc 2019.
[490] Li D, Yang Z, Jia D, Wu D, Zhu Q, Liang B, et al. Microstructure, oxidation and thermal shock resistance of graphene reinforced SiBCN ceramics. Ceram Int 2016;42:4429–44.
[491] Bharadwaj L, Fan Y, Zhang L, Jiang D, An L. Oxidation behavior of a fully dense polymer-derived amorphous silicon carbonitride ceramic. J Am Ceram Soc 2004;87:483–6.
[492] Chollon G. Oxidation behaviour of ceramic fibres from the Si-C-N-O system and related sub-systems. J Eur Ceram Soc 2000;20:1959–74.
[493] Baldus P, Jansen M, Sporn D. Ceramic fibers for matrix composites in high-temperature engine applications. Science 1999;285:699–703.
[494] Bernard S, Cornu D, Miele P, Weinmann M, Aldinger F. Polyborosilazane-derived ceramic fibers in the Si-B-C-N quaternary system for high-temperature applications. Mech Propert Perform Eng Ceram Compos: Ceram Eng Sci Proc 2005;26:35–42.
[495] Wen Q, Riedel R, Ionescu E. Significant improvement of the short-term high-temperature oxidation resistance of dense monolithic HfC/SiC ceramic nanocomposites upon incorporation of Ta. Corros Sci 2018;145:191–8.
[496] Butchereit E, Nickel KG, Müller A. Precursor-derived Si-B-C-N ceramics: oxidation kinetics. J Am Ceram Soc 2001;84:2184–8.
[497] Saha A, Shah SR, Raj R. Oxidation behavior of SiCN-ZrO_2 fiber prepared from alkoxide-modified silazane. J Am Ceram Soc 2004;87:1556–8.
[498] Raj R, An L, Shah S, Riedel R, Fasel C, Kleebe HJ. Oxidation kinetics of an amorphous silicon carbonitride ceramic. J Am Ceram Soc 2001;84:1803–10.
[499] Colombo P, Hellmann JR. Ceramic foams from preceramic polymers. Mater Res Innovations 2002;6:260–72.
[500] Chollon G. Oxidation behaviour of polymer-derived ceramics. DEStech Publications; 2009.
[501] Bahloul D, Pereira M, Goursat P. Silicon carbonitride derived from an organometallic precursor: influence of the microstructure on the oxidation behaviour. Ceram Int 1992;18:1–9.
[502] Bahloul D, Pereira M, Goursat P. Preparation of silicon carbonitrides from an organosilicon polymer: II, thermal behavior at high temperatures under argon. J Am Ceram Soc 1993;76:1163–8.
[503] Bahloul D, Goursat P, Lavedrine A. Influence of microstructural changes on the oxidation resistance of silicon carbonitrides derived from a polyvinylsilazane. J Eur Ceram Soc 1993;11:63–8.
[504] Wen Q, Riedel R, Ionescu E. Solid-solution effects on the high-temperature oxidation behavior of polymer-derived (Hf, Ta)C/SiC and (Hf, Ti)C/SiC ceramic nanocomposites. Adv Eng Mater 2018.
[505] Brewer CM, Bujalski DR, Parent VE, Su K, Zank GA. Insights into the oxidation chemistry of SiOC ceramics derived from silsesquioxanes. J Sol-Gel Sci Technol 1999;14:49–68.
[506] Ishikawa T, Kohtoku Y, Kumagawa K, Yamamura T, Nagasawa T. High-strength alkali-resistant sintered SiC fibre stable to 2,200 C. Nature 1998;391:773.
[507] Nguyen VL, Proust V, Quievryn C, Bernard S, Miele P, Soraru GD. Processing, mechanical characterization, and alkali resistance of siliconboronoxycarbide (SiBOC) glass fibers. J Am Ceram Soc 2014;97:3143–9.
[508] Jothi S, Ravindran S, Kumar R. Corrosion of polymer-derived ceramics in hydrofluoric acid and sodium salts. Adv Sci Technol Trans Tech Publ 2014:82–7.
[509] Jothi S, Ravindran S, Neelakantan L, Kumar R. Corrosion behavior of polymer-derived SiHfCN(O) ceramics in salt and acid environments. Ceram Int 2015;41:10659–69.
[510] An L, Wang Y, Bharadwaj L, Zhang L, Fan Y, Jiang D, et al. Silicoaluminum carbonitride with anomalously high resistance to oxidation and hot corrosion. Adv Eng Mater 2004;6:337–40.
[511] Linck C, Ionescu E, Papendorf B, Galuskova D, Galusek D, Ŝajgalík P, et al. Corrosion behavior of silicon oxycarbide-based ceramic nanocomposites under hydrothermal conditions. Int J Mater Res 2012;103:31–9.
[512] Kamiya K, Ohya M, Yoko T. Nitrogen-containing SiO_2 glass fibers prepared by ammonolysis of gels made from silicon alkoxides. J Non-Cryst Solids

1986;83:208–22.
[513] Cross T, Prasad S, Raj R. Friction and wear behavior of silicon carbonitride processed from the polymer-derived ceramic route. World Tribology Congress III: American Society of Mechanical Engineers; 2005. p. 473–4.
[514] Seitz J, Joachim B, Aldinger F, Naerheim Y. Process for producing a Si/C/N ceramic body. Google Patents; 2002.
[515] He J, Cao Y, Li Z, Wang Y. Study of tribological properties of polymer derived ZrB_2-SiC ceramics. Ceram Int 2018;44:15627–30.
[516] Pan J, Yan X, Cheng X, Xu D, Lu Q. Preparation and tribological properties of hierarchical porous SiOC/BN composites from wood powder and polysiloxane precursor. Ceram Int 2015;41:10102–9.
[517] Raj R, Shah SR. Polymer-derived nanocomposite lubricant for ultra-low wear applications. Google Patents; 2010.
[518] Archard J. Contact and rubbing of flat surfaces. J Appl Phys 1953;24:981–8.
[519] Hokao M, Hironaka S, Suda Y, Yamamoto Y. Friction and wear properties of graphite/glassy carbon composites. Wear 2000;237:54–62.
[520] Bryant P, Gutshall P, Taylor L. A study of mechanisms of graphite friction and wear. Wear 1964;7:118–26.
[521] Buckley DH, Miyoshi K. Friction and wear of ceramics. Wear 1984;100:333–53.
[522] Bakumov V, Blugan G, Roos S, Graule T, Fakhfouri V, Grossenbacher J, et al. Mechanical and tribological properties of polymer-derived Si/C/N sub-millimetre thick miniaturized components fabricated by direct casting. J Eur Ceram Soc 2012;32:1759–67.
[523] Hoche H, Allebrandt D, Bruns M, Riedel R, Fasel C. Relationship of chemical and structural properties with the tribological behavior of sputtered SiCN films. Surf Coat Technol 2008;202:5567–71.
[524] Ahn D, Raj R. Cyclic stability and C-rate performance of amorphous silicon and carbon based anodes for electrochemical storage of lithium. J Power Sources 2011;196:2179–86.
[525] Li Y, Yu Y, San H, Wang Y, An L. Wireless passive polymer-derived SiCN ceramic sensor with integrated resonator/antenna. Appl Phys Lett. 2013;103:163505.
[526] Yao R, Feng Z, Yu Y, Li S, Chen L, Zhang Y. Synthesis and characterization of continuous freestanding silicon carbide films with polycarbosilane (PCS). J Eur Ceram Soc 2009;29:2079–85.
[527] Wang K, Ma B, Wang Y, An L. Complex impedance spectra of polymer-derived silicon oxycarbides. J Am Ceram Soc 2013;96:1363–5.
[528] Karakuscu A, Guider R, Pavesi L, Soraru GD. White luminescence from sol-gel-derived SiOC thin films. J Am Ceram Soc 2009;92:2969–74.
[529] Menapace I, Mera G, Riedel R, Erdem E, Eichel R-A, Pauletti A, et al. Luminescence of heat-treated silicon-based polymers: promising materials for LED applications. J Mater Sci 2008;43:5790–6.
[530] Narisawa M, Kawai T, Watase S, Matsukawa K, Dohmaru T, Okamura K, et al. Long-lived photoluminescence in amorphous Si-O-C(-H) ceramics derived from polysiloxanes. J Am Ceram Soc 2012;95:3935–40.
[531] Shen C, Barrios E, Zhai L. Bulk polymer-derived ceramic composites of graphene oxide. ACS Omega 2018;3:4006–16.
[532] Yajima S. Special heat-resisting materials from organometallic polymers. Am Ceram Soc Bull Am Ceram Soc Bull 1983;62:893.
[533] Grossenbacher J, Gullo MR, Dalcanale F, Blugan G, Kuebler J, Lecaudé S, et al. Cytotoxicity evaluation of polymer-derived ceramics for pacemaker electrode applications. J Biomed Mater Res A 2015;103:3625–32.
[534] Ryu HY, Wang Q, Raj R. Ultrahigh-temperature semiconductors made from polymer-derived ceramics. J Am Ceram Soc 2010;93:1668–76.
[535] Ramakrishnan P, Wang Y, Balzar D, An L, Haluschka C, Riedel R, et al. Silicoboron-carbonitride ceramics: a class of high-temperature, dopable electronic materials. Appl Phys Lett 2001;78:3076–8.
[536] Hermann AM, Wang YT, Ramakrishnan PA, Balzar D, An L, Haluschka C, et al. Structure and electronic transport properties of Si-(B)-C-N ceramics. J Am Ceram Soc 2001;84:2260–4.
[537] Wang K, Li X, Ma B, Wang Y, Zhang L, An L. On electronic structure of polymer-derived amorphous silicon carbide ceramics. Appl Phys Lett 2014;104:221902.
[538] Chen Y, Yang X, Cao Y, An L. Effect of pyrolysis temperature on the electric conductivity of polymer-derived silicoboron carbonitride. J Eur Ceram Soc 2014;34:2163–7.
[539] Colombo P, Gambaryan-Roisman T, Scheffler M, Buhler P, Greil P. Conductive ceramic foams from preceramic polymers. J Am Ceram Soc 2001;84:2265–8.
[540] McLachlan D. An equation for the conductivity of binary mixtures with anisotropic grain structures. J Phys C Sol Stat Phys 1987;20:865.
[541] Carmona F, Canet R, Delhaes P. Piezoresistivity of heterogeneous solids. J Appl Phys 1987;61:2550–7.
[542] Balberg I. Tunneling and nonuniversal conductivity in composite materials. Phys Rev Lett 1987;59:1305.
[543] McLachlan DS, Blaszkiewicz M, Newnham RE. Electrical resistivity of composites. J Am Ceram Soc 1990;73:2187–203.
[544] Ueda N, Taya M. Prediction of the electrical conductivity of two-dimensionally misoriented short fiber composites by a percolation model. J Appl Phys 1986;60:459–61.
[545] Jing X, Zhao W, Lan L. The effect of particle size on electric conducting percolation threshold in polymer/conducting particle composites. J Mater Sci Lett 2000;19:377–9.
[546] Hu T, Li X, Pu W, Chu Z, Li G, Wang Q. Models proposed to explain the electrical conductivity of polymer-derived silicon carbide fibers. J Am Ceram Soc 2017;100:167–75.
[547] Mott NF. Conduction in non-crystalline materials: III. Localized states in a pseudogap and near extremities of conduction and valence bands. Philos Mag 1969;19:835–52.
[548] Haluschka C, Engel C, Riedel R. Silicon carbonitride ceramics derived from polysilazanes Part II. Investigation of electrical properties. J Eur Ceram Soc 2000;20:1365–74.
[549] Chollon G, Pailler R, Naslain R, Olry P. Correlation between microstructure and mechanical behaviour at high temperatures of a SiC fibre with a low oxygen content (Hi–Nicalon). J Mater Sci 1997;32:1133–47.
[550] Haluschka C, Engel C, Riedel R. Electrical properties of ternary Si-CN ceramics. MRS Online Proceed Libra Arch 1996;435.
[551] Chen Y, Yang F, An L. On electric conduction of amorphous silicon carbonitride derived from a polymeric precursor. Appl Phys Lett 2013;102:231902.
[552] Shao G, Peng W, Ma C, Zhao W, Guo J, Feng Y, et al. Enhanced electric conductivity of polymer-derived SiCN ceramics by microwave post-treatment. J Am Ceram Soc 2017;100:842–7.
[553] Ma B, Wang Y, Wang K, Li X, Liu J, An L. Frequency-dependent conductive behavior of polymer-derived amorphous silicon carbonitride. Acta Mater 2015;89:215–24.
[554] Cao Y, Gao Y, An L. Impedance spectroscopy study on polymer-derived amorphous SiAlCO. J Am Ceram Soc 2017;100:1481–5.
[555] Ma C, Shao G, Jiang J, Liu W, Wang H, Lu H, et al. Temperature dependent AC electric conduction of polymer-derived SiAlCN ceramics. Ceram Int 2018;44:8461–6.
[556] Ma B, Wang Y. Fabrication of dense polymer-derived silicon carbonitride ceramic bulks by precursor infiltration and pyrolysis processes without losing piezoresistivity. J Am Ceram Soc 2018;101:2752–9.
[557] Liebau-Kunzmann V, Fasel C, Kolb R, Riedel R. Lithium containing silazanes as precursors for SiCN: Li ceramics-a potential material for electrochemical applications. J Eur Ceram Soc 2006;26:3897–901.
[558] Dahn JR, Eguchi K, Wilson AM, Xing W, Zank GA. Electrodes for lithium ion batteries using polysiloxanes. Google Patents; 1998.
[559] Su D, Li YL, Feng Y, Jin J. Electrochemical properties of polymer-derived SiCN materials as the anode in lithium ion batteries. J Am Ceram Soc 2009;92:2962–8.
[560] Sanchez-Jimenez PE, Raj R. Lithium insertion in polymer-derived silicon oxycarbide ceramics. J Am Ceram Soc 2010;93:1127–35.
[561] Fukui H, Ohsuka H, Hino T, Kanamura K. A Si-O-C composite anode: high capability and proposed mechanism of lithium storage associated with micro-structural characteristics. ACS Appl Mater Inter 2010;2:998–1008.
[562] Ahn D, Raj R. Thermodynamic measurements pertaining to the hysteretic intercalation of lithium in polymer-derived silicon oxycarbide. J Power Sources 2010;195:3900–6.
[563] Graczyk-Zajac M, Fasel C, Riedel R. Polymer-derived-SiCN ceramic/graphite composite as anode material with enhanced rate capability for lithium ion batteries. J Power Sources 2011;196:6412–8.
[564] Bhandavat R, Singh G. Improved electrochemical capacity of precursor-derived Si(B)CN-carbon nanotube composite as Li-ion battery anode. ACS Appl Mater

Inter. 2012;4:5092–7.
[565] Wilamowska M, Graczyk-Zajac M, Riedel R. Composite materials based on polymer-derived SiCN ceramic and disordered hard carbons as anodes for lithium-ion batteries. J Power Sources 2013;244:80–6.
[566] Baek S-H, Reinold LM, Graczyk-Zajac M, Riedel R, Hammerath F, Büchner B, et al. Lithium dynamics in carbon-rich polymer-derived SiCN ceramics probed by nuclear magnetic resonance. J Power Sources 2014;253:342–8.
[567] Kaspar J, Graczyk-Zajac M, Choudhury S, Riedel R. Impact of the electrical conductivity on the lithium capacity of polymer-derived silicon oxycarbide (SiOC) ceramics. Electrochim Acta 2016;216:196–202.
[568] Kaspar J, Graczyk-Zajac M, Riedel R. Lithium insertion into carbon-rich SiOC ceramics: Influence of pyrolysis temperature on electrochemical properties. J Power Sources 2013;244:450–5.
[569] Pradeep V, Graczyk-Zajac M, Wilamowska M, Riedel R, Soraru G. Influence of pyrolysis atmosphere on the lithium storage properties of carbon-rich polymer derived SiOC ceramic anodes. Solid State Ionics 2014;262:22–4.
[570] Reinold LM, Graczyk-Zajac M, Gao Y, Mera G, Riedel R. Carbon-rich SiCN ceramics as high capacity/high stability anode material for lithium-ion batteries. J Power Sources 2013;236:224–9.
[571] Shen J, Ahn D, Raj R. C-rate performance of silicon oxycarbide anodes for Li^+ batteries enhanced by carbon nanotubes. J Power Sources 2011;196:2875–8.
[572] Graczyk-Zajac M, Reinold L, Kaspar J, Sasikumar P, Soraru G-D, Riedel R. New insights into understanding irreversible and reversible lithium storage within SiOC and SiCN ceramics. Nanomaterials 2015;5:233–45.
[573] Fukui H, Ohsuka H, Hino T, Kanamura K. Polysilane/acenaphthylene blends toward Si-O-C composite anodes for rechargeable lithium-ion batteries. J Electrochem Soc 2011;158:A550–5.
[574] Fukui H, Eguchi K, Ohsuka H, Hino T, Kanamura K. Structures and lithium storage performance of Si-O-C composite materials depending on pyrolysis temperatures. J Power Sources 2013;243:152–8.
[575] Graczyk-Zajac M, Toma L, Fasel C, Riedel R. Carbon-rich SiOC anodes for lithium-ion batteries: Part I. Influence of material UV-pre-treatment on high power properties. Solid State Ionics 2012;225:522–6.
[576] Kaspar J, Graczyk-Zajac M, Riedel R. Carbon-rich SiOC anodes for lithium-ion batteries: Part II. Role of thermal cross-linking. Solid State Ionics 2012;225:527–31.
[577] Pradeep V, Ayana D, Graczyk-Zajac M, Soraru G, Riedel R. High rate capability of SiOC ceramic aerogels with tailored porosity as anode materials for Li-ion batteries. Electrochim Acta 2015;157:41–5.
[578] Pradeep V, Graczyk-Zajac M, Riedel R, Soraru G. New insights in to the lithium storage mechanism in polymer derived SiOC anode materials. Electrochim Acta 2014;119:78–85.
[579] Xing W, Wilson A, Eguchi K, Zank G, Dahn J. Pyrolyzed polysiloxanes for use as anode materials in lithium-ion batteries. J Electrochem Soc 1997;144:2410–6.
[580] Besenhard JO. Handbook of battery materials. John Wiley & Sons; 2008.
[581] Graczyk-Zajac M, Vrankovic D, Waleska P, Hess C, Sasikumar PV, Lauterbach S, et al. The Li-storage capacity of SiOC glasses with and without mixed silicon oxycarbide bonds. J Mater Chem A 2018;6:93–103.
[582] Haaks M, Kaspar J, Franz A, Graczyk-Zajac M, Riedel R, Vogel M. ^{7}Li NMR studies of lithium ion dynamics in polymer-derived silicon oxycarbide ceramics. Solid State Ionics 2016;287:28–35.
[583] Liao N, Zheng B, Zhou H, Xue W. Lithiation behavior of high capacity SiCO anode material for lithium-ion battery: a first principle study. Electrochim Acta 2015;156:115–20.
[584] Liao N, Zheng B, Zhou H, Xue W. Effect of carbon segregation on performance of inhomogeneous $SiC_yO_{6/5}$ as anode materials for lithium-ion battery: a first-principles study. J Power Sources 2016;334:39–43.
[585] Liao N, Zheng B, Zhang M, Xue W. Atomic investigation on reversible lithium storage in amorphous silicon oxycarbide as a high power anode material. J Mater Chem A 2016;4:12328–33.
[586] Kroll P. Tracing reversible and irreversible Li insertion in SiCO ceramics with modeling and ab-initio simulations. MRS Online Proceed Libra Arch 2011;1313.
[587] Liu G, Kaspar J, Reinold LM, Graczyk-Zajac M, Riedel R. Electrochemical performance of DVB-modified SiOC and SiCN polymer-derived negative electrodes for lithium-ion batteries. Electrochim Acta 2013;106:101–8.
[588] Yusoff A, Abdullah M, Ahmad S, Jusoh S, Mansor A, Hamid S. Electromagnetic and absorption properties of some microwave absorbers. J Appl Phys 2002;92:876–82.
[589] Wen Q. Single-source-precursor synthesis and properties of SiMC (N) ceramic nanocomposites (M= Hf, Ta, HfTa). Technische Universität Darmstadt; 2017.
[590] Chen L, Yin X, Fan X, Chen M, Ma X, Cheng L, et al. Mechanical and electromagnetic shielding properties of carbon fiber reinforced silicon carbide matrix composites. Carbon 2015;95:10–9.
[591] Li X, Zhang L, Yin X, Yu Z. Mechanical and dielectric properties of porous Si_3N_4–SiC(BN) ceramic. J Alloys Compd 2010;490:L40–3.
[592] Qing Y, Zhou W, Huang S, Huang Z, Luo F, Zhu D. Microwave absorbing ceramic coatings with multi-walled carbon nanotubes and ceramic powder by polymer pyrolysis route. Compos Sci Technol 2013;89:10–4.
[593] Yu Z, Min H, Zhan J, Yang L. Preparation and dielectric properties of polymer-derived SiCTi ceramics. Ceram Int 2013;39:3999–4007.
[594] Ye F, Zhang L, Yin X, Zhang Y, Kong L, Liu Y, et al. Dielectric and microwave-absorption properties of SiC nanoparticle/SiBCN composite ceramics. J Eur Ceram Soc 2014;34:205–15.
[595] Duan W, Yin X, Li Q, Liu X, Cheng L, Zhang L. Synthesis and microwave absorption properties of SiC nanowires reinforced SiOC ceramic. J Eur Ceram Soc 2014;34:257–66.
[596] Mu Y, Zhou W, Hu Y, Qing Y, Luo F, Zhu D. Improvement of mechanical and dielectric properties of PIP-SiC_f/SiC composites by using Ti_3SiC_2 as inert filler. Ceram Int 2015;41:4199–206.
[597] Wang X, Mera G, Morita K, Ionescu E. Synthesis of polymer-derived graphene/silicon nitride-based nanocomposites with tunable dielectric properties. J Ceram Soc Jpn 2016;124:981–8.
[598] Duan W, Yin X, Ye F, Li Q, Han M, Liu X, et al. Synthesis and EMW absorbing properties of nano SiC modified PDC-SiOC. J Mater Chem C 2016;4:5962–9.
[599] Wang Y, Guo X, Feng Y, Lin X, Gong H. Wave absorbing performance of polymer-derived SiCN(Fe) ceramics. Ceram Int 2017;43:15551–5.
[600] Wang Y, Feng Y, Guo X, Liu Y, Gong H. Electromagnetic and wave absorbing properties of Fe-doped polymer-derived SiCN ceramics. RSC Adv 2017;7:46215–20.
[601] Zhang Q, Gou Y, Wang J, Wang H, Jian K, Wang Y. Preparation and characterization of polymer-derived Zr/Si/C multiphase ceramics and microspheres with electromagnetic wave absorbing capabilities. J Eur Ceram Soc 2017;37:1909–16.
[602] Liu X, Zhang L, Yin X, Ye F, Liu Y, Cheng L. The microstructure and electromagnetic wave absorption properties of near-stoichiometric SiC fibre. Ceram Int 2017;43:3267–73.
[603] Duan W, Yin X, Luo C, Kong J, Ye F, Pan H. Microwave-absorption properties of SiOC ceramics derived from novel hyperbranched ferrocene-containing polysiloxane. J Eur Ceram Soc 2017;37:2021–30.
[604] Li Q, Yin X, Duan W, Cheng L, Zhang L. Improved dielectric properties of PDCs-SiCN by in-situ fabricated nano-structured carbons. J Eur Ceram Soc 2017;37:1243–51.
[605] Guo X, Feng Y, Lin X, Liu Y, Gong H, Zhang Y. The dielectric and microwave absorption properties of polymer-derived SiCN ceramics. J Eur Ceram Soc 2018;38:1327–33.
[606] Wang P, Cheng L, Zhang L. Lightweight, flexible SiCN ceramic nanowires applied as effective microwave absorbers in high frequency. Chem Eng J 2018;338:248–60.
[607] Li Q, Yin X, Duan W, Kong L, Liu X, Cheng L, et al. Improved dielectric and electromagnetic interference shielding properties of ferrocene-modified polycarbosilane derived SiC/C composite ceramics. J Eur Ceram Soc 2014;34:2187–201.
[608] Wang Y, Xiao P, Zhou W, Luo H, Li Z, Chen W, et al. Microstructures, dielectric response and microwave absorption properties of polycarbosilane derived SiC

powders. Ceram Int 2018;44:3606–13.
[609] Li Q, Yin X, Zhang L, Cheng L. Effects of SiC fibers on microwave absorption and electromagnetic interference shielding properties of SiC_f/SiCN composites. Ceram Int 2016;42:19237–44.
[610] Mu Y, Zhou W, Wan F, Ding D, Hu Y, Luo F. High-temperature dielectric and electromagnetic interference shielding properties of SiC_f/SiC composites using Ti_3SiC_2 as inert filler. Compos Part A Appl Sci Manuf 2015;77:195–203.
[611] Li Q, Yin X, Duan W, Cheng L, Zhang L. Improved dielectric properties of PDCs-SiCN by in-situ fabricated nano-structured carbons. J Eur Ceram Soc. 2016.
[612] Wang P, Cheng L, Zhang L. One-dimensional carbon/SiC nanocomposites with tunable dielectric and broadband electromagnetic wave absorption properties. Carbon 2017;125:207–20.
[613] Wang P, Cheng L, Zhang Y, Zhang L. Synthesis of SiC nanofibers with superior electromagnetic wave absorption performance by electrospinning. J Alloys Compd 2017;716:306–20.
[614] Micheli D, Apollo C, Pastore R, Marchetti M. X-band microwave characterization of carbon-based nanocomposite material, absorption capability comparison and RAS design simulation. Compos Sci Technol 2010;70:400–9.
[615] Cao M-S, Song W-L, Hou Z-L, Wen B, Yuan J. The effects of temperature and frequency on the dielectric properties, electromagnetic interference shielding and microwave-absorption of short carbon fiber/silica composites. Carbon 2010;48:788–96.
[616] Luo C, Duan W, Yin X, Kong J. Microwave-absorbing polymer-derived ceramics from cobalt-coordinated poly (dimethylsilylene) diacetylenes. J Phys Chem C 2016;120:18721–32.
[617] Li Q, Yin X, Feng L. Dielectric properties of Si_3N_4-SiCN composite ceramics in X-band. Ceram Int 2012;38:6015–20.
[618] Ding D-H, Zhou W-C, Xuan Z, Fa L, Zhu D-M. Influence of pyrolysis temperature on structure and dielectric properties of polycarbosilane derived silicon carbide ceramic. T Nonferr Metal Soc 2012;22:2726–9.
[619] Mera G, Menapace I, Widgeon S, Sen S, Riedel R. Photoluminescence of as-synthesized and heat-treated phenyl-containing polysilylcarbodiimides: role of crosslinking and free carbon formation in polymer-derived ceramics. Appl Organomet Chem 2013;27:630–8.
[620] Cakmak H, Jansen M. Intrinsic photoluminescence properties of amorphous $Si_3B_3N_7$ ceramic. J Lumin 2010;130:2322–6.
[621] Cakmak H, Jansen M. Amorphous $Si_3B_3N_7$ ceramic as a versatile host for inorganic phosphor activators. Adv Funct Mater 2014;24:460–4.
[622] Karakuscu A, Guider R, Pavesi L, Sorarù GD. Broad-band tunable visible emission of sol–gel derived SiBOC ceramic thin films. Thin Solid Films 2011;519:3822–6.
[623] Wang Y, Jiang T, Zhang L, An L. Optical absorption in polymer-derived amorphous silicon oxycarbonitrides. J Am Ceram Soc 2009;92:3111–3.
[624] Soraru GD. Silicon oxycarbide glasses from gels. J Sol-Gel Sci Technol 1994;2:843–8.
[625] Bréquel H, Parmentier J, Walter S, Badheka R, Trimmel G, Masse S, et al. Systematic structural characterization of the high-temperature behavior of nearly stoichiometric silicon oxycarbide glasses. Chem Mater 2004;16:2585–98.
[626] Dire S, Borovin E, Narisawa M, Soraru GD. Synthesis and characterization of the first transparent silicon oxycarbide aerogel obtained through H_2 decarbonization. J Mater Chem A 2015;3:24405–13.
[627] Bachar A, Mercier C, Tricoteaux A, Leriche A, Follet C, Hampshire S. Bioactive oxynitride glasses: synthesis, structure and properties. J Eur Ceram Soc 2016;36:2869–81.
[628] Kousaalya AB, Zeng X, Karakaya M, Tritt T, Pilla S, Rao AM. Polymer-derived silicon oxycarbide ceramics as promising next-generation sustainable thermoelectrics. ACS Appl Mater Inter 2018;10:2236–41.
[629] Seifollahi Bazarjani M, Hojamberdiev M, Morita K, Zhu G, Cherkashinin G, Fasel C, et al. Visible light photocatalysis with c-WO_{3-x}/WO_3xH_2O nanoheterostructures in situ formed in mesoporous polycarbosilane-siloxane polymer. J Am Chem Soc 2013;135:4467–75.
[630] Hojamberdiev M, Prasad RM, Morita K, Schiavon MA, Riedel R. Polymer-derived mesoporous SiOC/ZnO nanocomposite for the purification of water contaminated with organic dyes. Micropor Mesopor Mater 2012;151:330–8.
[631] Pan J, Ren J, Xie Y, Wei X, Guan Y, Yan X, et al. Porous SiOC composites fabricated from preceramic polymers and wood powders for efficient dye adsorption and removal. Res Chem Intermed 2017;43:3813–32.
[632] Zeydanli D, Akman S, Vakifahmetoglu C. Polymer-derived ceramic adsorbent for pollutant removal from water. J Am Ceram Soc 2018;101:2258–65.
[633] Bruzzoniti MC, Appendini M, Rivoira L, Onida B, Del Bubba M, Jana P, et al. Polymer-derived ceramic aerogels as sorbent materials for the removal of organic dyes from aqueous solutions. J Am Ceram Soc 2018;101:821–30.
[634] Yu Z, Li S, Zhang P, Feng Y, Liu X. Polymer-derived mesoporous Ni/SiOC(H) ceramic nanocomposites for efficient removal of acid fuchsin. Ceram Int 2017;43:4520–6.
[635] Seifollahi Bazarjani M, Müller MM, Kleebe H-J, Jüttke Y, Voigt I, Baghaie Yazdi M, et al. High-temperature stability and saturation magnetization of superparamagnetic nickel nanoparticles in microporous polysilazane-derived ceramics and their gas permeation properties. ACS Appl Mater Inter 2014;6:12270–8.
[636] Schitco C, Bazarjani MS, Riedel R, Gurlo A. NH_3-assisted synthesis of microporous silicon oxycarbonitride ceramics from preceramic polymers: a combined N_2 and CO_2 adsorption and small angle X-ray scattering study. J Mater Chem A 2015;3:805–18.
[637] Jüttke Y, Richter H, Voigt I, Prasad RM, Bazarjani MS, Gurlo A, et al. Polymer derived ceramic membranes for gas separation. Chem Eng 2013;32..
[638] Zhuo R, Colombo P, Pantano C, Vogler EA. Silicon oxycarbide glasses for blood-contact applications. Acta Biomater 2005;1:583–9.
[639] Starý VR, Bačáková L, Horník J, Chmelík V. Bio-compatibility of the surface layer of pyrolytic graphite. Thin Solid Films 2003;433:191–8.
[640] Baldus H-P, Passing G, Scholz H, Sporn D, Jansen M, Göring J. Properties of amorphous SiBNC-ceramic fibres. Trans Tech Publ Key Eng Mater 1997:177–84.
[641] Evans A, Zok F. The physics and mechanics of fibre-reinforced brittle matrix composites. J Mater Sci 1994;29:3857–96.
[642] Ziegler G, Richter I, Suttor D. Fiber-reinforced composites with polymer-derived matrix: processing, matrix formation and properties. Compos Part A Appl Sci Manuf 1999;30:411–7.
[643] Ionescu E, Linck C, Fasel C, Müller M, Kleebe HJ, Riedel R. Polymer-derived SiOC/ZrO_2 ceramic nanocomposites with excellent high-temperature stability. J Am Ceram Soc 2010;93:241–50.
[644] Ionescu E, Papendorf B, Kleebe HJ, Riedel R. Polymer-derived silicon oxycarbide/hafnia ceramic nanocomposites. Part II: Stability toward decomposition and microstructure evolution at T ≫ 1000 °C. J Am Ceram Soc 2010;93:1783–9.
[645] Proust V, Bechelany MC, Ghisleni R, Beaufort M-F, Miele P, Bernard S. Polymer-derived Si-C-Ti systems: From titanium nanoparticle-filled polycarbosilanes to dense monolithic multi-phase components with high hardness. J Eur Ceram Soc 2016;36:3671–9.
[646] Website Starfire Systems Inc.: http://www.starfiresystems.com.
[647] Gadow R, Kern F. Liquid-phase coating of carbon fibers with pre-ceramic polymer precursors: process and applications. Adv Eng Mater 2002;4:883–6.
[648] Schütz A, Günthner M, Motz G, Greißl O, Glatzel U. Characterisation of novel precursor-derived ceramic coatings with glass filler particles on steel substrates. Surf Coat Technol 2012;207:319–27.
[649] Günthner M, Kraus T, Dierdorf A, Decker D, Krenkel W, Motz G. Advanced coatings on the basis of Si(C)N precursors for protection of steel against oxidation. J Eur Ceram Soc 2009;29:2061–8.
[650] Liu J, Zhang L, Hu F, Yang J, Cheng L, Wang Y. Polymer-derived yttrium silicate coatings on 2D C/SiC composites. J Eur Ceram Soc 2013;33:433–9.
[651] Günthner M, Kraus T, Krenkel W, Motz G, Dierdorf A, Decker D. Particle-filled PHPS silazane-based coatings on steel. Int J Appl Ceram Tec 2009;6:373–80.
[652] Shah SR, Raj R. Multilayer design and evaluation of a high temperature environmental barrier coating for Si-based ceramics. J Am Ceram Soc 2007;90:516–22.
[653] Zhao G, Hu P, Zhou S, Chen G, An Y, Cheng Y, et al. Ordered silica nanoparticles grown on a three-dimensional carbon fiber architecture substrate with siliconborocarbonitride ceramic as a thermal barrier coating. ACS Appl Mater Inter 2016;8:4216–25.
[654] Stern E, Heyder M, Scheffler F. Micropatterned ceramic surfaces by coating with filled preceramic polymers. J Am Ceram Soc 2009;92:2438–42.
[655] Wach RA, Sugimoto M, Yoshikawa M. Formation of silicone carbide membrane by radiation curing of polycarbosilane and polyvinylsilane and its gas separation up to 250 °C. J Am Ceram Soc 2007;90:275–8.
[656] Miyajima K, Eda T, Ohta H, Ando Y, Nagaya S, Ohba T, et al. Development of Si-N based hydrogen separation membrane. Ceram Trans 2010;213:87–94.
[657] Pivin J, Sendova-Vassileva M, Colombo P, Martucci A. Photoluminescence of composite ceramics derived from polysiloxanes and polycarbosilanes by ion

irradiation. Mater Sci Eng, B 2000;69:574–7.
[658] Pivin J, Colombo P, Martucci A, Soraru G, Pippel E, Sendova-Vassileva M. Ion beam induced conversion of Si-based polymers and gels layers into ceramics coatings. J Sol-Gel Sci Technol 2003;26:251–5.
[659] Wang Y, Ding J, Feng W, An L. Effect of pyrolysis temperature on the piezoresistivity of polymer-derived ceramics. J Am Ceram Soc 2011;94:359–62.
[660] Li N, Cao Y, Zhao R, Xu Y, An L. Polymer-derived SiAlOC ceramic pressure sensor with potential for high-temperature application. Sensor Actuat A-Phys 2017;263:174–8.
[661] Nagaiah N, Kapat J, An L, Chow L. Novel polymer derived ceramic-high temperature heat flux sensor for gas turbine environment. J Phys Conf Ser. IOP Publishing; 2006. p. 458.
[662] Seo D, Jung S, Lombardo SJ, Feng Z, Chen J, Zhang Y. Fabrication and electrical properties of polymer-derived ceramic (PDC) thin films for high-temperature heat flux sensors. Sensor Actuat A-Phys 2011;165:250–5.
[663] Zhao R, Shao G, Cao Y, An L, Xu C. Temperature sensor made of polymer-derived ceramics for high-temperature applications. Sensor Actuat A-Phys 2014;219:58–64.
[664] Ren X, Ebadi S, Chen Y, An L, Gong X. Characterization of SiCN ceramic material dielectric properties at high temperatures for harsh environment sensing applications. IEEE Trans Micro Theory Tech 2013;61:960–71.
[665] Gong X, An L, Xu C. Wireless passive sensor development for harsh environment applications. 2012 IEEE International Workshop on Antenna Technology (iWAT). IEEE; 2012. p. 140–3.
[666] Karakuscu A, Ponzoni A, Aravind PR, Sberveglieri G, Soraru GD. Gas sensing behavior of mesoporous SiOC glasses. J Am Ceram Soc 2013;96:2366–9.
[667] Karakuscu A, Hu LH, Ponzoni A, Baratto C, Ceccato R, Sberveglieri G, et al. Si OCN functionalized carbon nanotube gas sensors for elevated temperature applications. J Am Ceram Soc 2015;98:1142–9.
[668] Feng Y, Yu Z, Schuch J, Tao S, Wiehl L, Fasel C, et al. Ternary Nowotny phase $Mo_{3+2x}Si_3C_{0.6}$ dispersed in a porous SiC/C matrix: a novel catalyst for hydrogen evolution reaction. J Am Ceram Soc 2019;103(1):508–19. https://doi.org/10.1111/jace.16731.
[669] Schitco C, Bazarjani MS, Riedel R, Gurlo A. Ultramicroporous silicon nitride ceramics for CO_2 capture. J Mater Res 2015;30:2958–66.
[670] Jones RH, Giancarli L, Hasegawa A, Katoh Y, Kohyama A, Riccardi B, et al. Promise and challenges of SiC_f/SiC composites for fusion energy applications. J Nucl Mater 2002;307:1057–72.
[671] Colombo P, Riccardi B, Donato A, Scarinci G. Joining of SiC/SiC_f ceramic matrix composites for fusion reactor blanket applications. J Nucl Mater 2000;278:127–35.
[672] Xing W, Wilson A, Zank G, Dahn J. Pyrolysed pitch-polysilane blends for use as anode materials in lithium ion batteries. Solid State Ionics 1997;93:239–44.
[673] Wilson A, Xing W, Zank G, Yates B, Dahn J. Pyrolysed pitch-polysilane blends for use as anode materials in lithium ion batteries II: the effect of oxygen. Solid State Ionics 1997;100:259–66.
[674] Kaspar J, Graczyk-Zajac M, Riedel R. Determination of the chemical diffusion coefficient of Li-ions in carbon-rich silicon oxycarbide anodes by electro-analytical methods. Electrochim Acta 2014;115:665–70.
[675] Li Z, Wang Y. Preparation of polymer-derived graphene-like carbon-silicon carbide nanocomposites as electromagnetic interference shielding material for high temperature applications. J Alloys Compd 2017;709:313–21.
[676] Shen G, Xu Z, Li Y. Absorbing properties and structural design of microwave absorbers based on W-type La-doped ferrite and carbon fiber composites. J Magn Magn Mater 2006;301:325–30.
[677] Meshram M, Agrawal NK, Sinha B, Misra P. Characterization of M-type barium hexagonal ferrite-based wide band microwave absorber. J Magn Magn Mater 2004;271:207–14.
[678] Qin F, Brosseau C. A review and analysis of microwave absorption in polymer composites filled with carbonaceous particles. J Appl Phys 2012;111:061301.
[679] Micheli D, Apollo C, Gradoni G, Marchetti M, Morles RB, Pastore R. Electromagnetic characterization of composite materials and microwave absorbing modeling. INTECH Open Access Publisher; 2011.
[680] Kang Y, Chu Z, Zhang D, Li G, Jiang Z, Cheng H, et al. Incorporate boron and nitrogen into graphene to make BCN hybrid nanosheets with enhanced microwave absorbing properties. Carbon 2013;61:200–8.
[681] Riedel R, Ionescu E, Bansal N, Boccaccini A. Polymer processing of ceramics in ceramics and composites processing methods. Bansal: NP; 2012. p. 235–70.
[682] Kong L, Yin X, Ye F, Li Q, Zhang L, Cheng L. Electromagnetic wave absorption properties of ZnO-based materials modified with $ZnAl_2O_4$ nanograins. J Phys Chem C 2013;117:2135–46.
[683] Liu X, Yin X, Kong L, Li Q, Liu Y, Duan W, et al. Fabrication and electromagnetic interference shielding effectiveness of carbon nanotube reinforced carbon fiber/pyrolytic carbon composites. Carbon 2014;68:501–10.
[684] Arjmand M, Mahmoodi M, Gelves GA, Park S, Sundararaj U. Electrical and electromagnetic interference shielding properties of flow-induced oriented carbon nanotubes in polycarbonate. Carbon 2011;49:3430–40.
[685] Wen Q, Yu Z, Liu X, Bruns S, Yin X, Eriksson M, et al. Mechanical properties and electromagnetic shielding performance of single-source-precursor synthesized dense monolithic SiC/HfC_xN_{1-x}/C ceramic nanocomposites. J Mater Chem C 2019;7:10683–93.
[686] Luo X, Chung D. Electromagnetic interference shielding using continuous carbon-fiber carbon-matrix and polymer-matrix composites. Compos Part B Eng. 1999;30:227–31.
[687] Yan DX, Pang H, Li B, Vajtai R, Xu L, Ren PG, et al. Structured reduced graphene oxide/polymer composites for ultra-efficient electromagnetic interference shielding. Adv Funct Mater 2015;25:559–66.
[688] Mu Y, Zhou W, Wang C, Luo F, Zhu D, Ding D. Mechanical and electromagnetic shielding properties of SiC_f/SiC composites fabricated by combined CVI and PIP process. Ceram Int 2014;40:10037–41.
[689] Duan W, Fan Z, Wang H, Zhang J, Qiao T, Yin X. Electromagnetic interference shielding and mechanical properties of Si_3N_4-SiOC composites fabricated by 3D-printing combined with polymer infiltration and pyrolysis. J Mater Res. 2017;32:3394–401.
[690] Park J-K. Principles and applications of lithium secondary batteries. John Wiley & Sons; 2012.
[691] Riedel R. Nanoscaled inorganic materials by molecular design. Chem Soc Rev 2012;41:5029–31.
[692] Greaves GN, Greer A, Lakes RS, Rouxel T. Poisson's ratio and modern materials. Nat Mater 2011;10:823.
[693] Rouxel T, Sanglebœuf JC, Guin JP, Keryvin V, Soraru GD. Surface damage resistance of gel-derived oxycarbide glasses: hardness, toughness, and scratchability. J Am Ceram Soc 2001;84:2220–4.
[694] Blum YD, Hui DK, MacQueen DB. Method of imparting corrosion resistance to a substrate surface, and coated substrates prepared thereby. Google Patents; 2012.
[695] Wang Y, Tian H, Quan D, Guo L, Ouyang J, Zhou Y, et al. Preparation, characterization and infrared emissivity properties of polymer derived coating formed on 304 steel. Surf Coat Technol 2012;206:3772–6.
[696] Kappa M, Kebianyor A, Scheffler M. A two-component preceramic polymer system for structured coatings on metals. Thin Solid Films 2010;519:301–5.
[697] Kaspar J. Carbon-rich silicon oxycarbide (SiOC) and silicon oxycarbide/element (SiOC/X, X= Si, Sn) nano-composites as new anode materials for Li-ion battery application. Technische Universität; 2014.
[698] Wilson A, Reimers J, Fuller E, Dahn J. Lithium insertion in pyrolyzed siloxane polymers. Solid State Ionics 1994;74:249–54.
[699] Fukui H, Ohsuka H, Hino T, Kanamura K. Silicon oxycarbides in hard-carbon microstructures and their electrochemical lithium storage. J Electrochem Soc 2013;160:A1276–81.
[700] Luo C, Tang Y, Jiao T, Kong J. High-temperature stable and metal-free electromagnetic wave-absorbing SiBCN ceramics derived from carbon-rich hyper-branched polyborosilazanes. ACS Appl Mater Inter 2018;10:28051–61.

Dr. Qingbo Wen is a postdoc researcher in Prof. Riedel's group at the Technische Universität Darmstadt in Germany, where he received his PhD degree in Materials Science in 2017. He got his master's degree (2012) and bachelor's degree (2009) in Environmental Engineering at Hunan University in China. One of his research interests is focused on polymer-derived ceramics (PDCs), particularly on the development of advanced ceramic nanocomposites with tailor-made chemical/phase compositions and microstructures for structural and functional applications in harsh environment (*e.g.*, ultrahigh-temperature ceramics/composites for thermal protection systems, high-temperature electromagnetic wave absorbing/shielding materials as well as electrode materials for high-temperature fuel cells). Another research interest is devoted to ultrahigh-pressure and high-temperature synthesis of novel transition metal nitrides and their solid solutions. Up to now, Dr. Wen has published more than 30 papers in peer-reviewed journals and filed four patents as first/corresponding author or co-author.

Prof. Zhaoju Yu received her PhD degree in Polymer Chemistry and Physics in 2004 at the Wuhan University, China. She is presently Full Professor and Deputy Director of Key Laboratory of High Performance Ceramic Fibers at the College of Materials, Xiamen University, China. Prof. Yu was a Humboldt Research Fellow (Awarded on 15.12.2016) and guest professor in the frame of an international scientist exchange program with the research group "Disperse Feststoffe" at the Materials and Geosciences Department of the Technische Universität Darmstadt. Since 2019, she is Associate Editor of the journal of *Ceramics International*. Her research fields cover ceramic nanocomposites, ceramic fibers and silicon-based polymer materials. In particular, her research work is focused on i) advanced Si-based ceramic nanocomposites containing nanocarbon phases by molecular approach; and ii) correlation of the molecular structure of pre-ceramic polymers with the microstructure and advance functional properties (such as electrical, dielectric, catalytic, electromagnetic properties) of the ceramic materials obtained therefrom. She has currently published more than 60 scientific papers in peer-reviewed journals, gave more than 30 Invited Conference Presentations and authored 11 granted patents.

Prof. Riedel got a PhD degree in Inorganic Chemistry in 1986 at the University of Stuttgart. After a Postdoc period at the Max-Planck Institute für Metallforschung in Stuttgart, he became Full Professor at the Institute of Materials Science at the Technische Universität Darmstadt in 1993. He is an elected member of the World Academy of Ceramics, Fellow of the American Ceramic Society, the European Ceramic Society as well as Fellow of the School of Engineering at The University of Tokyo in Japan. Prof. Riedel was awarded with the Gold Medal for Merits in Natural Sciences and with an honorary doctorate of the Slovak Academy of Science as well as with the Gustav Tammann Prize of the German Society of Materials Science (DGM). In 2009, he received an honorary Professorship at the Tianjin University in Tianjin, China. He was Guest Professor at the Jiangsu University in Zhenjiang and at the Xiamen University in China. Recently, Prof. Riedel received the Innovation Talents Award of Shaanxi Province, China at the Northwestern Polytechnical University in Xían. He is Guest Professor at the University of Tokyo in the group of Prof. Ikuhara, Japan and was awarded with the International Ceramics Prize 2020 for "Basic Science" of the World Academy of Ceramics. HeHe is Editor in Chief of the Journal of The American Ceramic Society and of Ceramics International. His current research interest is focused on two research areas, namely i) molecular synthesis of advanced structural and functional ceramics for ultra-high temperature and energy-related applications as well as ii) ultrahigh pressure materials synthesis.